



Title	Velocity profiling based rheometry toward model-free characterization of non-Newtonian fluids
Author(s)	白鳥, 貴久
Citation	北海道大学. 博士(工学) 甲第11884号
Issue Date	2015-03-25
DOI	10.14943/doctoral.k11884
Doc URL	<a href="http://hdl.handle.net/2115/60949">http://hdl.handle.net/2115/60949</a>
Type	theses (doctoral)
File Information	Takahisa_Shiratori.pdf



[Instructions for use](#)

Velocity profiling based rheometry toward  
model-free characterization of  
non-Newtonian fluids

Takahisa SHIRATORI

Laboratory for Flow Control,  
Graduate School of Engineering,  
Hokkaido University

Supervised by  
Prof. Dr. Y. Murai

February 18th, 2015

Chapter 1	Introduction	1
1.1	Background	1
1.1.1	Focused length scale in quantification of property	1
1.1.2	Comparison of various kinds of rheometer	3
1.1.3	Fluid characterization enabled by velocity profiling	5
1.1.4	Flow surface as a beginning of data driven fluid engineering	7
1.2	Objective and outline	9
Chapter 2	Quantitative visualization of viscoelastic flows	14
2.1	Introduction	14
2.2	Experimental setup	15
2.3	Spatio-temporal distributions obtained by UVP	20
2.4	Visualization of fluid motion	23
2.4.1	Vector expressions of velocity for intuitive understanding	23
2.4.2	Visualization of fluid deformation with grid expression	26
2.4.3	Simultaneous visualization of fluid motion and shear rate	29
2.5	Conclusion	32
Chapter 3	Quantification of shear-rate-dependent viscosity from steady shear flow	36
3.1	Introduction	36
3.2	Experimental setup	39
3.2.1	Experimental apparatus	39
3.2.2	Error propagation and measurement limitation	42
3.3	Flow curve derivation with finite differential method and power law	47
3.4	Flow curve derivation without rheological model	57
3.5	Conclusion	65
Chapter 4	Characterization of viscoelasticity and flow simulation	69
4.1	Introduction	69
4.2	Experimental setup	71
4.3	Spatio-temporal velocity distributions	76
4.4	Quantification of viscoelasticity	78
4.4.1	Procedure to derive shear stress distribution	78
4.4.2	The obtained shear stress and quantified viscoelasticity	78
4.4.3	Error propagation and measurement limitation	80
4.5	Application to numerical simulations	86

	4.5.1	Procedure of the numerical simulation	86
	4.5.2	Interpolation of the discretized relation to determine shear stress	88
	4.5.3	Spatio-temporal velocity distribution obtained by the simulation	91
	4.6	Conclusion	92
Chapter 5		Effective viscosity measurement of highly concentrated suspension by expanding interfacial rheometry	96
	5.1	Introduction	96
	5.2	Experimental setup	97
	5.3	Effective viscosity of suspensions characterized with flow curve	100
	5.4	Conclusion	103
Chapter 6		Conclusions and future perspectives	106
	6.1	Conclusions	106
	6.2	Future perspectives	108
	6.3	Summary of measurement limitations	110

## 1.1 Background

### 1.1.1 Focused length scale in quantification of property

In the present industrialized society, handling of materials which have complex fluid properties, such as non-Newtonian viscosity and viscoelasticity, is required. In the food industry, for example, flow property of foods affects processing efficiency and food quality [1]. Also in other industries and research fields, such as polymer industry, energy industry and life science, materials with complex property are utilized. The flow property of these materials has to be quantified through concepts like viscoelasticity and non-Newtonian viscosity to handle these materials. In the scientific discipline called rheology, concepts to understand complex fluid properties have been invented, and quantities to describe properties have been defined. Methodology to measure the quantities to understand properties is called rheometry.

Because rheology has developed in various industries and academic research fields, it is bifurcating into particularized fields such as food rheology, polymer rheology and bio-rheology. In each fields of rheology, models to describe fluid properties, called rheological model, have been provided. The models are useful to represent complex fluid properties of materials, and have been employed to predict non-Newtonian fluid flows. In the process engineering, for example, flow in processing plants is simulated to design highly efficient plants. One of the difficulties in simulating non-Newtonian fluid flows is a choice of rheological model. Because most of rheological models are specialized to describe property of materials in a certain group, mischoice of the model causes a considerable gap between simulated and real flows.

Rheology and rheological models have been segmentalized, because rheological models are based on microstructure of materials. Figure 1.1 shows schematic of rheological modeling in different length scales in the case of polymer rheology. In the smallest length scale, all atoms in the polymer chain are described. Thus all of interatomic interactions are taken into account. One of the problems of this all-atomistic simulation is that much computational resources are required. Because motions of many atoms have to be calculated in long time scale to explain macroscopic flow behaviors, it is practically impossible to predict macroscopic flows based on the all-atomistic simulation. Then molecular chains are described coarsely by introducing coarse-graining [2-4]. In bead-spring model, for example, two or three monomer units are described as one bead [5]. Through the coarse-graining, motion of polymer chains is predicted with less computational resources. The largest scale in Fig. 1.1 is continuous

model which describes a relation between macroscopic deformation and generated stress. Models in larger length scale call values of model constants from models in smaller length scale. In this way, macroscopic behavior of polymeric materials is simulated based on molecular dynamics.

This study aims to provide a method to evaluate viscoelasticity of materials as continuum regardless of microscopic structure. This enables to characterize materials belonging in any groups such as polymers, foods or biomaterials. Instead of the modeling in microscopic scales, the relation between deformation and stress in macroscopic scale is described with experimental data. So far, only rheometers are used as a device to obtain the relation experimentally in macro scale, thus the experimental data can explain flows only in limited cases such as steady shear flows governed by shear-rate-dependent viscosity. Velocimetries developed in recent years enable to quantify properties of fluids from velocity distribution of flows as described in the next section. It is possible to characterize fluids not based on rheological models but on experimental data. This methodology is called “model-free characterization” in this study.

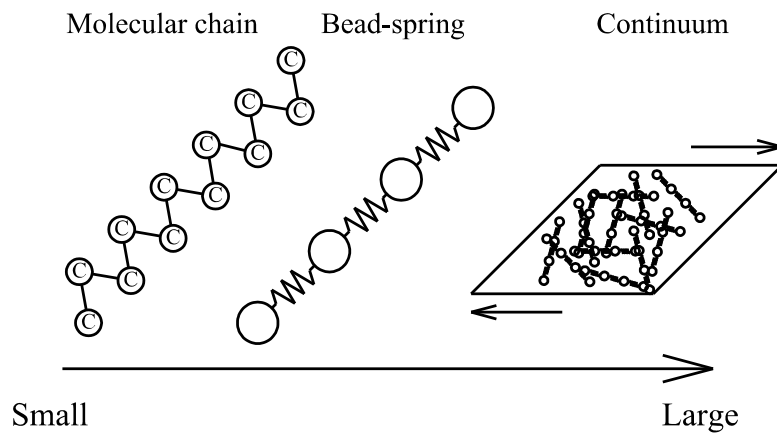


**Figure 1.1** Modeling of a polymeric fluid in different length scales

### 1.1.2 Comparison of various kinds of rheometer

To quantify properties of non-Newtonian fluids in macroscopic length scale, devices called rheometer have been employed. The property of a non-Newtonian fluid is grasped by measuring various quantities such as shear-rate-dependent viscosity, storage and loss moduli, and elongational viscosity. Various kinds of rheometer have been developed to measure these quantities. These rheometers have advantages and disadvantages as summarized in Table 1.1.

Conventional shear rheometers, such as cone-plate, parallel-plates and concentric-cylinders rheometers, measure properties of fluids by applying shear deformation to the test fluid. Fluid layer between these objects is thin, and the flow is assumed to be a Couette flow where shear rate is constant over the fluid layer. Because of this assumption, velocity slip on the wall [6], shear banding [7] and some other phenomenon cause errors on the obtained fluid properties.

To describe flows of non-Newtonian fluids, not only shear but also elongational properties, such as elongational viscosity, have to be taken into account. The elongational property is not a matter in Newtonian flows because the ratio of elongational viscosity to shear viscosity, called Trouton's ratio, theoretically equals three. For non-Newtonian fluids, however, Trouton's ratio not always equals three and thus elongational rheometers [8-12] have been developed. It is known that elongational properties affect various phenomena such as drag force on a sphere [13] and transition to turbulence [14-16].

Although motion of a sphere and induced flow around it have been examined to measure viscosity of Newtonian fluids, the flow around a sphere is object of investigation also in non-Newtonian cases. Because it is clarified that a sphere falling through non-Newtonian fluids induce elongational flow, and elongational properties affect the flow [17,18], there is a possibility that elongational properties are derived from the falling sphere measurement by measuring velocity distribution around the sphere. From this point of view, our group investigated viscoelastic flows around a sphere [19,20]. Flow around a sphere is utilized as a rheometer also for another objective, namely reduction of the volume of test fluids. Spinning sphere rheometer [21] enabled to measure viscosity with 0.1 ml of test fluid. Reduction of the test volume is important in biorheology where it is difficult to prepare much amount of test fluids.

As described above, rheometers which have been developed so far have advantages and disadvantages. Recently, some researches succeed in developing rheometers with new advantages by introducing velocity profiling techniques for flow measurement. For example, it is enabled to measure shear-rate-dependent viscosity even

if slip or shear band occurs by taking distributions of velocity and shear rate into account. In the next section, advantages to introduce velocity profiling to rheometry are described in detail.

**Table 1.1** Characteristics of various kinds of rheometer

	Shear-rate-dependent viscosity	Viscoelasticity	Elongational properties	Large ingredients	Inhomogeneity	In-line	Required fluid volume
Conventional shear rheometers	☆	☆☆					1 ml
Elongational rheometers			☆☆				1 ml~ 1000 ml
Falling sphere	☆	☆	☆	☆			100 ml~ 1000 ml
Spinning sphere	☆	☆					0.1 ml
Pipe with velocity profiling	☆			☆	☆	☆	10 l
Concentric cylinders with velocity profiling	☆	☆☆		☆	☆		100 ml~ 1000 ml

### 1.1.3 Fluid characterization enabled by velocity profiling

Velocity profiling techniques, such as ultrasonic velocity profiler (UVP) [22] and particle imaging velocimetry (PIV) [23], were developed and sophisticated in recent years, and applied for evaluation of property of fluids. One of the most usual ways to evaluate property is to measure viscosity depending on shear rate or any other quantities. Because viscosity is defined as a ratio of stress to shear rate, simultaneous measurement of stress and velocity gives viscosity, even if it varies spatio-temporally. For example, UVP-PD [24-31] enabled to obtain shear-rate-dependent viscosity by measuring velocity profiles and pressure drop (PD) in steady pipe flows. The measured velocity profile and pressure drop give shear rate and shear stress profiles, respectively. In rheology, diagram describing the relationship between shear rate and shear stress, termed “flow curve”, is used to quantify viscous property. Thus the measured data in UVP-PD are summarized as flow curve, and applied to control qualities in processing plant. Velocimetries other than UVP, for example PIV [6,32-34], LDA (laser Doppler anemometer) [27] and NMR (nuclear magnetic resonance) [35, 36] are also combined with PD measurement. PD measurement is also replaced by other measurements, such as stress-optical rule [37-39] or torque measurement [40], to realize rheometry.

In the previous researches introduced above, fluid properties are determined by analyzing flows to the opposite direction of physical phenomenon as Fig 1.2 shows. Fluid phenomena are understood as follows: Fluids have their own property independent on how the fluid flows. When the fluid is forced to deform, it flows to satisfy momentum conservation and mass conservation laws. Velocity and stress distributions are given as a solution of the conservation laws. In the characterizations based on velocimetry, on the other hand, experimental data is analyzed toward the opposite direction of the physical phenomena: velocity and stress information are given at first as the experimental results, and rheological properties are determined by solving momentum conservation law. Velocity information should be given as spatio-temporal distribution to perform this analysis. Thus profiling techniques, UVP and PIV, play a significant role in this study.

Although there are a number of previous researches about fluid characterization by introducing velocity profiling, little research has been done on quantification of viscoelasticity, i.e. most of the researches focus on shear-rate-dependent viscosity with a flow curve. Because the flow curve is insufficient to represent viscoelasticity, “flow surface”, the relation between shear rate, strain and shear stress, is suggested as a diagram to represent viscoelasticity. The term “flow surface” means that strain is added to flow curve as a quantity to explain shear stress. Difficulty in quantifying

viscoelasticity is taking into account unsteady motions of the fluid. In the evaluation of shear rate dependent viscosity, it is enough to analyze steady state, because viscosity governs the flow when strain rate is applied for longer time than the relaxation time of the fluid. On the other hand, flows governed by viscoelasticity, for example an oscillatory flow, are usually unsteady. Thus momentum conservation law is solved while taking time-derivative term into account. The obtained stress distribution as a solution is displayed in the form of flow surface. The process of solving momentum conservation law in unsteady form is exactly an analysis to the opposite direction of physical phenomenon.

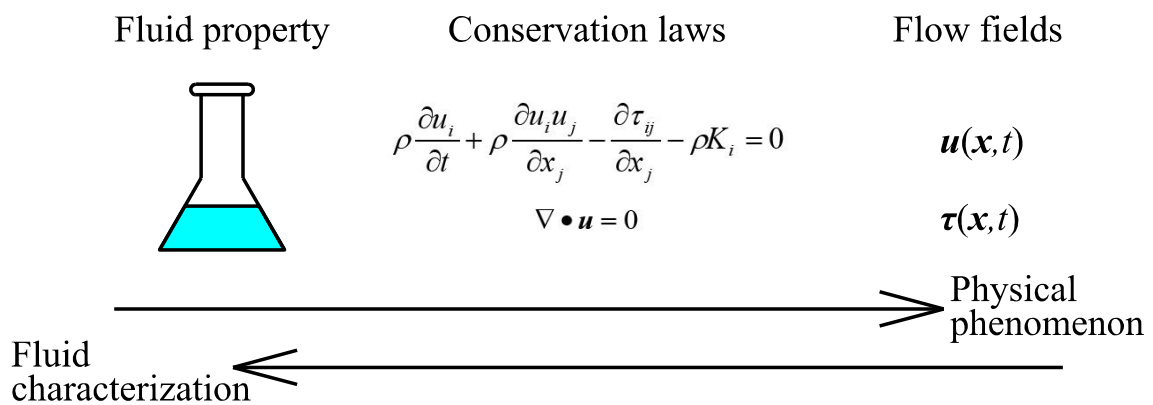


**Figure 1.2** Fluid characterization as an analysis to the opposite direction of physical phenomenon

#### 1.1.4 Flow surface as a beginning of data driven fluid engineering

As the flow surface contains information of a relation between deformation and stress generation, it is applicable in numerical simulations. In simulations of Newtonian fluid flows, equation of continuity, momentum conservation law and Newton's law of viscosity are solved simultaneously. For non-Newtonian fluid flows, as its name suggests, Newton's law of viscosity is not applicable. Alternative equations to Newton's law of viscosity have been proposed and the equations should describe the relation between deformation and stress generation, and termed constitutive equation. Forming the flow curve as the constitutive equation make simulations of non-Newtonian fluid flows possible.

Because flow surfaces are formed from experimental data, the utilization of flow surfaces in numerical simulation corresponds to replacing constitutive equations by experimental data. Recently, performance of information-processing equipment is rapidly increasing, and it becomes easier to store and utilize data. Thus complicated theories are replaced by stored big data in many fields. For example, Google Translate, one of the most popular website providing automated translation, improved their translation algorithm with big data [41]. In their early days, Google Translate tried translating sentences based on grammatical theories of each language. But now sentences are translated in the different way. They statistically analyzed correspondence of words and grammatical structure in many sentences written in different languages and having mutual meaning, such as global treaties, as big data. In this way, they succeeded in improving quality of the automated translation. This case represents that theory can be replaced by results of statistical analyses for big data. An adjective phrase "data driven" is used to mean that complicated theories are replaced by big data.

Characterization of fluids with flow surface and application of flow surface to numerical simulations will be the first step of "data driven fluid engineering". Figure 1.3 shows analogy between the automated translation and the flow simulation with the flow surface. In data driven systems, beneficial rules are obtained from big data through statistical analysis. In the case of automated translation, sentences written in various languages correspond to the big data. Through the statistical analysis, correspondence of words and grammatical structure are obtained as beneficial rules. These rules are applied to automated translation which translates input sentence according to the obtained rule. In data driven fluid engineering, quantities measured in the experiment, such as velocity and stress distributions, play a role of big data. It has been difficult to acquire "big" data about non-Newtonian fluids, because measurements with rheometer take a long time. The development of velocity profiling techniques is improving the

situation. Statistical analysis clarifies which factor is dominant to determine the stress as rules. Flow surface is regarded as a way to display the result of the analysis with insight with the prospect that stress is determined by shear rate and strain. Application of the obtained rules is numerical simulation of non-Newtonian fluid flows. Data driven flow simulation is already performed for transport phenomena over a wide region, for example modeling of flood [42]. If the day comes when data driven fluid engineering is established, flows of new materials are simulated without constructing rheological model from dynamics in microscopic scale to continuum dynamics.

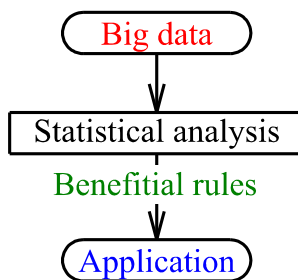
Google Translate

Data driven fluid engineering

Sentences written  
in various languages

Experimental information

Words correspondence  
& grammatical structure



Factors to determine stress  
(Displayed as flow surface)

Automated translation

Flow simulation

**Figure 1.3** How experimental information and flow surface contribute to data driven fluid engineering

## 1.2 Objective and outline

This research aim to quantify rheological properties, namely shear-rate-dependent viscosity and viscoelasticity, in a way applicable to materials regardless of microstructure. Velocity profiling is employed in order to enable the quantification by analyzing flows to the opposite direction of physical phenomena. The present way of quantifying rheological property is applicable to materials with any kind of microstructure because it is focused on the length scale of continuum.

In Chapter 2, flow of viscoelastic fluids is quantitatively visualized by using ultrasonic velocity profiling (UVP). Spin down flow in a rotational cylinder is visualized to observe oscillatory flow induced by viscoelasticity. By visualizing shear rate and deformation, which relate to viscous and elastic stress, respectively, it is confirmed that the flow is affected by viscoelasticity. Applicability of UVP to opaque fluids is also confirmed by visualizing flow in an opaque yogurt. Shear-rate-dependent viscosity is quantified in Chapter 3. Concentric cylinders with a wide gap is chosen as configuration because shear stress profile is easily obtained under the steady state. From the shear stress profile and measured velocity profile, the relationship between shear rate and shear stress, termed flow curve, is obtained as a lot of local relations. The applicability to opaque fluids is acquired by introducing UVP. In Chapter 4, viscoelasticity is quantified as the relation among shear rate, strain and shear stress. The relation is named “flow surface” as extension of the flow curve. Unsteady flow after the spin up of the inner cylinder is measured. Because momentum conservation law have to be solved spatio-temporally, particle imaging velocimetry (PIV) is employed to acquire velocity distribution with less measurement noise. As application of the flow curve, velocity distribution is reconstructed by solving simultaneous equation of momentum conservation and the flow surface. In Chapter 5, effective viscosity of highly concentrated particle suspension is evaluated. By extending a function of interfacial rheometer, effective viscosity and particle motion in the suspension are monitored simultaneously. Effective viscosity depending on shear rate is obtained as a rheological property in length scale of continuum.

## References

- [1] P. Fischer, E. J. Windhab, Rheology of food materials, *Current Opinion in Colloid & Interface Science* 16 (2011) 36-40
- [2] C. Tzoumanekas, D.N. Theodorou, From atomistic simulations to slip-link models of entangled polymer melts: Hierarchical strategies for the prediction of rheological properties, *Current Opinion in Solid State and Materials Science* 10 (2006) 61-72
- [3] J.T. Padding, W.J. Briels, Systematic coarse-graining of the dynamics of entangled polymer melts: the road from chemistry to rheology, *J. Phys. Condens. Matter* 23 (2011) 233101
- [4] Y. Li, B.C. Abberton, M. Kröger, W.K. Liu, Challenges in Multiscale Modeling of Polymer Dynamics, *Polymers* 5 (2013) 751-832
- [5] M. Doi (ed), *Polymeric materials simulation*, The Chemical Daily, Tokyo, 2014 (in Japanese)
- [6] F. Rodríguez-González, J. Pérez-González, L. Vargas, B.M. Marín-Santibáñez, Rheo-PIV analysis of the slip flow of a metallocene linear low-density polyethylene melt, *Rheol Acta* 49 (2010) 145-154
- [7] C. J. Dimitriou, L. Casanellas, T. J. Ober, G. H. McKinley, Rheo-PIV of a shear-banding wormlike micellar solution under amplitude oscillatory shear, *Rheol Acta* 51 (2012) 395-411
- [8] P. Schümmer, K. H. Tebel, Design and operation of the free jet elongational rheometer, *Rheol Acta*, 21 (1982) 514-516
- [9] P. Schümmer, K. H. Tebel, A new elongational rheometer for polymer solutions, *J. Non-Newtonian Fluid Mech.* 12 (1983) 331-347
- [10] J. Meissner, J. Hostettler, A new elongational rheometer for polymer melts and other highly viscoelastic liquids, *Rheol Acta* 33 (1994) 1-21
- [11] M. Stelter, G. Brenn, Elongational rheometry for the characterization of viscoelastic liquids, *Chem. Eng. Technol.* 25 (2002) 30-35
- [12] G. H. McKinley, T. Sridhar, Filament-stretching rheometry of complex fluids, *Annu. Rev. Fluid Mech.* 34 (2002) 375-415
- [13] E. Mitsoulis, Effect of rheological properties on the drag coefficient for creeping motion around a sphere falling in a tightly-fitting tube, *J. Non-Newtonian Fluid Mech.* 74 (1998) 263-283
- [14] P. J. Oliveira, F. T. Pinho, A qualitative assessment of the role of a viscosity depending on the third invariant of the rate-of-deformation tensor upon turbulent non-Newtonian flow, *J. Non-Newtonian Fluid Mech.* 78 (1998) 1-25
- [15] A. Groisman, V. Steinberg, Elastic turbulence in a polymer solution flow, *Nature*

405 (2000) 53-55

- [16] S. Tamano, M. Itoh, S. Hotta, K. Yokota, Y. Morinishi, Effect of rheological properties on drag reduction in turbulent boundary layer flow, *Phys. Fluids* 21 (2009) 055101
- [17] M. T. Arigo, G. H. McKinley, An experimental investigation of negative wakes behind spheres settling in a shear-thinning viscoelastic fluid, *Rheol. Acta* 37 (1998) 307-327
- [18] S. Chen, J. P. Rothstein, Flow of a wormlike micelle solution past a falling sphere, *J. Non-Newtonian Fluid Mech.* 116 (2004) 205-234
- [19] T. Shiratori, Y. Tasaka, Y. Murai, K. Oyama, I. Kumagai, Y. Takeda, Flow of a viscoelastic fluid around a falling sphere, *ASME-KSME-KSME 2011 Joint Fluids Eng. Conf.* (2011) 2657-2662
- [20] T. Shiratori, Y. Oishi, Y. Tasaka, Y. Murai, Characterization of viscoelasticity from complex flows with shear and extension, *The 12<sup>th</sup> Int. Symp. Fluid Control. Meas. Vis.* (2013) OS8-04-2
- [21] K. Sakai, T. Hirano, M. Hosoda, Electromagnetically spinning sphere viscometer, *App. Phys. Exp.* 3 (2010) 016602
- [22] Y. Takeda (ed), *Ultrasonic Doppler Velocity Profiler for Fluid Flow*, Springer, Tokyo, 2012
- [23] R. J. Adrian, Twenty years of particle image velocimetry, *Experiments in Fluids* 39 (2005) 159-169
- [24] B. Ouriev, Investigation of the Wall Slip Effect in Highly Concentrated Disperse Systems by Means of Non-Invasive UVP-PD Method in the Pressure Driven Shear Flow, *Colloid J.* 64 (2002) 740-745
- [25] B. Ouriev, E.J. Windhab, Rheological study of concentrated suspensions in pressure-driven shear flow using a novel in-line ultrasound Doppler method, *Experiments in Fluids* 32 (2002) 204-211
- [26] B. Ouriev, E. Windhab, P. Braun, B. Birkhofer, Industrial application of ultrasound based in-line rheometry: From stationary to pulsating pipe flow of chocolate suspension in precrystallization process, *Rev. Scientific Instruments* 75 (2004) 3164-3168
- [27] J.A. Wiklund, M. Standing, A.J. Pettersson, A. Rasmuson, A Comparative Study of UVP and LDA Techniques for Pulp Suspensions in Pipe Flow, *AIChE J.* 52 (2006) 484-495
- [28] J. Wiklund, I. Shahram, M. Standing, Methodology for in-line rheology by ultrasound Doppler velocity profiling and pressure difference techniques, *Chemical Engineering Sci.* 62 (2007) 4277-4293

- [29] B.H. Birkhofer, S.A.K. Jeelani, E.J. Windhab, B. Ouriev, K.-J. Lisner, P. Braun, Y. Zeng, Monitoring of fat crystallization process using UVP–PD technique, *Flow Meas. Instrumentation* 19 (2008) 163-169
- [30] J. Wiklund, M. Standing, Application of in-line ultrasound Doppler-based UVP–PD rheometry method to concentrated model and industrial suspensions, *Flow Measurement Instrumentation* 19 (2008) 171-179
- [31] J. Wiklund, M. Stading, C. Trägårdh, Monitoring liquid displacement of model and industrial fluids in pipes by in-line ultrasonic rheometry, *J. Food Engineering* 99 (2010) 330-337
- [32] J. Pérez-González, J.J. López-Durán, B.M. Marín-Santibáñez, F. Rodríguez-González, Rheo-PIV of a yield-stress fluid in a capillary with slip at the wall, *Rheol Acta* 51 (2012) 937-946
- [33] J.J. López-Durán, J. Pérez-González, B.M. Marín-Santibáñez, F. Rodríguez-González, A New method to determine the yield stress of a fluid from velocity profiles in a capillary, *Revista Mexicana de Ingeniería Química* 12 (2013) 121-128
- [34] H.C.H. Bandalusena, W.B. Zimmerman, J.M. Rees, Microfluidic rheometry of a polymer solution by micron resolution particle image velocimetry: a model validation study, *Meas. Sci. Technol.* 20 (2009) 115404
- [35] S.J. Gibbs, K.L. James, L.D. Hall, D.E. Haycock, W.J. Frith, S. Ablett, Rheometry and detection of apparent wall slip for Poiseuille flow of polymer solutions and particulate dispersions by nuclear magnetic resonance velocimetry, *J. Rheol.* 40 (1996) 425-440
- [36] S.J. Gibbs, D.E. Haycock, W.J. Frith, S. Ablett, L.D. Hall, Strategies for Rapid NMR Rheometry by Magnetic Resonance Imaging Velocimetry, *J. Magnetic Resonance* 125 (1997) 43-51
- [37] M. Kato, T. Takahashi, M. Shirakashi, Steady planar elongational viscosity of CTAB/NaSal aqueous solutions measured in a 4-roll mill flow cell, *J. Society of Rheology, Japan* 30 (2002) 283-287
- [38] S. Schuberth, H. Münstedt, Simultaneous measurements of velocity and stress distributions in polyisobutylenes using laser-Doppler velocimetry and flow induced birefringence, *Rheol Acta* 47 (2008) 111-119
- [39] F. Gibouin, S. Jarny, P. Monnet, J.C. Dupré, V. Valle, Coupled measurements of PIV and photoelasticity on a thixotropic yield stress fluid flow, *Experiments in Fluids* 55 (2014) 1839
- [40] B. Derakhshandeh, D. Vlassopoulos, S.G. Hatzikiriakos, Thixotropy, yielding and

ultrasonic Doppler velocimetry in pulp fibre suspensions, *Rheol. Acta* 51 (2012) 201-214

[41] M. Nielsen, *Reinventing Discovery: The New Era of Networked Science*, Princeton University Press, Princeton, 2011 (M. Nielsen, 高橋洋 (訳), オープンサイエンス革命, 紀伊国屋書店, 東京, 2013)

[42] R. Remesan, J. Mathew, *Hydrological Data Driven Modelling*, Springer, Cham, 2015

## 2.1 Introduction

Flow visualization has long been recognized as a way to capture fluid motion, for example leaves floating on rivers, snow swirling around buildings, and minced vegetables floating on soup. Flow visualization has been sophisticated as an important tool in experimental fluid mechanics, and over the last decades, it has evolved into a quantitative tool, namely particle imaging velocimetry (PIV). Various techniques for flow visualizations of Newtonian fluids, such as water and air, have been described in many published text books. However, in the field of rheology, complex behaviors on flows of non-Newtonian and viscoelastic fluids, such as milk and paint, are often invisible because of opaqueness. Therefore, approaches using flow visualization have been inhibited and less popular to date. Rheologists focus on measurement of rheological properties in various substances and numerically visualize entire flow structures with CFD to understand the influence of the properties. Experimental flow visualization is always desirable to validate the effective range and universality of rheological properties and models. In the point of view of the fluid mechanics, flow fields reflect all physical properties of fluids and the physical effects acting in a fluid. Therefore, the experimental visualizations of velocity and strain field, which represent momentum transfer and material deformation, should be able to provide intuitive images that capture the flow characteristics of rheological fluids.

Some visualization techniques are applicable to opaque fluids, such as ultrasonic velocity profiling (UVP) [1-4], ultrasonic echo image processing [5], X-rays [6,7], neutron radiography [8] and NMRI [9]. Except for ultrasonic applications, these techniques require special facilities and licenses and, therefore, their use is available only to a very few researchers. In contrast, ultrasonic techniques are widely available than other techniques and are radiation free. In particular, UVP can be easily implemented: basically, all that is required is attaching an ultrasonic transducer to a wall of flow facilities. In addition, because of its fast-signal analysis, UVP is capable of monitoring instantaneous velocity profiles such as flow field visualization. To date, UVP has a wide range of application fields, as summarized in the book by Takeda [4]. Because of its wide applicability, UVP has already been applied to characterization of non-Newtonian fluids [10-12]. The measurable property is still limited to shear-rate-dependent viscosity under steady flows, but this work suggests future potential uses of UVP in rheology.

In this paper, we propose a UVP-based visualizer for capturing the characteristics

of viscoelastic fluid motions. Flow fields contain rich information about fluid properties and fluid mechanics. Therefore, the present flow visualizer provides information that is familiar to general researchers and intuitive images about flow characteristics of rheological fluids, rather than just specific values for rheological properties, which has commonly been done in rheology. Further, with the help of knowledge about rheology, this visualizer would be an effective tool for estimating rheological properties at industrial sites, like interpretations of radiograms at the medical front.

As the first step in system development, we have devoted most of our efforts to investigating viscoelastic fluids. Because flow behaviors of viscoelastic fluids change depending on the flow system, selection of the system determines the success of development. We adopt rotating flows in a cylinder as the flow system, because such a system achieves simple one-dimensional flows and allows wide variations in rotation. The viscoelastic nature of fluids is emphasized in unsteady flows. Thus, we employ three different rotation tests: (a) sudden starts from a stationary state (spin-up), (b) sudden stops from steady-state rotation (spin-down), and (c) periodic oscillations. To highlight the viscoelastic behavior of the fluid, we developed three ways of visualization: (1) direct flow field visualization in the cylinder, (2) strain field visualization, and (3) shear rate field visualization. On the results of visualizations for three test fluids (a viscous silicone oil, a polyacrylamide (PAA) solution, and yogurt), we explain how to capture viscoelastic characteristics.

## 2.2 Experimental setup

To observe the viscoelastic motions of fluids, we used a cylindrical container having a height of 300 mm and an inside diameter of 154 mm. A schematic top view of the container is shown in Fig. 2.1. A stepping motor was connected to the bottom to rotate the whole cylinder. The container was filled with a test fluid and covered by a lid. An ultrasonic transducer for UVP with 2 MHz in the basic frequency was installed at the position indicated in Fig. 2.1, 150 mm from the bottom and  $d = 7$  mm horizontally from the center line. This horizontal displacement from the center line makes it possible to obtain the radial profiles of the azimuthal velocity component. The cylindrical container and ultrasonic transducer were settled in a rectangular container filled with water to improve the transmission rate of ultrasonic waves and to prevent multiple reflections of ultrasonic waves from cylindrical walls. As UVP device, a commercial system, UVP-DUO (Met-Flow, S.A.) was adopted for signal processing. Each measurement volume has a thin disk shape with 0.98 mm in thickness. The diameter of the measurement volume changes depending on the position because of divergence of the

ultrasonic beam, and ranges from 10 to 20 mm. There is a near-field region, where the ultrasonic beam is unstable, from the front of the transducer to 33.8 mm, and we omit the velocity information obtained at the corresponding positions.

Placing the measurement line off the center line of the cylinder ( $d$  in Fig. 2.1) enables us to obtain the azimuthal velocity component. Velocities measured on the line contain both radial velocity component,  $u_r$ , and circumferential velocity component,  $u_\theta$ . Assuming the axial symmetry of the flows, these velocity components can be extracted from the following formulae:

$$u_\theta = \frac{u_{x, far} + u_{x, near}}{2 \cos \alpha}, \quad (2.1)$$

$$u_r = \frac{u_{x, far} - u_{x, near}}{2 \sin \alpha}, \quad (2.2)$$

where  $u_{x, far}$  and  $u_{x, near}$  represent the velocities measured at the far side and the near side halves of the cylinder by UVP and  $\alpha$  is the angular coordinate of the measurement point against the center of the cylinder, as shown in Fig. 2.1.

Three test fluids were used in the experiments: silicone oil (Shin-Etsu Chemical, KF96-1000cs), 0.5 wt% polyacrylamide (PAA) solution (Dia-Nitrix, AP825C), and yogurt (Meiji, LB81 plain). Silicone oil is regarded as a Newtonian fluid with a viscosity of 0.97 Pa·s. The PAA solution has shear-rate-dependent viscosity and viscoelasticity. Figure 2.2 (a), (b) shows the viscosity curve and dynamic moduli, storage modulus  $G'$  and loss modulus  $G''$ , measured with a rotational rheometer MCR301 (Anton Paar). As Fig. 2.2 (a) indicates, PAA solution is shear thinning fluid whose viscosity obeys the power law. At the same time, PAA solution has viscoelasticity. According to Fig. 2.2 (b), storage modulus  $G'$  always exceeds loss modulus  $G''$  in the measurable frequency range. The yogurt is an example of an opaque and viscoelastic fluid with uncertain rheological properties. In silicone oil and PAA solution, resin powders, FLO-BEADS CL-2507 (Sumitomo Seika Chemicals), and DIAION HP20SS (Mitsubishi Chemical) were dispersed, respectively, as ultrasound reflectors. In the yogurt, the fat content reflects ultrasonic waves [13-14], so seeding particles were not needed.

To observe unsteady flows, three patterns of rotation were given to the cylindrical container: rapid start of constant rotation (spin-up), rapid stop from constant rotation (spin-down), and periodic oscillations. In spin-up tests, the container suddenly accelerated at  $t=0$  to the lateral wall speed  $U_{wall} = 101$  mm/s (the corresponding rotation rate was 12.5 rpm). After that, the rotation was suddenly stopped at  $t=5.0$  s (spindown test). The duration time of rotation was long enough for fluids to reach rigid-body

rotation. In the oscillation tests, oscillatory rotation was applied to the container from the initial stationary condition. Time variations of the velocity on the lateral wall are described by

$$U_{osc} = U_0 \sin 2\pi ft, \quad (2.3)$$

where  $U_0$  is the amplitude of velocity (760 mm/s) and  $f$  is the frequency of oscillation (0.5 Hz).

In the conversion of the velocity components from  $u_x$  to  $u_\theta$  and  $u_r$ , measurement errors are amplified through Eqs. (2.1) and (2.2). Error on measured velocity,  $\delta u_x$ , and that on displacement of the transducer,  $\delta d$ , are regarded as predominant error factors. Thus the effect of these errors on the derived  $u_\theta$  and  $u_r$  is assessed. When an quantity  $y$  is derived from experimentally measured quantities  $x_l$  as

$$y = f(x_1, x_2, x_3, \dots, x_l, \dots, x_M), \quad (2.4)$$

measurement error on  $y$ ,  $\delta y$ , is described as following

$$\delta y = \pm \sqrt{\sum_{l=1}^M \left( \frac{\partial f}{\partial x_l} \delta x_l \right)^2}, \quad (2.5)$$

where  $\delta x_l$  are errors on the measured quantities  $x_l$ . According to Eqs. (2.1), (2.2) and (2.5), error on circumferential velocity component,  $\delta u_\theta$ , and that on radial velocity component,  $\delta u_r$ , are described as

$$\delta u_\theta = \pm \sqrt{\left( \frac{\partial u_\theta}{\partial u_{x, far}} \delta u_x \right)^2 + \left( \frac{\partial u_\theta}{\partial u_{x, near}} \delta u_x \right)^2 + \left( \frac{\partial u_\theta}{\partial d} \delta d \right)^2}, \quad (2.6)$$

and

$$\delta u_r = \pm \sqrt{\left( \frac{\partial u_r}{\partial u_{x, far}} \delta u_x \right)^2 + \left( \frac{\partial u_r}{\partial u_{x, near}} \delta u_x \right)^2 + \left( \frac{\partial u_r}{\partial d} \delta d \right)^2}, \quad (2.7)$$

respectively. As partial differentials in Eqs. (2.6) and (2.7) are derived from Eqs. (2.1) and (2.2),  $\delta u_\theta$  and  $\delta u_x$  are described as following

$$\delta u_\theta = \pm \sqrt{\frac{r^2}{2d^2} \delta u_x^2 + \left[ \frac{u_{x, far} + u_{x, near}}{2} \left( \frac{x}{\xi r} - \frac{r}{d^2} \right) \right]^2 \delta d^2}, \quad (2.8)$$

$$\delta u_r = \pm \sqrt{\frac{1}{2} \frac{r^2}{r^2 - d^2} \delta u_x^2 + \frac{1}{4} \left( \frac{d}{\xi} \right)^2 (u_{x, far} - u_{x, near})^2 \frac{r^2 - d^2}{r^2} \left[ \frac{xd^2 - \xi r^2}{(r^2 - d^2)^2} \right]^2 \delta d^2}, \quad (2.9)$$

where  $x$  is spatial axis along the measurement line of UVP whose origin is on the wall of the outer cylinder, and  $\xi$  is distance from the origin to the nearest point to the center

on  $x$  axis, namely

$$\xi = \sqrt{R^2 - d^2}. \quad (2.10)$$

Figure 2.3 shows spatial distribution of  $u_\theta \pm \delta u_\theta$  and  $u_r \pm \delta u_r$ . Error enhancement depends on velocity distribution as Eqs. (2.8) and (2.9) indicate. Thus error distribution under rigid-rotation flow is shown in Fig. 2.3 as an example. The velocity of the wall is set as the same value as the experimental condition:  $U_{wall} = 101$  mm/s. The error on the position of the transducer,  $\delta d$  in Eqs. (2.8) and (2.9), is assumed to be 0.5 mm, which is a half value of minimum scale of the ruler to fix the position. As the error on the velocity,  $\delta u_x$ , velocity resolution of UVP is employed:  $\delta u_x = 0.78$  mm/s. According to Fig. 2.3,  $\delta u_\theta$  is large near the outer cylinder while  $\delta u_r$  is large near the center of the cylinder. Because the angle between  $x$  axis and  $u_\theta$ , which equals to  $\alpha$  in Fig. 2.1, is large near the outer cylinder,  $\delta u_x$  is remarkably amplified through the conversion with Eq. (2.1). Near the center, on the other hand,  $\delta u_x$  is remarkably amplified through Eq. (2.2), and thus  $\delta u_r$  is estimated to be large there.

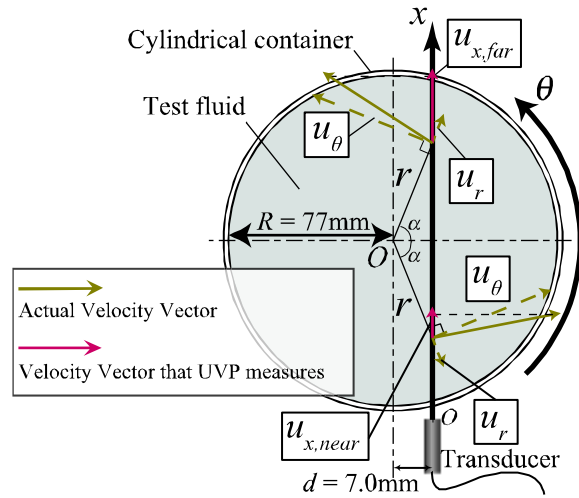


**Figure 2.1** Experimental apparatus

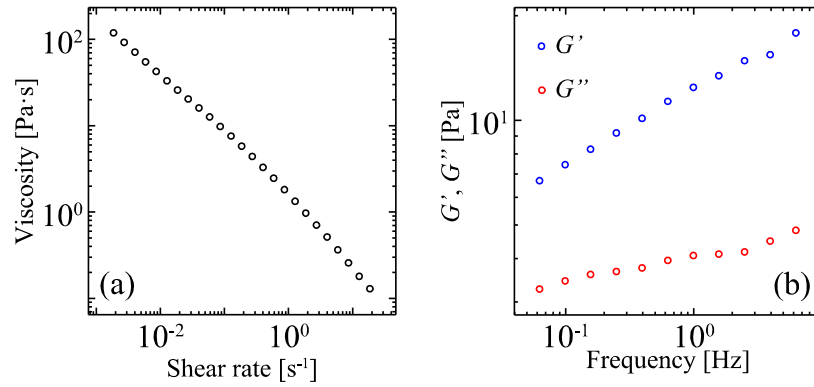


**Figure 2.2** (a) Shear-rate-dependent viscosity and (b) storage and loss moduli of 0.5 wt% PAA solution measured with rotational rheometer

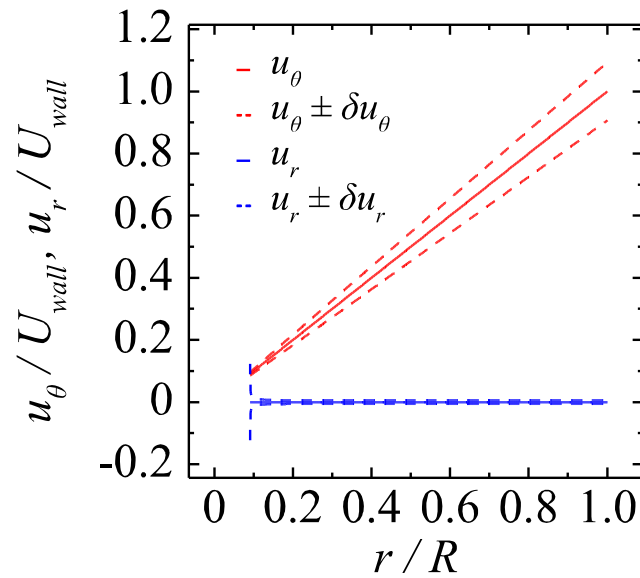


**Figure 2.3** Errors on  $u_\theta$  and  $u_r$  caused by measurement noise on velocity  $\delta u_x$  and displacement of the transducer  $\delta d$

### 2.3 Spatio-temporal distributions obtained by UVP

For each of the three test fluids, Figs. 2.4 and 2.5 show the profiles of the circumferential velocity component  $u_\theta$  and radial velocity component  $u_r$ , calculated from Eqs. (2.1) and (2.2), respectively. The velocity components are obtained for the three tests: spin-up, spin-down, and oscillation. In all velocity maps, the radial coordinate has been normalized by the radius of the cylindrical container  $R = 77$  mm. In the spin-up and spin-down tests, the color code for  $u_\theta$  was set to drastically change at  $u_\theta = 0$ ; this emphasizes the appearance of negative velocities that appear as the result of fluid elasticity. We can observe deep-purple stripes before the rotation when the fluid should be stationary, but their magnitudes correspond to several fold of velocity resolution. So, we assume that these are noise due to the measurement characteristics for stationary fluid. In the spin-up and spin-down tests, the velocities were normalized by the velocity of the lateral wall ( $U_{wall} = 101$  mm/s); in oscillation tests, they were normalized by the amplitude of the wall velocity ( $U_\theta = 760$  mm/s). Velocities near the wall ( $r/R > 0.9$ ) could not be captured, because the ultrasound beam could not be focused enough. Multi-reflection of the ultrasound beam in the cylindrical wall also prevents velocity profiling.

Figs. 2.4 and 2.5 show that the fluids move almost to the circumferential direction. The radial velocity component  $u_r$  is one orders of magnitude less than the circumferential velocity component  $u_\theta$ . Thus rheological properties of the test fluids are read out from the distribution of circumferential velocity component  $u_\theta$  shown in Fig. 2.4. In spin-up tests shown in the left panels of Fig. 2.4, the cylinder begins to rotate at  $t = 0$ . At first, the lateral wall, which has the non-slip condition against the fluid, induces azimuthal motion of fluid near the wall. Then, azimuthal momentum transferred from the wall to the fluid propagates to the core fluid region by viscous diffusion. After that, the fluid motion reaches rigid-body rotation, which is the terminal condition of spin-up tests. Momentum propagation appears as a contour line in velocity profiles as a dotted line in the left panel of Fig. 2.4 (a). The angle between the contour line and the horizontal axis represents the speed of momentum propagation, which is determined by the viscosity of the test fluid: larger angles indicate larger viscosities. For yogurt, the left panel in Fig. 2.4 (c) shows that the speed of propagation depends on the radial position. Near the wall,  $r/R > 0.7$ ; it takes time for the momentum to propagate. But in the core region of the fluid, the contour lines are almost vertical. This means that the yogurt in the core region remains in a rigidbody state even while accelerating. This observed behavior is consistent with the fact that yogurt has yield stress as it changes from a solid-like state to fluid. Near the wall, the shear stress exceeds the yield stress

because of the strong shear, and the yogurt behaves like a fluid. However, in the core region, the shear stress is less than the yield stress, and the yogurt behaves like a solid.

In the spin-down tests, the cylinder stopped rotating at  $t = 5.0$  s. Until just before the stop, fluids rotated rigidly, but after the cylinder stopped, test fluids were decelerated by the lateral wall. Elastic behavior was most clearly observed in spin-down tests. Reverse flows were observed at  $t > 7.0$  s for the PAA solution and at  $6.0 < t < 6.5$  s for the yogurt. These reverse flows must be caused by elasticity because the lateral wall does not introduce any momentum in the negative direction. Moreover, reverse flows were not observed in silicone oil, which is regarded as an inelastic fluid. Velocity profiles during deceleration in spin-down tests indicate that kinetic energy is stored as elastic energy in viscoelastic fluids, and the fluid is driven in the negative direction when that elastic energy is reconverted to kinetic energy.

In the oscillation tests, oscillatory motion was applied to the cylinder in accordance with Eq. (2.3) starting at  $t = 0$ . The right panel of Fig. 2.4 (a) shows that the velocity profile for silicone oil displays sinusoidal oscillations at each position. The frequency of the velocity fluctuations is almost the same as that of the lateral wall ( $f = 0.5$  Hz). This means that there are no non-linear interactions during momentum propagation in the oil. The amplitude of the velocity is large near the lateral wall. However, silicone oil in the core region has a phase lag relative to the lateral wall, as indicated by the dotted line in the right panel of Fig. 2.4 (a). This phase lag depends on the viscosity: the dotted line would tilt to the horizontal axis if the viscosity of the fluid is small, but it would tilt to the vertical axis if the viscosity is large. For the PAA solution, the time variations in velocity deviate from a simple sinusoidal curve. This is because of viscoelasticity. After a sufficiently long time, the time variations in velocity converge to a sinusoidal curve. On the basis of the phase lag, the viscosity of the PAA solution is small near the lateral wall and large near the center, as the dotted line in Fig. 2.4 (b) indicates. This spatial variation of the viscosity is consistent with shear thinning of the PAA solution; in shear thinning fluids, the viscosity decreases as the shear acting on the fluid increases. For yogurt, the time variations in velocity are almost sinusoidal. The differences between the velocity profiles of the yogurt and silicone oil are the phase lags at different positions. In yogurt, the phase lag is small, especially during the initial cycle because the yogurt remains in a rigid-body state during the initial cycle of the oscillation. In the second cycle, the dotted line tilts more horizontally than in the initial cycle. This behavior suggests a decrease in viscosity. The stress acting on the yogurt exceeds the yield stress in the oscillation; therefore, the viscosity changes from infinity (i.e., a solid state) to a finite value after yielding.

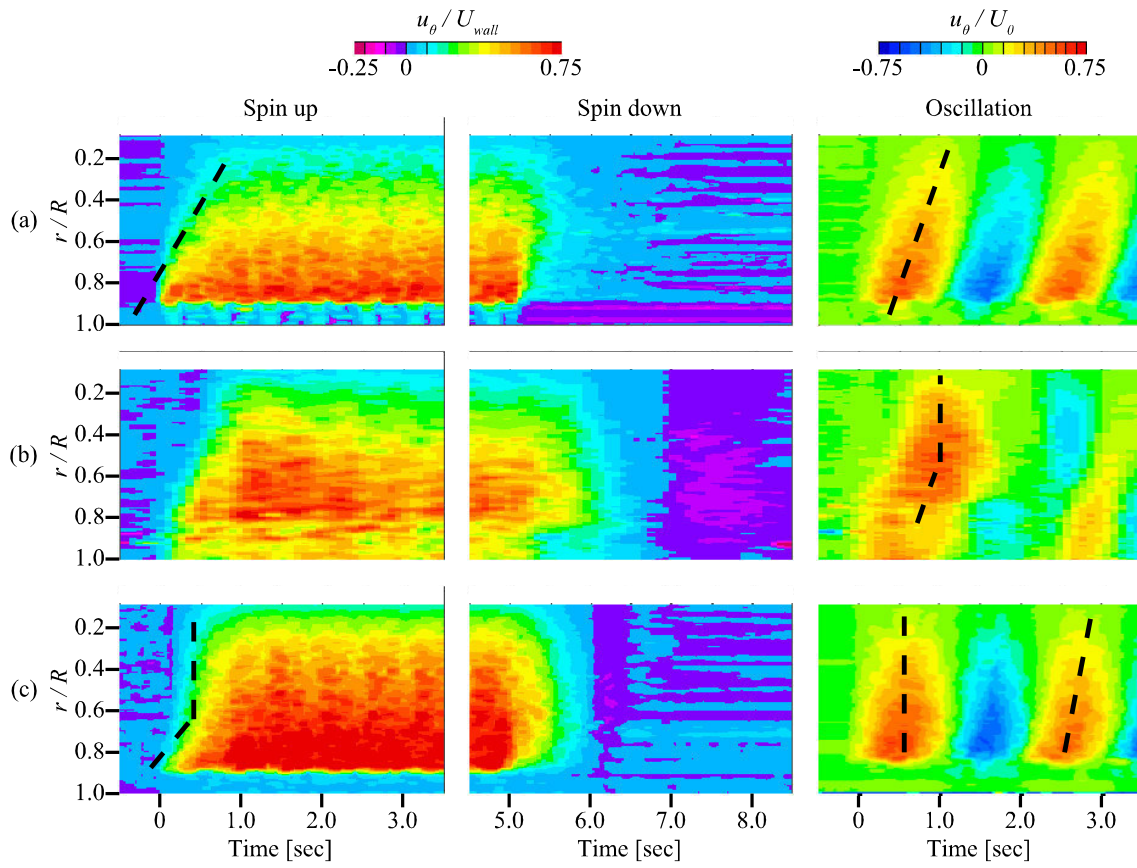


**Figure 2.4** Circumferential velocity components of (a) silicone oil, (b) PAA solution, and (c) yogurt under three rotational conditions (spin-up, spin-down, and oscillation)

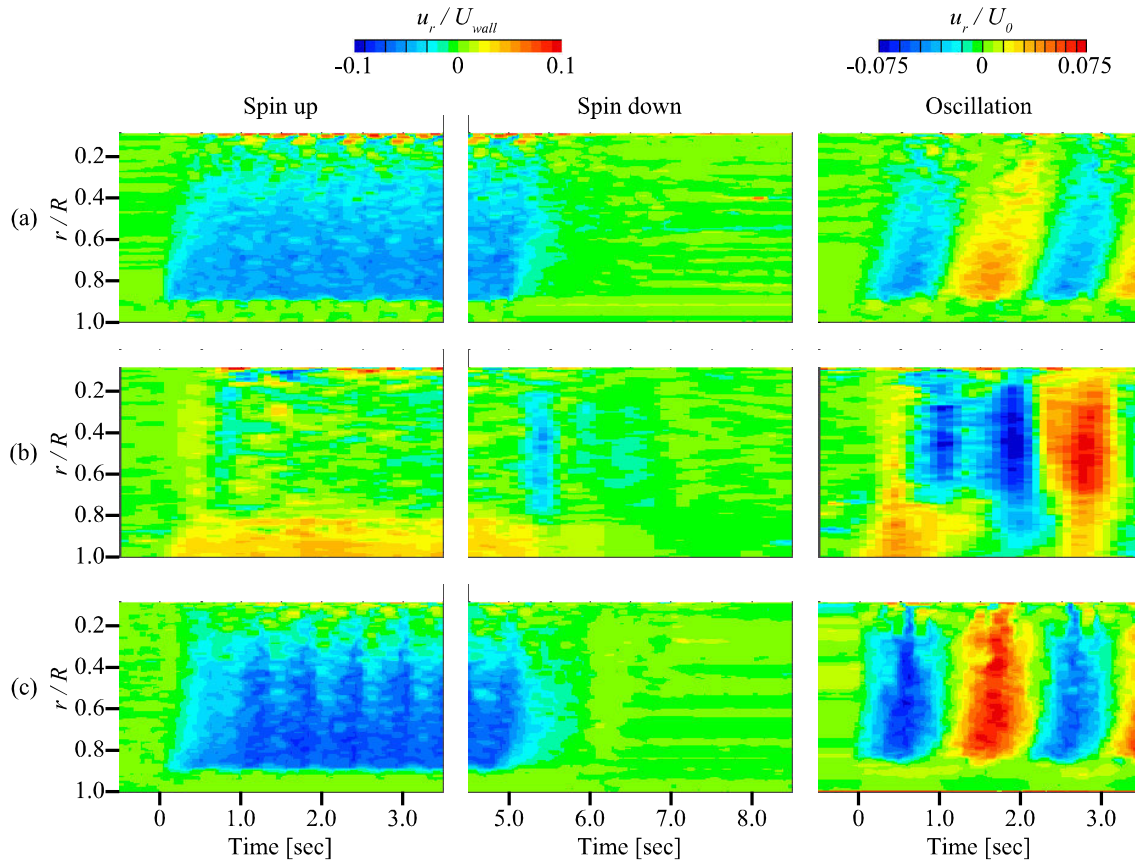


**Figure 2.5** Radial velocity components of (a) silicone oil, (b) PAA solution, and (c) yogurt under three rotational conditions (spin-up, spin-down, and oscillation)

## 2.4 Visualization of fluid motion

### 2.4.1 Vector expressions of velocity for intuitive understanding

Spatio-temporal velocity maps, such as those in Figs. 2.4 and 2.5, contain full information about flow characteristics and fluid properties. However, those maps do not provide direct images of fluid motions in real physical coordinates. The displays of velocity vector profiles are a better way of visualization for intuitive understanding. Figures 2.6, 2.7, and 2.8 show velocity vector fields at select times during the spin-down of the silicon oil, PAA solution, and yogurt, respectively. The corresponding spatio-temporal velocity distributions are shown in the center panel of Fig. 2.4. As described by Eq. (2.1) and (2.2), both circumferential and radial velocity components,  $u_\theta$  and  $u_r$ , can be derived from spatio-temporal velocity profiles provided by UVP. Both velocity components are displayed as the vector fields in Figs. 2.6, 2.7, and 2.8. Those figures show that the radial component  $u_r$  is negligible compared to the circumferential component  $u_\theta$ . Hence, only  $u_\theta$  is taken into account in the two visualization modes described in the following sections.

For the spin-down tests, Figs. 2.6 (a), 2.7 (a), and 2.8 (a) indicate velocity vector fields at  $t = 5.0$  s, at which the rotation of the cylinder is just stopped after the flow reaches the rigid-body rotation. The linear trend in vector length vs. radial position indicates that all three fluids remain in rigid-body rotation at the time. After that, the fluids are decelerated by the lateral wall. Figure 2.6 (c), (d), (e) provides clear images of the deceleration process in silicone oil: velocities are small near the wall, and a maximum velocity occurs near  $r/R = 0.5$ . After deceleration, the velocities reach zero all along the radial positions, as shown in Fig. 2.6 (f). The PAA solution follows a deceleration process that is similar to that of silicone oil until the velocities first become zero at Fig. 2.7 (d), but then, unlike silicone oil, reverse flows due to elasticity appear as shown in Fig. 2.7 (e). After that the PAA solution displays oscillations around zero velocity with decreasing amplitudes until finally the flow reaches a stationary state, as shown in Fig. 2.7 (f). Unfortunately, cycles in oscillations after the initial one cannot be distinguished on the velocity vector profile, because their small velocities were buried in measurement noise. For the yogurt, deceleration was similar to that of the PAA solution: velocities first become zero in Fig. 2.8 (d) and then reverse flows appear in Fig. 2.8 (e). However, the duration of reverse flow of the yogurt was shorter than that of the PAA solution, suggesting that yogurt has larger elasticity than the PAA solution. The reverse flows of the PAA solution and yogurt were due to elastic energy stored in those viscoelastic fluids. If the test fluid is a perfect elastic body, the stored elastic energy is proportional to the square of the strain. It is possible to imagine how much and where the elastic energy is stored by watching the strain fields. In the next section, deformations of a grid pattern, which represents fluid deformations, are calculated from the velocity profiles in Fig. 2.4. Those deformations provide semi-quantitative visualizations of the strain and help us grasp the elastic energy distribution.

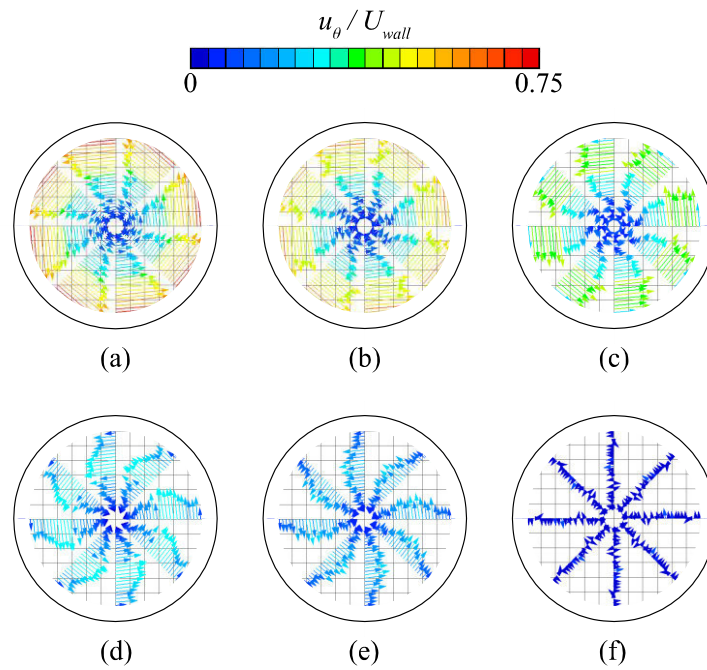


**Figure 2.6** Velocity vector fields of silicone oil in the spin-down process at these times:  $t =$  (a) 5.00 s, (b) 5.06 s, (c) 5.12 s, (d) 5.23 s, (e) 5.35 s, and (f) 6.34 s

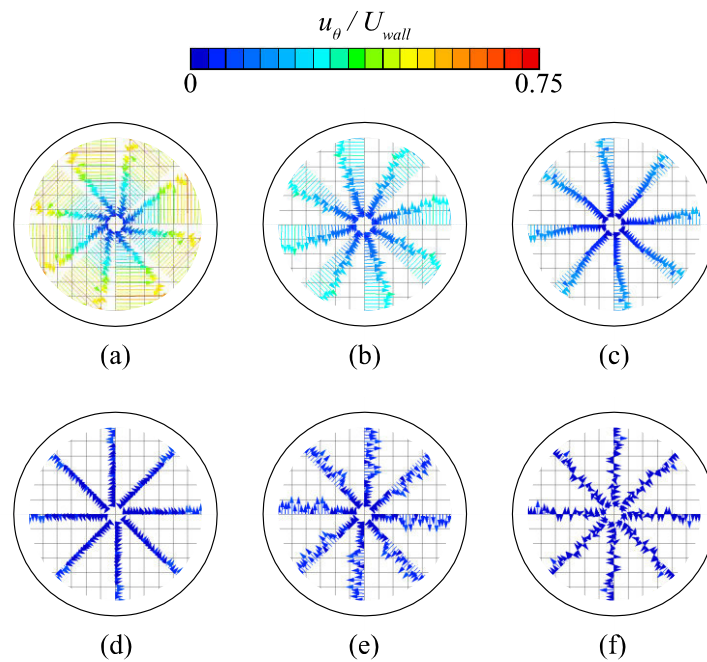


**Figure 2.7** Velocity vector fields of the PAA solution in the spin-down process at these times:  $t =$  (a) 5.00 s, (b) 5.98 s, (c) 6.25 s, (d) 6.60 s, (e) 7.40 s, and (f) 8.56 s

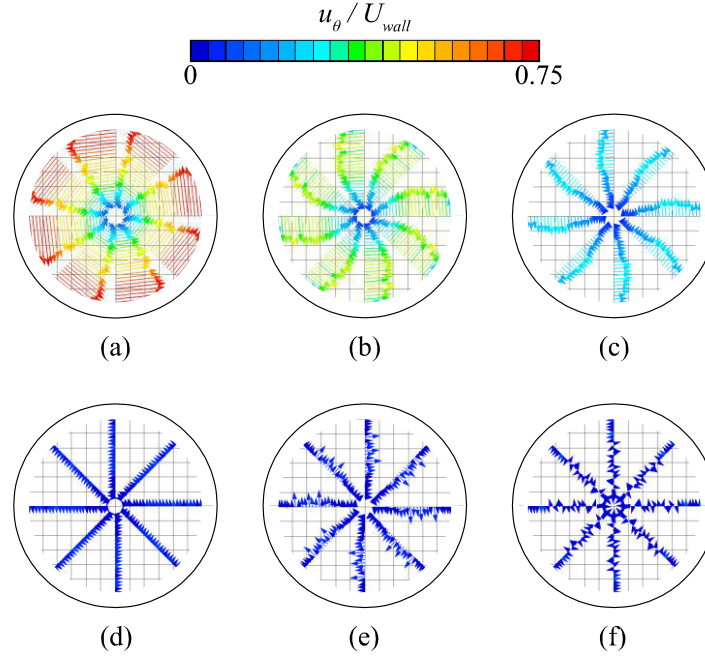


**Figure 2.8** Velocity vector fields of yogurt in the spin-down process at these times:  $t =$  (a) 5.00 s, (b) 5.23 s, (c) 5.49 s, (d) 5.88 s, (e) 6.14 s, and (f) 6.56 s

#### 2.4.2 Visualization of fluid deformation with grid expression

Because elastic stress and stored elastic energy are determined by strain, visualizing the strain field has great importance in the discussion of viscoelasticity. In spin-down tests, reverse flows, caused by stored elastic energy, were observed. Therefore, we visualized the strain field during spin-down tests by calculating how grid patterns are deformed by fluid motion. The calculated deformations are shown in Figs. 2.9, 2.11, and 2.12, for silicone oil, PAA solution, and yogurt, respectively. The initial conditions were defined by the undeformed grids shown in (a) of each figure at  $t = 5.0$  s. From this initial condition, cross points are moved according to the velocity profile shown in Fig. 2.4: circumferential positions of cross points  $\theta(t)$  are determined by

$$\theta(t) = \int_{t_{stop}}^t \frac{u_{\theta}(t')}{r} dt', \quad (2.11)$$

where  $t_{stop}$  means time when the rotation of the cylinder is stopped:  $t = 5.0$  s. The moved points are connected by straight lines. At the initial condition, the test fluids were rigidly rotating without any stress. Thus, the calculated deformations represent deviations from the initial stress-free state. Under this expression, viscous characteristics appear as the deformation remaining at the terminal state, whereas elastic characteristics appear as the recovery from the deformed state. Time variations in the deformations are shown in the image sequence from (a) to (f) in Figs. 2.9, 2.10, and 2.11. Parts of each sequence are

superposed in (g), where grid patterns at each time step are displayed with a different color.

Even after the wall is stopped, fluids move in the circumferential direction because of inertia. This produces a velocity gradient against the stationary cylinder wall and thus the fluids near the wall are deformed, as shown in Fig. 2.9 (b). Then the inner fluid is deformed while being stopped. Thus, silicone oil is deformed at all radial positions when the fluid is completely stopped, as shown in Fig. 2.9 (f). If a perfect elastic body experiences this same deformation, the fluid moves in the negative direction and continues to oscillate forever. However, silicone oil does not exhibit any reverse flow, as shown in Fig. 2.4 (a). This indicates that silicone oil does not have elasticity, and all the initial kinetic energy in Fig. 2.9 (a) is converted to thermal energy. In the stationary condition, shown in Fig. 2.9 (f), all the kinetic energy has been converted to thermal energy.

In contrast, the deceleration processes of the PAA solution and yogurt are not monotonic. For example, for the PAA solution, the fluid near the wall is deformed at first, as shown in Fig. 2.10 (b). Then, the velocity first becomes zero at all radial positions in Fig. 2.10 (e). The reverse flow induced by the release of elastic energy occurs at a time between Fig. 2.10 (e) and (f). The strain in Fig. 2.10 (e) partially recovers and finally converges to the stationary terminal state, as in Fig. 2.7 (f). The reverse flow and the recovery of the deformation can be clearly seen in Fig. 2.10 (g) as the variation from (e) to (f). The yogurt undergoes deceleration similar to the PAA solution: the yogurt is first deformed near the wall (Fig. 2.11 (b)), then stops the first time (Fig. 2.11 (e)), and recovers slightly (from Fig. 2.11 (e), (f)). The magnitudes of the relaxations in deformations from (e) to (f) in Figs. 2.10 and 2.11 should be a measure of the degree of elasticity, because the distance is determined by the stored elastic energy. According to this, the PAA solution is more elastic than the yogurt.

As already mentioned, a perfectly elastic fluid should oscillate forever in spin-down tests. However, in the present experiments, the fluids lose kinetic energy and reach a stationary state while maintaining the deformation. This means that a large part of the initial kinetic energy is not stored as elastic energy, but dissipated as thermal energy. One factor that determines the amount of energy dissipation is the shear rate. Thus, to estimate the magnitude of viscous energy dissipation, the shear rate distribution is visualized in the next section.

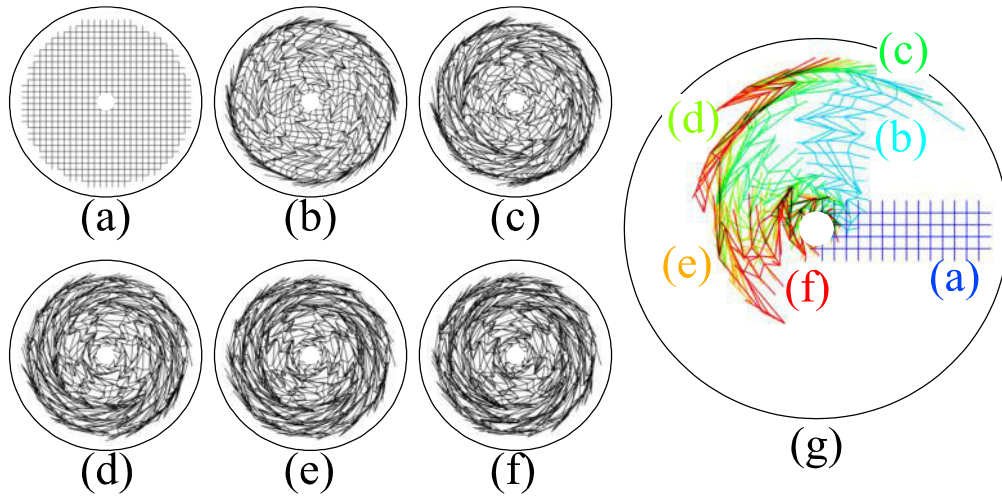


**Figure 2.9** Deformation of grid pattern for silicone oil in the spin-down process at these times:  $t =$  (a) 5.00 s, (b) 5.23 s, (c) 5.46 s, (d) 5.70 s, (e) 5.93 s, and (f) 6.13 s. Parts of the grids are superposed in (g)

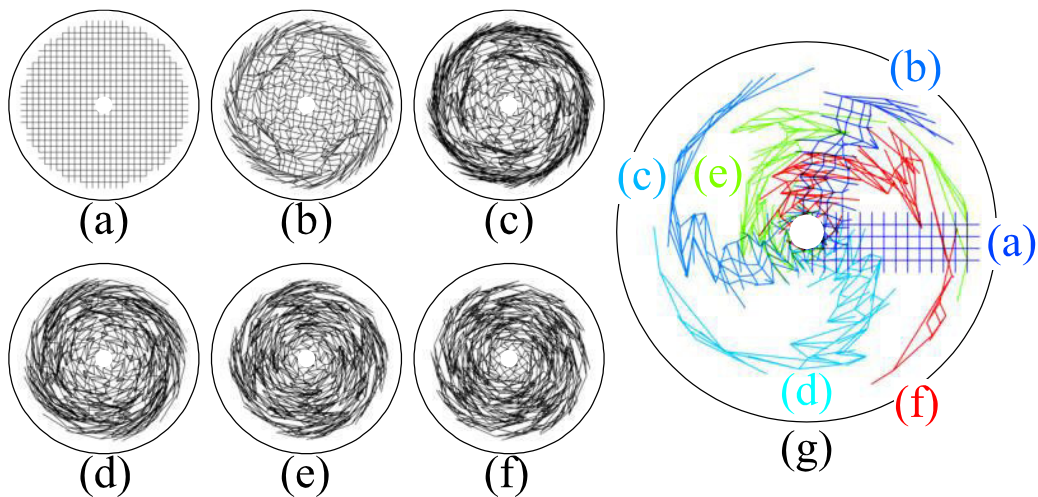


**Figure 2.10** Deformation of grid pattern for the PAA solution in the spin-down process at these times:  $t =$  (a) 5.00 s, (b) 5.18 s, (c) 5.45 s, (d) 5.71 s, (e) 7.14 s, and (f) 8.56 s. Parts of the grids are superposed in (g)

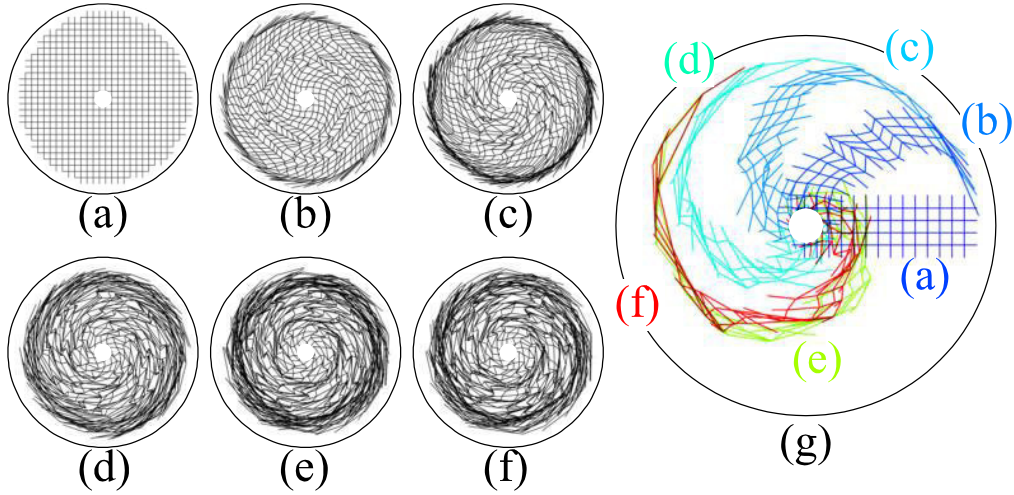


**Figure 2.11** Deformation of grid pattern for yogurt in the spin-down process at these times:  $t =$  (a) 5.00 s, (b) 5.10 s, (c) 5.23 s, (d) 5.44 s, (e) 6.01 s, and (f) 6.59 s. Parts of the grids are superposed in (g)

### 2.4.3 Simultaneous visualization of fluid motion and shear rate

In Sect. 2.4.2, we visualized the strain distribution, which is related to stored elastic energy. On the other hand, viscosity causes the energy dissipation that occurs in high-amplitude shear rate regions. Therefore, to understand how viscosity contributes to the motion of fluids, we now visualize the shear rate distribution in spin-down tests. Figures 2.12, 2.13, and 2.14 present images of the shear rate distribution. In those figures, the colors indicate the local shear rate, which was calculated by

$$\dot{\gamma} = \frac{\partial u_{\theta}}{\partial r} - \frac{u_{\theta}}{r}, \quad (2.12)$$

Shear rates were normalized by the characteristic shear rate, which is defined by

$$\dot{\gamma}_c = \frac{U_{wall}}{R}, \quad (2.13)$$

As shown in Eq. (2.12), the calculation requires the differential of the experimental velocity. Often, such differentials are numerically estimated using a simple finite difference. However, in this case a finite difference enhances noise in the measurements. To avoid amplifying the noise, least square fitting was applied to the data: velocity gradient in Eq. (2.12) was calculated by

$$\left(\frac{\partial u_\theta}{\partial r}\right)_i = \frac{(2n-1) \sum_{j=i-n}^{i+n} r_j u_{\theta j} - \sum_{j=i-n}^{i+n} r_j \sum_{j=i-n}^{i+n} u_{\theta j}}{(2n-1) \sum_{j=i-n}^{i+n} r_j^2 - \left(\sum_{j=i-n}^{i+n} r_j\right)^2}, \quad (2.14)$$

where  $2n + 1$  corresponds to the spatial range for the fitting. In the figures,  $n$  was set as 20. This indicates that structures smaller than 10 mm cannot be resolved in the figures. This spatial range is smaller than the energy dissipating area, yet large enough to reduce local noise caused by finite difference calculation. The strain acting on the fluid is also displayed as particle motions determined by Eq. (2.11). At the initial position, the particles align in the radial direction at  $t = 5.0$  s, as shown in (a) of Figs. 2.12, 2.13, and 2.14. Therefore, both viscous and elastic contributions to the stress are visualized in the same figures.

After the lateral wall was stopped, the fluid near the wall also stopped. However, the fluid far from the wall remained in motion because of inertia. This situation produced negative shear rates, as shown by the blue areas near the lateral walls in Figs. 2.12 (b), (c), 2.13 (b), and 2.14 (b). In these areas, kinetic energy is dissipated as thermal energy. The energy conversion during reverse flow is easily seen in Fig. 2.14 for yogurt. After deceleration caused by the lateral wall, velocities become zero everywhere. Then the shear rate also becomes zero, of course, as shown in Fig. 2.14 (d). However, the fluid still has energy as elastic energy, as shown by the deformed distribution of particles in Fig. 2.14 (d). Thus, the reverse flow and corresponding positive shear rates appear in Fig. 2.14 (e), (f) as yellow rings a little inside from the cylinder wall. Viscoelastic fluids such as yogurt should undergo repeated azimuthal oscillations around zero velocity with decreasing amplitudes, but those small velocities cannot be resolved on the velocity profiles shown here. Thus, the value of the shear rate also should oscillate around zero, and viscous dissipation occurs in the regions of both positive and negative shear rates. While the oscillations continue, the amplitudes of shear rate and velocity decrease. In the terminal state, the shear rate and velocity become zero everywhere because all kinetic energy has been converted to thermal energy.

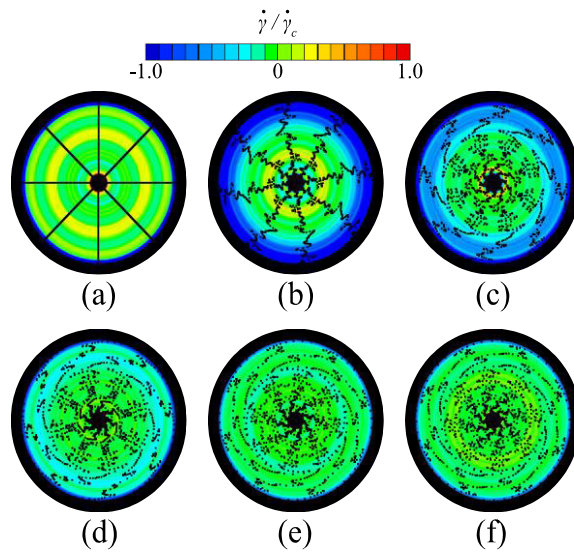


**Figure 2.12** Particle motions (black dots) and shear rates (colors) for silicone oil flows at  $t =$  (a) 5.00 s, (b) 5.15 s, (c) 5.32 s, (d) 5.49 s, (e) 5.67 s, and (f) 5.84 s

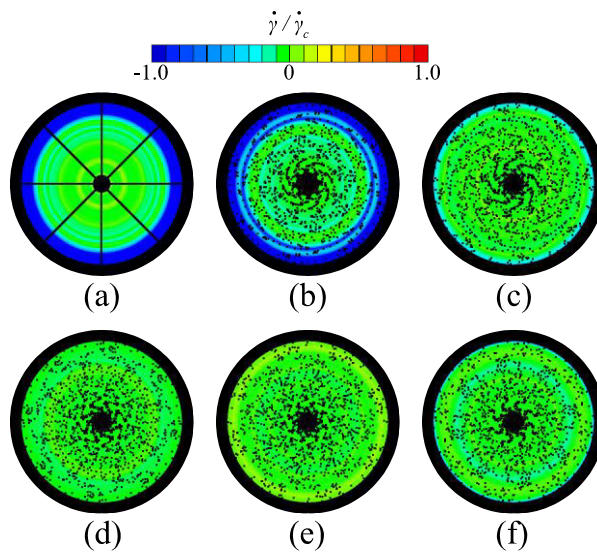


**Figure 2.13** Particle motions (black dots) and shear rates (colors) for PAA solution flows at  $t =$  (a) 5.00 s, (b) 5.62 s, (c) 6.34 s, (d) 7.05 s, (e) 7.76 s, and (f) 8.47 s

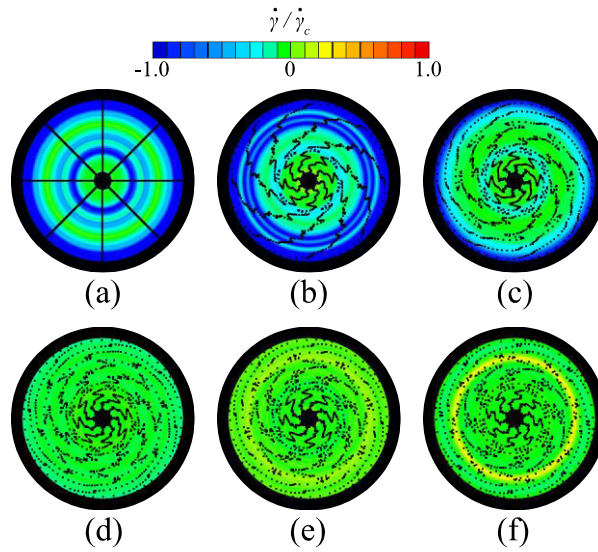


**Figure 2.14** Particle motions (black dots) and shear rates (colors) of yogurt flows at  $t =$  (a) 5.00 s, (b) 5.29 s, (c) 5.60 s, (d) 5.91 s, (e) 6.22 s, and (f) 6.53 s

## 2.5 Conclusion

With the aim of obtaining intuitive images of characteristic flows induced by viscoelasticity, we developed an ultrasonic visualizer for the flows of viscoelastic fluids. The system consists of an ultrasonic velocity profiler (UVP) and a cylindrical container that can undergo various rotational modes. To highlight viscoelastic behavior, we applied three display modes (velocity vector profiles, fluid deformations, and shear rate distributions) to data taken from three rotational modes (spin-up, spin-down, and oscillation). For evaluating the applicability of the visualizer, three fluids were examined: two non-Newtonian fluids having different elasticities (a polyacrylamide (PAA) solution and yogurt) and, for comparison, an inelastic Newtonian fluid (silicone oil). The use of yogurt also emphasized the ability of the visualizer to provide images from opaque fluids, because most industrial viscoelastic fluids are opaque.

Before demonstrating the three display modes, we read out essential information about flow characteristics obtained from experimentally determined spatio-temporal velocity maps. Spin-up tests indicated differences in the relative viscosities of the three fluids, and variations of contours on the velocity maps implied yield stresses in the yogurt. Spin-down tests explicitly revealed elastic behavior in the form of reverse flows. These influences were superimposed in the oscillation tests. For capturing viscoelastic effects, the spin-down test is most suitable because of the clear appearance of reverse flows.

Therefore, we demonstrated the three display modes on the basis of the spin-down

tests applied to each of the three fluids. The velocity vector profiles produce intuitive visual understanding of momentum propagation from the wall to the inner fluid and, thus, the users of the visualizer can directly extract magnitudes of relative viscosity and behavior of viscoelastic fluids. A grid pattern display can provide visualized information about fluid deformations that correspond to strain. Strain distributions provide information about the storage of elastic energy, deformations remaining at terminal stationary states, and mean energy dissipations to thermal energy caused by viscosity. Viscous dissipation and the storage of energy are simultaneously visualized in a display of both shear rate distribution and fluid particle motions representing deformation of the fluid. In these three display modes, we restricted the object of the visualizer to viscoelasticity for demonstration purposes in this paper. In fact, the visualizer has wider applicability than what is presented here; for example, it can be adopted for visual detection of complex rheological responses, such as yield stress, shear thinning, or thickening effects.

Flow fields reflect all physical properties of fluids and the physical effects acting on fluids. Therefore, spatio-temporal velocity maps, which contain quantitative information about flow fields, can provide viscoelastic properties of fluids as specific values. However, this cannot be done in the current configuration, because the determination of specific values requires information about stress at the boundaries. We are designing new equipment that consists of the present visualizer and a torque meter; this new device should satisfy the demands of providing intuitive visual images as well as explicit values for physical properties of viscoelastic fluids.

## References

- [1] J. Wiklund, M. Standing, A. J. Pettersson, A. Rasmuson, A comparative study of UVP and LDA Techniques for pulp suspensions in pipe flow, *AIChE J.* 52 (2006) 484-495
- [2] Y. Murai, Y. Tasaka, Y. Nambu, Y. Takeda, S. R. Gonzalez, Ultrasonic detection of moving interfaces in gas–liquid two phase flow, *Flow Meas. Instrum.* 21 (2010) 356–366
- [3] T. Yanagisawa, Y. Yamagishi, Y. Hamano, Y. Tasaka, K. Yano, J. Takahashi, Y. Takeda, Detailed investigation of thermal convection in a liquid metal under a horizontal magnetic field, *Phys. Rev. E* 82 (2010) 056306
- [4] Y. Takeda (ed) (2012) *Ultrasonic Doppler velocity profiler for fluid flow*. Springer, Tokyo
- [5] H. Zheng, L. Liu, L. Williams, J. R. Hertzberg, C. Lanning, R. Shandas, Real time multicomponent echo particle image velocimetry technique for opaque flow imaging, *Appl. Phys. Lett.* 88 (2006) 261915
- [6] S. J. Lee, G. B. Kim, D. H. Yim, S. Y. Jung, Development of a compact X-ray particle image velocimetry for measuring opaque flows, *Rev. Sci. Instrum.* 80 (2009) 033706
- [7] D. Bauer, H. Chaves, C. Arcoumanis, Measurements of void fraction distribution in cavitating pipe flow using X-ray CT, *Meas. Sci. Technol.* 23 (2012) 055302
- [8] A. B. Geiger, A. Tsukada, E. Lehmann, P. Vontobel, A. Wokaun, G. G. Scherer, In situ investigation of two-phase flow patterns in flow fields of PEFC's using neutron radiography, *Fuel Cells* 2 (2002) 92–98
- [9] S. W. Sinton, A. W. Chow, J. H. Iwamiya, NMR imaging as a new tool for rheology, *Macromol. Symposia* 86 (1994) 299–309
- [10] B. Ouriev, E. J. Windhab, Rheological study of concentrated suspensions in pressure-driven shear flow using a novel inline ultrasound Doppler method, *Exp. Fluids* 32 (2002) 204–211
- [11] B. H. Birkhofer, S. A. K. Jeelani, E. J. Windhab, B. Ouriev, K. J. Linsner, P. Braun, Y. Zeng, Monitoring of fat crystallization process using UVP–PD technique. *Flow Meas. Instrum.* 19 (2008) 163–169
- [12] R. Kotze, E. J. Wiklund, R. Haldenwang, Optimization of the UVP plus PD rheometric method for flow behavior monitoring of industrial fluid suspensions, *Appl. Rheol.* 22 (2012) 42760
- [13] J. Wiklund, M. Standing, Application of in-line ultrasound Doppler-based UVP-PD rheometry method to concentrated model and industrial suspensions. *Flow Meas.*

Instrum. 19 (2008) 171–179

[14] J. Wiklund, M. Standing, C. Trägårdh, Monitoring liquid displacement of model and industrial fluids in pipes by in-line ultrasonic rheometry, *J. Food Eng.* 99 (2010) 330–337

### 3.1 Introduction

An important part of polymer and food engineering is the quantification of the rheological properties of non-Newtonian fluids, to predict their fluid flows. The relationship between shear rate and shear stress, which is called “flow curve” in the field of rheology, is commonly used as rheological properties to predict inelastic flows. Conventional rheometers obtain flow curves by measuring the torque that acts on a rotating device at variable shear rates. These rheometers confine the test fluid between concentric cylinders, parallel plates, or a cone-and-plate, and assume a constant shear rate in a narrow gap between cylinders or plates [1]. The corresponding shear stress is derived from the measured torque for a fixed shear rate, and the flow curve is obtained by repeating the torque measurement at a different applied shear rate. Therefore, complete flow curves require relatively long experiments of around 1-h duration. This restricts the rheological investigation of fluids whose properties vary sharply with time, such as thixotropic or oxidizing materials. The assumption of constant shear rate in the fluid layer requires a sufficiently narrow gap, which inhibits the assessment of fluids that possess a large spatial fluctuation of a specific rheological property, e.g., a multiphase medium. Furthermore, even if the gap is narrow enough, some special fluid cases can still produce measurement errors, such as shear banding [2], shear localization [3], and coexistence of yielding and unyielding region.

The limitations of the rheometry assuming constant shear rate is overcome by solving a problem called “Couette inverse problem”, where flow curve is derived in concentric cylinder configuration without assuming constant shear rate. The original data measured with rheometer is the relationship between rotational speed of the inner cylinder  $\Omega$  and shear stress on the inner cylinder wall  $\tau_{wall}$ . To derive a flow curve from  $\tau_{wall}(\Omega)$ , various techniques have been presented, for example introducing rheological models [4-7], mathematical functions [8-11], Tikhonov regularization [12] and wavelet-vaguelette decomposition [13]. These previous researches allow that shear rate have distribution. Thus yield stress can be obtained by causing the flow where yielding and unyielding regions coexists. Concentric cylinders with a large gap are preferred configuration to satisfy this condition.

Another way to allow shear rate distribution is utilization of velocity profiling. Features of the recent rheometries introducing velocity profiling are summarized in Table 3.1. The measurement system developed by Ouriev and Windhab [14-16] and

Wiklund *et al.* [17-19] adopted a pipe-flow configuration and velocity profiling to measure the flow curves of fluids made up of large-sized components. Concentric cylinders were introduced to determine the rheological properties when subjected to a non-uniform shear rate [20-22]. All of these studies introduced velocimetry; either ultrasonic velocity profiling (UVP) [14-19,21,22], particle imaging velocimetry [23-25], or laser Doppler velocimetry (LDV) [17]. In most cases, the measured velocity distributions were approximated with continuous functions to derive the velocity gradient. This was to avoid noise amplification in numerical derivatives. The approximation functions of these methods were chosen based on rheological models that make prior assumptions about the rheological characteristics of the fluid under examination. Substituting the constitutive equations into the equation of motion of fluids provides the corresponding velocity profiles for the approximation function. For example, the power law model [14-16,19], the Casson model [20], and the Herschel-Bulkley model [14,17,18,21] were introduced as rheological models for various test fluids.

Between the two approaches to allow shear rate distribution, Couette inverse problem and velocity profiling, we employed velocity profiling to utilize its advantages. For example, it is enabled to confirm whether the flow is really one dimensional, steady and non-slip. Furthermore, the velocity profiling gives an extensibility to viscoelasticity measurement by measuring unsteady flows. Previous researches have introduced rheological model to avoid noise enhancement in derivative calculation. In the rheological model-based approximations, however, the choice of the model crucially affects the flow curve derivation. If the power law model is used to obtain the flow curve of an unknown fluid material, with certain yield stress, the derived flow curve actually overlooks the yield stress. Consequently the model-dependent velocity profile approximation claims preliminary knowledge about the rheological characteristics prior to the experiment. This restricts the applicability of velocity profiling-base rheometry in engineering, which often deals with unknown materials.

We therefore aim here to establish a model-free rheometry that does not require any rheological models. We use a configuration of concentric cylinders with a large gap, making the method applicable to fluids with time-dependent properties, large components, or non-uniform shear rates. The shear rate varies across the test fluid even if the fluid is subjected to the constant rotational speed of the cylinder. The measurement of the velocity distribution between the cylinders leads to the acquisition of the flow curve without having to vary the rotational speed of the cylinder. The time required to obtain the complete flow curve is therefore greatly reduced. UVP was

chosen as the velocimetry because of its instantaneous velocity profiling and applicability to opaque fluids. We have previously used UVP for non-Newtonian and opaque fluids and presented a series of flow visualizations [26]. In this current work, the velocity distribution was approximated with power series polynomials and Chebyshev expansions, instead of functions derived *a priori* from rheological models. The power series is widely used for function approximation as the simplest polynomials [27]. Chebyshev expansions give the best approximation of  $(m-1)$ th order polynomials for  $m$ th order power series polynomials [28]. In a concentric cylinder system with a wide gap, a large fluid velocity gradient appears near the inner cylinder, particularly in shear-thinning fluids. We propose a transformation of variable in flow curve derivation that resolves this region of large velocity gradient. We use silicone oil, polyacrylamide (PAA) solution, and yogurt as test fluids, which are examples of Newtonian fluids, shear-thinning fluids, and opaque fluids, respectively. Flow curves for the silicone oil and PAA solution are compared with the data collected by a conventional commercial rheometer. We analyze yogurt to demonstrate the applicability of our technique to a quality-changeable soft matter.

**Table 3.1** Comparison of our model-free rheometry with other rheometry techniques that use velocity profile information

Author	Year	Geometry	Velocimetry	Rheological model	Advantage	Disadvantage
Ouriev [14]	2002	Pipe	UVP	Power law	In-line	Model dependent
Wiklund [17]	2006	Pipe	UVP, LDV	Herschel-Bulkley	In-line	Model dependent
Derakhshandeh [21]	2012	Concentric cylinder	UVP	Herschel-Bulkley	High accuracy	Model dependent
Perez-Gonzalez [25]	2012	Pipe	PIV	None	In-line, model independent	Transparent fluid only
Gallot [22]	2013	Concentric cylinder	UVP	None	Model independent	Qualitative characterization
Present research	2014	Concentric cylinder	UVP	None	Model independent	Off-line

## 3.2 Experimental setup

### 3.2.1 Experimental apparatus

The experimental apparatus is shown in Fig. 3.1. Flow between concentric cylinders was used as a basic flow configuration, but the gap between the cylinders is much wider than in conventional rheometers. Radii of the inner cylinder,  $r_{in}$ , and outer cylinder,  $r_{out}$ , are 15.0 mm and 71.5 mm, respectively, and the corresponding gap size is 46.5 mm. These dimensions were determined by considering the measurement requirements of UVP and the test fluid was introduced into the gap: Because the spatial resolution of UVP on the measurement line is 0.38 mm, the gap is resolved into more than hundreds data points which is enough to derive shear rate profile by differential calculations. There is no lid, so the top side of the fluid is a free surface. As the inner cylinder rotates, a shear flow is driven between the gap. In this study, only one assumption was applied; we presumed a one-directional flow in the circumferential direction. Specifically, the radial and axial velocity components are regarded as zero so that physical properties are unvaried in the azimuthal and axial directions. The inner cylinder was connected to a motor with a torque sensor (Bohlin Visco88; Malvern Instruments Ltd., Malvern, U.K.) that both rotated the cylinder and enabled time variations of the torque to be recorded. The measured torque,  $T$ , gives the shear stress on the wall of the inner cylinder,  $\tau_{wall}$ , by

$$\tau_{wall} = -\frac{T}{2\pi r_{in}^2 H}, \quad (3.1)$$

where  $H = 50$  mm is the height of the inner cylinder. The negative sign in the equation indicates that the shear rate component,  $\dot{\gamma}_{r,\theta}$ , defined by the radial derivative of fluid velocity is always negative in the flow. An ultrasonic transducer was installed at the side wall of the outer cylinder as shown in Fig. 3.1 (a). The propagation line of the ultrasonic wave corresponding to the measurement line of UVP was arranged separate from the wall of the inner cylinder to prevent reflection of ultrasonic waves on the wall. The height of the transducer was located 25 mm from the bottom of the cylinder, which corresponds to the middle of the fluid layer. Data acquisition of the torque sensor and UVP was started simultaneously. By using the definition of cylindrical coordinates, the origin point of the  $r$  axis was set at the center of the inner cylinder, meaning that the wall of the inner cylinder is located at  $r = 15$  mm. To obtain the viscosity of the test fluid, a radial distribution of the circumferential velocity component,  $u_\theta(r)$ , was required. UVP-DUO (Metflow S.A., Lausanne, Switzerland) was introduced to measure instantaneous profiles of velocity component projected in the measurement line,  $u_x$ , as shown in Fig. 3.1 (a). For one-directional flows,  $u_x$  is converted to  $u_\theta$  as

$$u_{\theta} = \frac{u_x}{\cos \alpha}, \quad (3.2)$$

where  $\alpha$  is the angular coordinate of the measurement point against the center of the cylinder, as shown in Fig. 3.1 (a). In cases where the test fluid has both shear-rate-dependent viscosity and viscoelasticity, the flow immediately after the start of inner cylinder rotation is governed by viscoelasticity, and then converges to a steady state that is governed by shear-rate-dependent viscosity. In this analysis, therefore, the spatial distribution of  $u_{\theta}$  under the steady state was used as a time average of  $u_{\theta}$ , to derive the shear-rate-dependent viscosity of the test fluid. The viscoelasticity measurement requires time-dependent velocity profile information, but we consider this as a separate issue from the work presented here because further assessment of the temporal resolution of UVP is needed. Reaching the steady flow state was judged from the time variation of the torque. The measurement was performed at room temperature.

The test fluids were 1000 cSt silicone oil (KF96-1000cs; Shin-Etsu Chemical Co., Ltd., Tokyo, Japan), 1.0 wt% PAA solution (AP805C; Dia-Nitrix Co., Ltd., Tokyo, Japan), and yogurt (LB81 plain; Meiji Co., Ltd., Tokyo, Japan). The silicone oil is a Newtonian fluid with a constant viscosity of 0.97 Pa·s. PAA solution is a fluid with a shear-rate-dependent viscosity. The yogurt is an example of an opaque viscoelastic fluid whose properties easily fluctuate in time and space. In the silicone oil and the PAA solution, resin powders, FLO-BEADS CL-2507 (Sumitomo Seika Chemicals), and DIAION HP20SS (Mitsubishi Chemical) were dispersed, respectively, as tracer particles. In cases of both of fluids, the amount of tracer particle is around 0.005 wt% which is enough to visualize the flow and reflect ultrasonic beam. The effect of the tracer particles to viscosity of fluids is estimated as 0.013 % [29], which is negligibly small compared to measurement accuracy of the present characterization. In the yogurt, the fat content reflects ultrasonic waves [19], so tracer particles were not needed. The velocity of the inner cylinder wall,  $U_{wall}$ , was fixed at 31.1 mm/s for the silicone oil and the PAA solution. This rotational velocity is large enough to drive the fluids on the ultrasonic measurement line, and small enough to prevent the Weissenberg effect of the PAA solution, whereby fluids rise up along the inner cylinder. For yogurt this same velocity is not enough to drive the fluid, because it has a yield stress (or its equivalent stress) at which the solid-like state alters to a fluidized state. Thus, a larger  $U_{wall}$  of 96.1 mm/s was chosen to give a higher shear stress than the yield stress. Resolutions and measurable ranges of UVP for each test fluids are summarized in Table 3.2. In measurements with silicone oil and PAA solution, maximum value of measurable velocity  $u_{x,max}$  is set larger than  $U_{wall}$  with a view to analyze unsteady velocity profiles

obtained by UVP in the future: In unsteady state, velocity of viscoelastic fluid on the measurement line can reach almost  $U_{wall}$  while the fluid velocity on the measurement line is much smaller than  $U_{wall}$  in steady state. In the measurement with yogurt,  $u_{x,max}$  is set smaller than  $U_{wall}$  to resolve small velocity of the yogurt on the measurement line. Figure 3.2 shows the reference values of the shear-rate-dependent viscosity of the PAA solution, measured with a commercial cone-plate rheometer (Bohlin CVO; Malvern Instruments Ltd., Malvern, U.K.). Circle symbols in the figure indicate the measured shear stress,  $\tau$ , at the shear rate,  $\dot{\gamma}$ . The relationship matches a power law described by

$$\tau = k\dot{\gamma}^n, \quad (3.3)$$

where  $n$  and  $k$  are constants representing the properties of the fluid and were determined to be  $n = 0.25$  and  $k = 5.86 \text{ Pa}\cdot\text{s}^n$ , by least-square approximation. The value of  $n$  smaller than unity means that the PAA solution is a shear thinning fluid.

Velocity and shear rate distribution in steady states are analytically predictable from Eq. (3.3) and the following equation of motion of fluid in the circumferential direction,

$$\rho \frac{\partial u_\theta}{\partial t} = \frac{2\tau}{r} + \frac{\partial \tau}{\partial r}, \quad (3.4)$$

under the assumption of one-directional flow. In the steady state, Eq. (3.4) yields

$$\frac{2\tau}{r} + \frac{d\tau}{dr} = 0. \quad (3.5)$$

The radial distribution of the shear stress  $\tau$  is derived from Eq. (3.5) as

$$\tau = \tau_{wall} \left( \frac{r_{in}}{r} \right)^2. \quad (3.6)$$

In cylindrical coordinates, the relation between shear rate and velocity distribution is described as

$$\dot{\gamma} = \frac{du_\theta}{dr} - \frac{u_\theta}{r}. \quad (3.7)$$

Velocity and shear rate distributions between concentric cylinders are obtained by Eqs. (3.8) and (3.9), respectively, by solving Eqs. (3.3), (3.6), and (3.7), with non-slip boundary conditions ( $u_\theta = U_{wall}$  at  $r = r_{in}$  and  $u_\theta = 0$  at  $r = r_{out}$ ), as

$$u_\theta = \frac{r_{in}^{2/n}}{1 - (r_{in}/r_{out})^{2/n}} \left( r^{1-2/n} - r_{out}^{-2/n} r \right) \frac{U_{wall}}{r_{in}}, \quad (3.8)$$

$$\dot{\gamma} = -\frac{2}{n} \frac{1}{1 - (r_{in}/r_{out})^{2/n}} \left( \frac{r_{in}}{r} \right)^n \frac{U_{wall}}{r_{in}}, \quad (3.9)$$

where  $U_{wall}$  is the velocity of the inner cylinder wall. The spatial distribution of the shear rate described in Eq. (3.9) allows us to obtain a flow curve with Eq. (3.6) within a given range of shear rate. According to Eq. (3.9), maximum shear rate  $\dot{\gamma}_{max}$  and minimum shear rate  $\dot{\gamma}_{min}$ , which are realized at  $r = r_{in}$  and  $r = r_{out}$ , respectively, are described as

$$\dot{\gamma}_{max} = -\frac{2}{n} \frac{1}{1 - (r_{in}/r_{out})^{2/n}} \frac{U_{wall}}{r_{in}}, \quad (3.10)$$

$$\dot{\gamma}_{min} = -\frac{2}{n} \frac{1}{1 - (r_{in}/r_{out})^{2/n}} \left( \frac{r_{in}}{r_{out}} \right)^n \frac{U_{wall}}{r_{in}}. \quad (3.11)$$

Thus the ratio of  $\dot{\gamma}_{max}$  to  $\dot{\gamma}_{min}$  is determined by the radius ratio and power law index, namely

$$\frac{\dot{\gamma}_{max}}{\dot{\gamma}_{min}} = \left( \frac{r_{out}}{r_{in}} \right)^n. \quad (3.12)$$

In case that the PAA solution ( $n = 0.25$ ) is measured by the apparatus shown in Fig. 3.1, the ratio  $\dot{\gamma}_{max}/\dot{\gamma}_{min}$  equals  $2.24 \times 10^5$ . It means that flow curve is obtained under five decades of shear rate without varying rotational velocity of the inner cylinder if the velocity distribution between the cylinders was perfectly obtained. In Newtonian case, on the other hand, flow curve is obtained only under one decade of shear rate because the ratio  $\dot{\gamma}_{max}/\dot{\gamma}_{min}$  equals 22.7.

### 3.2.2 Error propagation and measurement limitation

Error propagation in this measurement configuration is theoretically assessed below. When a quantity  $y$  is derived from experimentally measured quantities  $x_l$  as

$$y = f(x_1, x_2, x_3, \dots, x_l, \dots, x_M), \quad (3.13)$$

measurement error on  $y$ ,  $\delta y$ , is described as following

$$\delta y = \pm \sqrt{\sum_{l=1}^M \left( \frac{\partial f}{\partial x_l} \delta x_l \right)^2}, \quad (3.14)$$

where  $\delta x_l$  are errors on the measured quantities  $x_l$ . Geometrical conditions in Fig. 3.1 is described as the following equations

$$\cos \alpha = \frac{d}{r} \quad (3.15)$$

$$r = \sqrt{r_{out}^2 - 2x\xi + x^2} \quad (3.16)$$

$$\xi = \sqrt{r_{out}^2 - d^2} \quad (3.17)$$

where  $d$  means distance between the center line of the cylinder and the measurement line (20 mm in Fig. 3.1 (a)). According to Eqs. (3.2), (3.15) and (3.16),  $u_\theta$  is described as a function of  $u_x$  and dimensions of the experimental apparatus, namely

$$u_\theta = \frac{u_x}{d} \sqrt{r_{out}^2 - 2x\xi + x^2}. \quad (3.18)$$

In the quantities in Eq. (3.18),  $u_x$  and  $d$  are regarded as quantities which include errors. Errors on  $u_x$  correspond to measurement errors of UVP. The distance  $d$  is suspected to include error because the position of the transducer is manually fixed. Therefore, Eqs. (3.14) and (3.18) give equations to derive the error on  $u_\theta$  as

$$\delta u_\theta = \pm \sqrt{\left( \frac{\partial u_\theta}{\partial d} \delta d \right)^2 + \left( \frac{\partial u_\theta}{\partial u_x} \delta u_x \right)^2}, \quad (3.19)$$

$$\frac{\partial u_\theta}{\partial d} = \frac{u_x}{d^2} \sqrt{r_{out}^2 - 2x\xi + x^2} + \frac{xu_x}{\xi \sqrt{r_{out}^2 - 2x\xi + x^2}}, \quad (3.20)$$

$$\frac{\partial u_\theta}{\partial u_x} = \frac{1}{d} \sqrt{r_{out}^2 - 2x\xi + x^2}. \quad (3.21)$$

To obtain a flow curve from a velocity profile, spatial distribution of shear rate have to be derived from the velocity profile. The simplest way to derive the shear rate is to calculate the velocity gradient with finite differencing. Then shear rate is described in discretized form as

$$\dot{\gamma}_{i,j} = \frac{u_{i+1,j} - u_{i-1,j}}{2\Delta r} - \frac{u_{i,j}}{r_i}, \quad (3.22)$$

where  $\Delta r$  is spatial resolution on  $r$  axis, the suffixes  $i$  and  $j$  indicate the position and time in discretized form. In Eq. (3.22),  $u_{i,j}$  and  $r_i$  are regarded as causes of errors. Thus the error on shear rate,  $\delta \dot{\gamma}$ , is described as

$$\delta \dot{\gamma}_{i,j} = \pm \sqrt{\left[ \frac{1}{(\Delta r)^2} + \frac{1}{r_i^2} \right] (\delta u_\theta)^2 + \left( \frac{u_{i,j}}{r_i^2} \delta r \right)^2}. \quad (3.23)$$

Note that  $\Delta r$  and  $\delta r$  in Eq. (3.23) are described as functions of  $d$  and  $x$ , namely

$$\Delta r = \frac{\xi - x}{\sqrt{d^2 + (\xi - x)^2}} \Delta x, \quad (3.24)$$

$$\delta r = \frac{x}{4\xi\sqrt{d^2 + (\xi - x)^2}} \delta d, \quad (3.25)$$

where  $\Delta x$  means spatial resolution of UVP. The measurement errors on velocity and shear rate, described by Eqs. (3.19) and (3.25), respectively, are shown in the next Section together with experimental velocity profiles.

To confirm that the flow is one dimensional, which is assumption of Eq. (3.2), Reynolds number  $Re$  should be less than critical Reynolds number  $Re_c$ . In flows between concentric cylinders,  $Re$  is defined as

$$Re = \frac{\rho U_{wall}(r_{out} - r_{in})}{\eta}, \quad (3.26)$$

where  $\eta$  means viscosity of the fluid. Because viscosity of non-Newtonian fluids varies depending on shear rate, characteristic viscosity have to be defined to substitute  $\eta$ . Here, power law, described by Eq. (3.3), is introduced to give viscosity. Then  $Re$  is described as

$$Re = \frac{\rho U_{wall}(r_{out} - r_{in})}{k\dot{\gamma}_c^{n-1}}, \quad (3.27)$$

$$\dot{\gamma}_c = \frac{U_{wall}}{r_{out} - r_{in}}. \quad (3.28)$$

In this experiment,  $Re$  defined by Eq. (3.27) is 5.43 even in the largest case ( $U_{wall} = 96.1$  for silicone oil). According to a previous research [30],  $Re_c$  under the present radius ratio,  $r_{in}/r_{out} = 0.21$ , is estimated at about 100. Thus the flow is kept laminar during the experiment.

In measurements of flow curve with conventional rheometers, shear stress is measured in a wide range of shear rate, over some decades, while changing rotational velocity. In the present rheometry, measurable range of shear rate is determined by geometry and measurement condition of UVP. Here, maximum shear rate measured in the present configuration is theoretically estimated. Figure 3.3 shows geometry of measurement points near the inner cylinder. It is expected that the maximum shear rate  $\dot{\gamma}_{max}$  is obtained at the nearest measurement point to the inner cylinder, namely

$$\dot{\gamma}_{max} = \frac{u_{\theta,r=d+\Delta r_{min}} - u_{\theta,r=d}}{\Delta r_{min}} - \frac{u_{\theta,r=d}}{d}, \quad (3.29)$$

where  $\Delta r_{min}$  means difference of radial position between points A and B in Fig. 3.3.

When measured velocity profile is converted to radial distribution, radial position of points A and B are described as  $d$  and  $d + \Delta r_{min}$ , respectively. From the geometrical relation, the radial distance between the points  $\Delta r_{min}$  is described as

$$\Delta r_{min} = \sqrt{d^2 + \Delta x^2} - d. \quad (3.30)$$

The difference of  $u_x$  between points A and B equals velocity resolution of UVP  $\Delta u_x$  because  $\Delta r_{min}$  is too small to make larger velocity difference than  $2\Delta u_x$  between the points. Thus  $u_{\theta, r=d+\Delta r_{min}}$  in Eq. (3.29) is described as

$$u_{\theta, r=d+\Delta r_{min}} = \frac{\sqrt{d^2 + \Delta x^2}}{d} [u_{\theta, r=d} - \Delta u_x]. \quad (3.31)$$

From Eqs. (3.29), (3.30) and (3.31),  $\dot{\gamma}_{max}$  is described as

$$\dot{\gamma}_{max} = \frac{(\sqrt{d^2 + \Delta x^2} / d - 1) u_{\theta, r=d} - \Delta u_x \sqrt{d^2 + \Delta x^2} / d}{\sqrt{d^2 + \Delta x^2} - d} - \frac{u_{\theta, r=d}}{d}. \quad (3.32)$$

By substituting  $u_{\theta, r=d}$  from Eq. (3.8), measurable maximum shear rate is estimated. According to Eq. (3.32), the apparatus shown in Fig. 3.1 can measure shear rate up to 76 and 102  $s^{-1}$  for the silicone oil and the PAA solution, respectively.

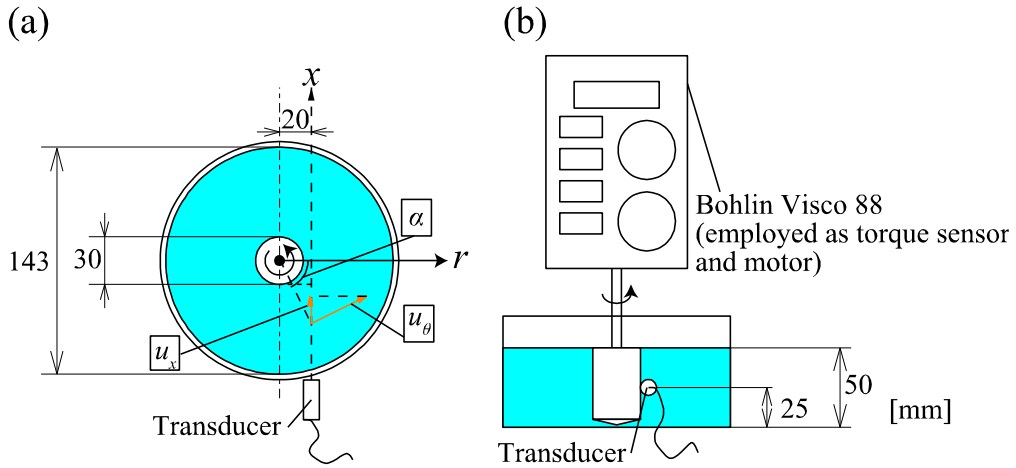


**Figure 3.1** (a) Top view and (b) side view of the experimental apparatus

**Table 3.2** Measurement condition of UVP for each test fluids

Test fluid	Wall velocity $U_{wall}$ [mm/s]	Time resolution $\Delta t$ [s]	Spatial resolution $\Delta x$ [mm]	Velocity resolution $\Delta u_x$ [mm/s]	Maximum velocity $u_{x,max}$ [mm/s]
Silicone oil	31.1	0.121	0.37	0.25	32
PAA solution	31.1	0.132	0.38	0.36	46.08
Yogurt	96.1	0.132	0.39	0.37	47.36

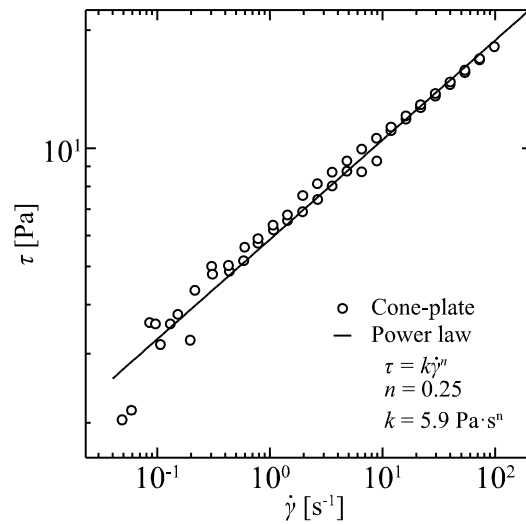


**Figure 3.2** Flow curve of 1.0 wt% polyacrylamide solution obtained with a commercial cone-plate rheometer (circles) and approximation curve derived from the power law (line)

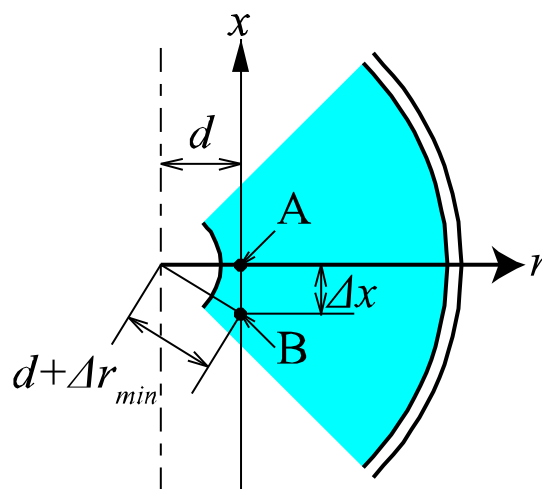


**Figure 3.3** Geometry of data points near the inner cylinder to estimate maximum limit of shear rate measurement

### 3.3 Flow curve derivation with finite differential method

The simplest way to derive the shear rate from the velocity profile is to use Eq. (3.22), which corresponds to calculate the velocity gradient with finite differencing. Figure 3.4 (a), Fig. 3.5 (a) and Fig. 3.6 (a) indicate the spatial distributions of the azimuthal velocity component,  $u_\theta$ , and Fig. 3.4 (b), Fig. 3.5 (b) and Fig. 3.6 (b) indicate shear rate,  $\dot{\gamma}$ , calculated from the distribution of  $u_\theta$  with Eq. (3.22), for three test fluids. Light blue circles indicate the velocity and shear rate obtained from the experiment. The velocity profiles in (a) of Figs. 3.4-3.6 are normalized by the velocity of the inner cylinder wall  $U_{wall}$ . In (b) of Figs. 3.4-3.6, the shear rate is normalized by the characteristic shear rate,  $\dot{\gamma}_c$ , which is defined as

$$\dot{\gamma}_c = -\frac{U_{wall}}{r_{out} - r_{in}}. \quad (3.33)$$

The horizontal axes of (a) and (b) of Figs. 3.3-3.5 indicate normalized radial position, defined as

$$r^* = \frac{r - r_{in}}{r_{out} - r_{in}}. \quad (3.34)$$

As seen in the velocity profiles, there are some dips, for example around  $r^* = 0.15$  in Fig. 3.4 (a), even though Eq. (3.8) indicates that  $u_\theta(r)$  is expected to be a monotonically decreasing function. There were unexpected reflections of ultrasonic waves from the side wall, and so we eliminated the corresponding data points by evaluating the ultrasonic echo signals. Black open circular symbols in Fig. 3.4 represent data points after the elimination, and it can be seen that the dips were successfully removed. Theoretical velocity distribution and expected error, described by Eqs. (3.8) and (3.19), respectively, are indicated in (a) of Figs. 3.4 and 3.5. The error on the position of the transducer,  $\delta d$  in Eq. (3.19), is assumed to be 0.5 mm, which is a half value of minimum scale of the ruler to fix the position. The error on the velocity  $\delta u_x$  is equal to velocity resolution of UVP  $\Delta u_x$ , 0.25 mm/s for silicone oil and 0.36 mm/s for PAA solution. In Fig. 3.4 (a), the experimental velocity profile of the silicone oil deviates from the theoretical distribution. This deviation implies that the position of the transducer is deviated more than the expectation, or velocity includes larger errors than  $\Delta u_x$ . The experimental velocity profile of the PAA solution, indicated in Fig. 3.5 (a), follow the theoretical velocity profile well. Although the experimental velocity slightly deviates from the theoretical one, the difference between them is in the range of error expected by Eq. (3.19).

Shear rate distributions of the three test fluids were obtained from the velocity distributions with a finite differencing of Eq. (3.22), for calculating the velocity gradient.

The shear rate distributions of silicone oil, PAA solution, and yogurt are shown as (b) of Fig. 3.4, 3.5 and 3.6. Because the finite differencing enhances measurement errors in the velocity profiles, the measured shear rate has a larger deviation than the theoretical value, especially near the inner cylinder. In the case of silicone oil, the maximum normalized shear rate is expected to be 4.5 in the measured spatial range, but the measured value jumps up to 20, as shown in Fig. 3.4 (d). Theoretical distribution and expected errors of shear rate, described by Eqs. (3.9) and (3.23), respectively, are displayed together with the experimental distribution. In both cases of fluids,  $\delta\dot{\gamma}$  is large near the inner cylinder. This is because  $\Delta r$  is small near the inner cylinder according to Eq. (3.24), and thus the term  $1/(\Delta r)^2$  contributes to increase  $\delta\dot{\gamma}$ . The term  $(u_{\theta}\delta r/r^2)^2$  in Eq. (3.23) means that large velocity near the inner cylinder also contributes to increase  $\delta\dot{\gamma}$  there. The deviation of experimental shear rate from theoretical one is explained by the enhancement of  $\delta u_{\theta}$  and  $\delta r$  in the finite differential calculation as (b) of Figs. 3.4 and 3.5 shows.

Such error enhancement will affect the fluid characterization and needs to be removed. Flow curves for the three fluids are depicted in (c) and (d) of Fig. 3.4, 3.5 and 3.6. In the derivation of these flow curves, shear rate is calculated by a finite differential of Eq. (3.22) at the given shear stress calculated from Eqs. (3.1) and (3.6). The shear rate derived by finite differential varies widely as shown in (b) of Figs. 3.4-3.6. Also on flow curve, of course, shear rate varies widely. Thus (c) of Figs. 3.4-3.6 shows all of the derived data points on flow curve, and (d) of Figs. 3.4-3.6 focuses on shear rate range where realistically occurs between the cylinders. In Figs. 3.4 and 3.5, flow curves obtained in different conditions of  $U_{wall}$  are indicated. In Fig. 3.6, only the flow curve obtained under the condition of  $U_{wall} = 96.1$  mm/s is shown because the effect from degradation of the yogurt has higher impact on flow curve than that from the variation of  $U_{wall}$ . The silicone oil is a Newtonian fluid and should have a linear flow curve. In Fig. 3.4 (d), flow curves derived from velocity profiles, indicated by circles, describes the linear relation well while shear rate and shear stress are low. In the case of  $U_{wall} = 96.1$  mm/s, for example, the derived flow curve agrees the linear relation in  $\tau < 6.0$  Pa, but deviates in higher stress region. The higher shear stress region corresponds to the region near the inner cylinder in space. Thus reflection of ultrasound on the inner cylinder cause measurement error, and this yield the deviation of derived flow curve from the linear relation. The deviation occurs in different shear stress range depending on  $U_{wall}$ . This is because higher shear stress is applied near the inner cylinder when  $U_{wall}$  is larger. In Fig. 3.5 (d), which shows flow curves of the PAA solution, the flow curves derived from the velocity profiles, indicated by blue, green and red circles, have same

trend as that obtained with a conventional cone-plate rheometer shown by black circles. But as is the case in the silicone oil, the flow curves from velocity profiles deviate from the reference value obtained with a conventional rheometer under high shear stress. The flow curve of yogurt derived from velocity profile, indicated by black circles in Fig. 3.6 (d), is similar to that of yield stress fluids: Shear rate is almost zero under the yield stress  $\tau_y$ , and the curve is upward slope in  $\tau > \tau_y$ . The existence of yield stress accords with the nature of the yogurt that it suddenly transit from solid to liquid state when stress is applied. The yield stress is estimated to be around 10 Pa from the flow curve derived from the velocity profile.

As mentioned earlier, the shear-thinning behavior of the PAA solution is well described by a power law, as in Eq. (3.3). It is also applicable to Newtonian fluids with  $n = 1$ . We therefore applied it to the silicone oil, PAA solution and yogurt to fit the flow curves. Based on the least square approximation in double logarithmic plot, the power law coefficient,  $k$ , and power law index,  $n$ , are expressed as

$$\log k = \frac{\sum_{j=1}^N (\log \tau_j)^2 \sum_{j=1}^N \log \dot{\gamma}_j - \sum_{j=1}^N (\log \tau_j \log \dot{\gamma}_j) \sum_{j=1}^N \log \tau_j}{\sum_{j=1}^N \log \tau_j \sum_{j=1}^N \log \dot{\gamma}_j - N \sum_{j=1}^N (\log \tau_j \log \dot{\gamma}_j)} \quad (3.35)$$

$$n = \frac{N \sum_{j=1}^N (\log \tau_j)^2 - \left( \sum_{j=1}^N \log \tau_j \right)^2}{N \sum_{j=1}^N (\log \tau_j \log \dot{\gamma}_j) - \sum_{j=1}^N \log \tau_j \sum_{j=1}^N \log \dot{\gamma}_j} \quad (3.36)$$

where  $N$  is the number of the data points obtained experimentally. To the flow curve of the silicone oil, approximation with Newton's law of viscosity,

$$\tau = \eta \dot{\gamma} \quad (3.37)$$

was also performed. The Newtonian viscosity  $\eta$  is derived from the discrete flow curve by

$$\eta = \frac{\sum_{j=1}^N \tau_j \dot{\gamma}_j}{\sum_{j=1}^N \tau_j^2} \quad (3.38)$$

based on the least square approximation in linear plot. The ultrasonic rheometry presented here has a larger uncertainty in the shear rate than in the shear stress, and thus the square of the error of the shear rate is minimized to approximate flow curves with

the power law and Newton's law of viscosity. In Fig. 3.4 (d) and 3.5 (d), flow curves obtained in  $U_{wall} = 31.1$  mm/s are chosen as the object of approximation because the assumption of one-dimensional flow is satisfied well. The flow curve obtained by Eq. (3.38) is indicated by blue dashed line in Fig. 3.4 (d), and solid lines in (d) of Figs. 3.4-3.6 indicate flow curves obtained by Eqs. (3.35) and (3.36). As seen in the figures, the approximations with Newton's law of viscosity and power law are strongly affected by the error enhanced by the finite differential calculation for the shear rate. In the case of silicone oil, the power law index,  $n$ , is determined to be  $n = 0.49$ . This should be around unity, because the silicone oil is regarded as a Newtonian fluid. High shear rate values are obtained at around  $\tau = 2.0$  Pa, which exists close to the inner cylinder. By introducing Newton's law of viscosity, the approximation gives better flow curve. In Fig. 3.4 (d), the flow curve obtained with the Newton's law less deviates from the theoretical curve while that obtained with the power law largely deviates. Viscosity  $\eta$  was detected as 0.69 Pa·s with Eq. (3.38). This is about 30% lower than the reference value, 0.97 Pa·s. It is difficult to quantify viscosity precisely even if the proper rheological model is introduced to the approximation. In the flow curve of the PAA solution, shown in Fig. 3.5 (d), the approximation curve of the power law underestimates the shear rate in the high shear stress region when compared with the commercial cone-plate rheometer (black symbols).

Median filter is performed for the flow curves shown in (d) of Figs. 3.4, 3.5 and 3.6 to reduce errors amplified in the finite differential. Here two kinds of median filter are performed. In the first case, shown in (b) of Figs. 3.7, 3.8 and 3.9, data points are compared to other two data points neighboring in shear stress, and a median value of shear rate is employed to the data point. In the second case, three data points neighboring in shear rate are compared, and median value of shear stress is employed. The result of the second median filter is shown in (c) of Figs. 3.7, 3.8 and 3.9. Figure 3.7 (a), (b) and (c) indicate flow curves before the median filter, and after the two kinds of median filters. Because shear rate in Fig. 3.4 (b) fluctuate near the inner cylinder, the flow curve in Fig. 3.7 (a) has two values of shear stress for one shear rate. Two data points indicated by a green circle in Fig. 3.7 (a), for example, have high shear stress (about  $\tau = 2.6$  Pa) while many data points in the same shear rate range have low shear stress (about  $1.1 < \tau < 1.6$  Pa). The two data points are removed in Fig. 3.7 (c) because they are compared with data points of low shear stress. In Fig. 3.7 (b), on the other hand, the two data points remain because they are compared with data points neighboring in shear stress. In cases that the test fluid is Newtonian fluid, the difference between the two kinds of median filters is not a problem because the flow curve is described as a

single value function. In cases that the test fluid is non-Newtonian fluid, on the other hand, the choice of quantity to perform median filter can significantly affect the result because shear stress of some non-Newtonian fluids is described as multiple-valued function of shear rate, or inversely, shear rate is described as multiple-valued function of shear stress. The two kinds of median filter does not make significant difference in Fig. 3.8. In Fig. 3.9, which shows a flow curve of yogurt, the two median filters make difference at around  $\dot{\gamma} = 0$ . Many data points of different shear stress exists at around  $\dot{\gamma} = 0$  because the yogurt does not flow under a certain shear stress, and thus some data points are modified there in Fig. 3.9 (c).

To avoid the error amplification in finite differential calculations, other velocity profile-based rheometry use fitting of the experimental velocity distribution by the power law as a rheological model for shear-rate-dependent viscosity [4-6,9]. The power law is introduced here to our rheometry, and the differential is obtained analytically by approximating the velocity profile with Eq. (3.8). In the fitting, the index,  $n$ , is determined by the least-square approximation by varying  $n$  from 0.02 to 1.00 (with an increment of  $10^{-3}$ ) for all test fluids. The coefficient,  $k$ , is determined from both  $n$  and the shear stress on the inner cylinder wall,  $\tau_w$ , by combining Eqs. (3.3) and (3.9) as

$$k = \tau_{wall} \left\{ \frac{2U_{wall}}{\left[1 - (r_{in}/r_{out})^{2/n}\right]nr_{in}} \right\}^{-n}. \quad (3.39)$$

The results of the fitting are shown in Fig. 3.10 (a)–(c) as solid lines on the experimental data. Corresponding flow curves are also shown in Fig. 3.10 (d)–(f). In the silicone oil and PAA solution (Fig. 3.10 (a) and (b)), there are remarkable differences between the experimental data and the approximation curves. In contrast, the corresponding flow curves calculated from these velocity profiles, Fig. 3.10 (d) and (e), represent the rheological characteristics of the fluids well. The index,  $n$ , for the silicone oil is 0.82 and is much closer to unity than the  $n = 0.49$  shown in Fig. 3.4 (d). The flow curve for the PAA solution closely matches the reference value obtained by a cone-plate rheometer, displayed by red symbols. The measured index  $n = 0.26$  agrees well with the reference value shown in Fig. 3.2. These two fluids originally obey the power law, demonstrating that these results are reasonable. In the case of the yogurt, the power law seems to represent the velocity profile well, as shown in Fig. 3.10 (c). In the flow curve shown in Fig. 3.10 (f), however, the estimated flow curve shows large differences from the experimental data and does not represent the rheological characteristics of the yogurt. The experimental data seems to be divided into two regions around 10 Pa. It suggests the existence of yield stress around 10 Pa, below which the fluid materials remain

immobile. Such a fluid having a yield stress is out of the applicable range of the power law. This result confirms that adopting the power law cannot be a universal step in the present velocimetry-based rheometry, even for steady shear rate conditions. Similar problems arise for other general fluid materials when invalid rheological models are used, which results in bad approximations of flow curve. We therefore need to establish general model-free characterizations of the rheological properties for all materials.

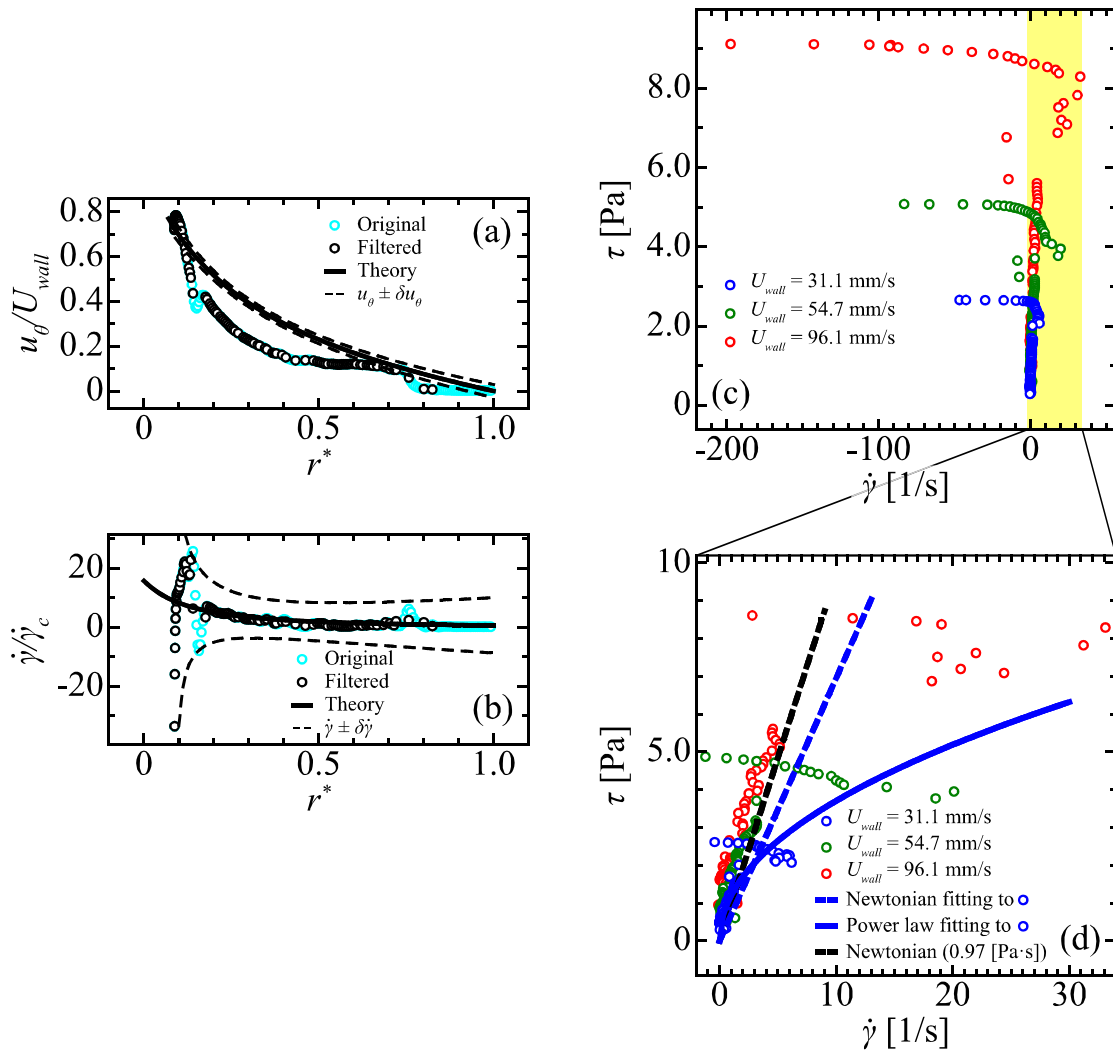


**Figure 3.4** Spatial distributions of (a) velocity, (b) shear rate, and (c) (d) flow curve of silicone oil obtained with finite differential

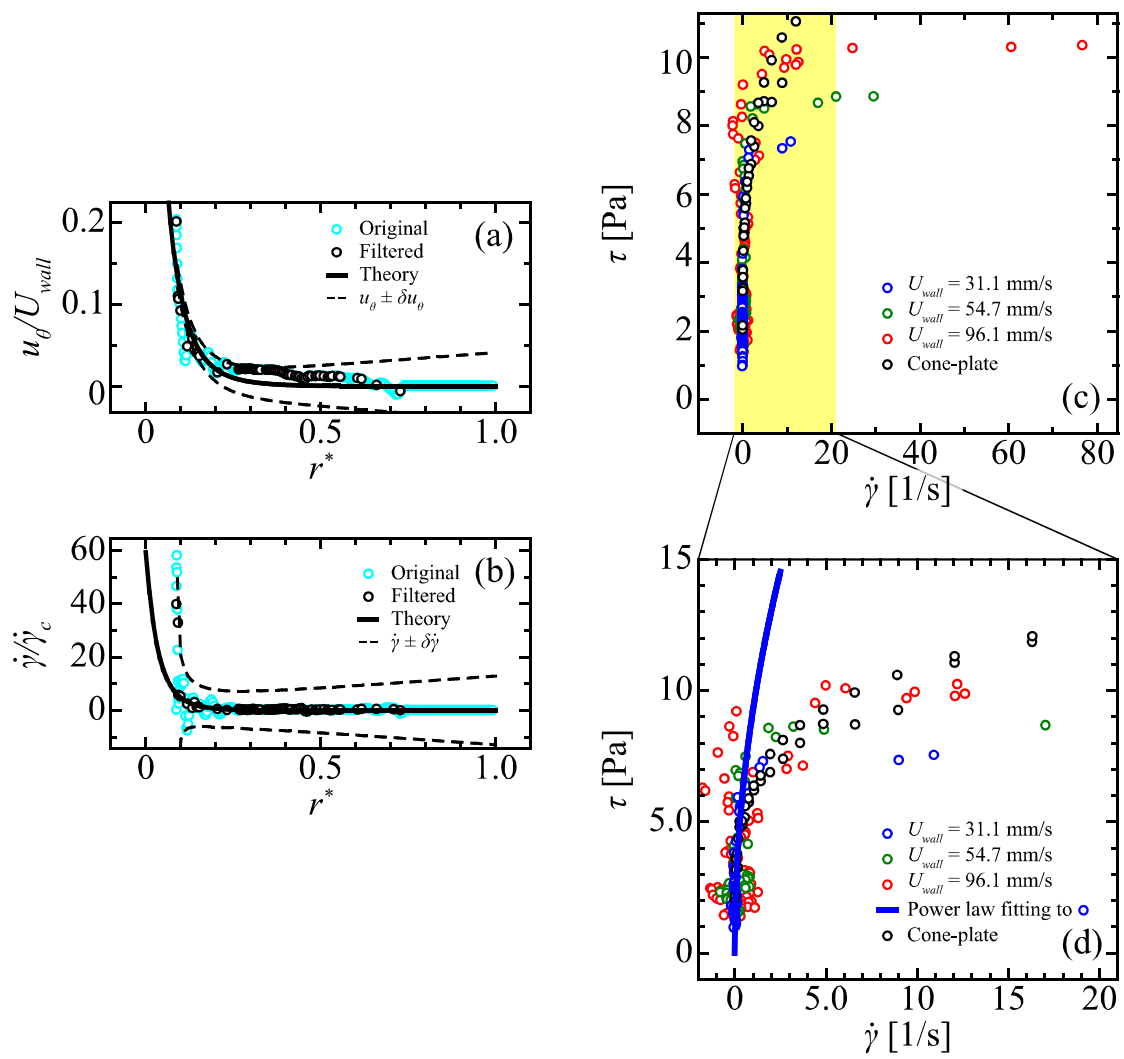


**Figure 3.5** Spatial distributions of (a) velocity, (b) shear rate, and (c) (d) flow curve of PAA solution obtained with finite differential

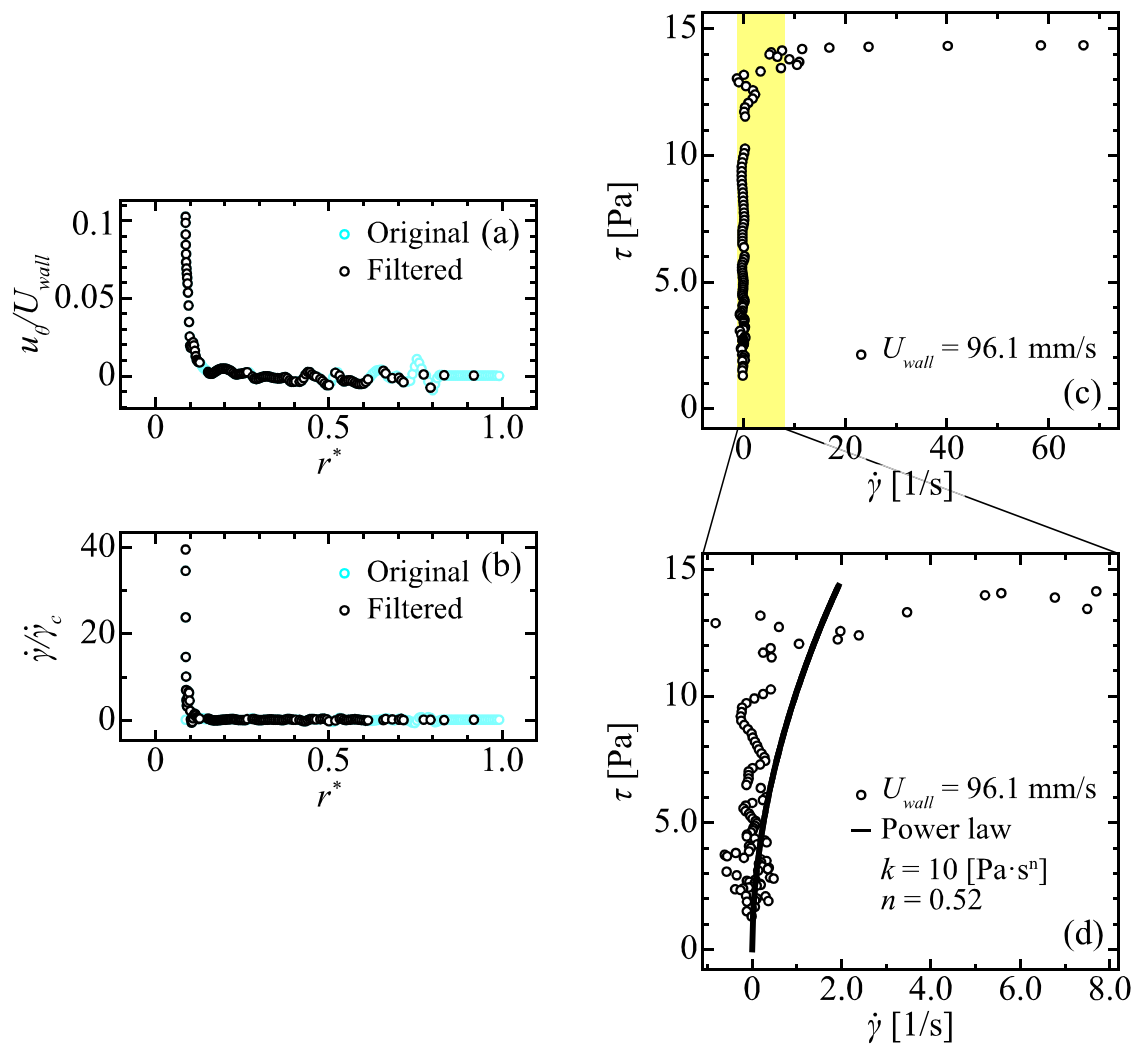


**Figure 3.6** Spatial distributions of (a) velocity, (b) shear rate, and (c) (d) flow curve of yogurt obtained with finite differential

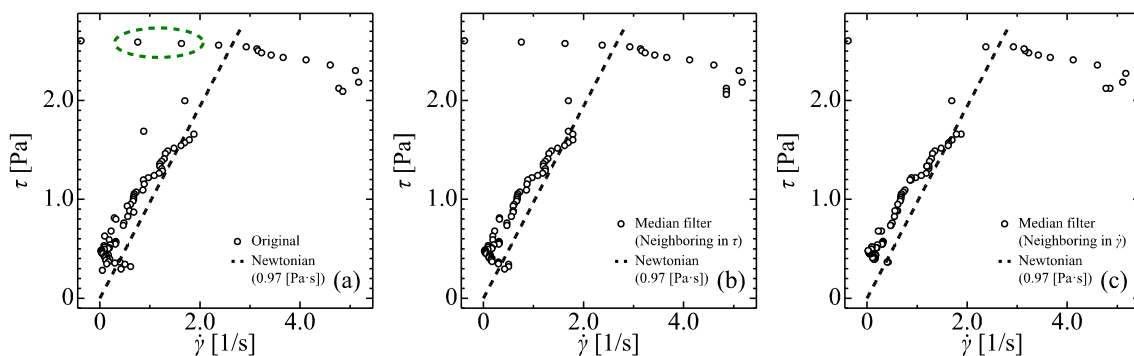


**Figure 3.7** Flow curves of silicone oil obtained from velocity profile (a) without median filter, (b) with median filter to data neighboring in shear stress, and (c) with median filter to data neighboring in shear rate

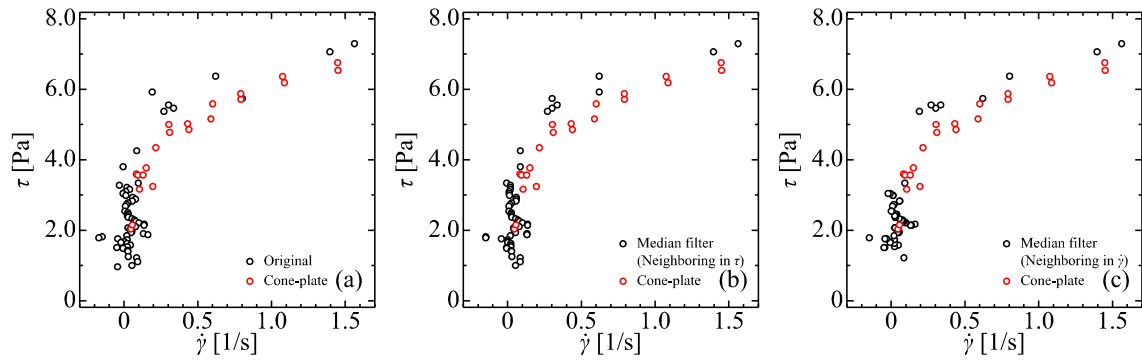


**Figure 3.8** Flow curves of PAA solution obtained from velocity profile (a) without median filter, (b) with median filter to data neighboring in shear stress, and (c) with median filter to data neighboring in shear rate

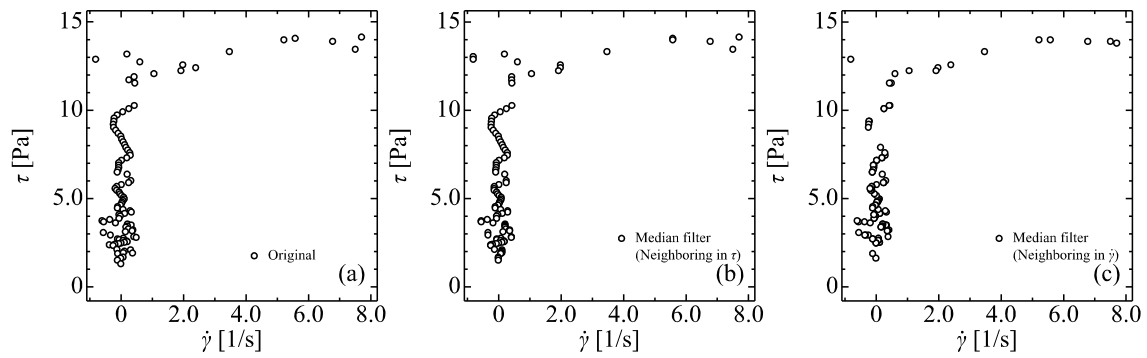


**Figure 3.9** Flow curves of yogurt obtained from velocity profile (a) without median filter, (b) with median filter to data neighboring in shear stress, and (c) with median filter to data neighboring in shear rate

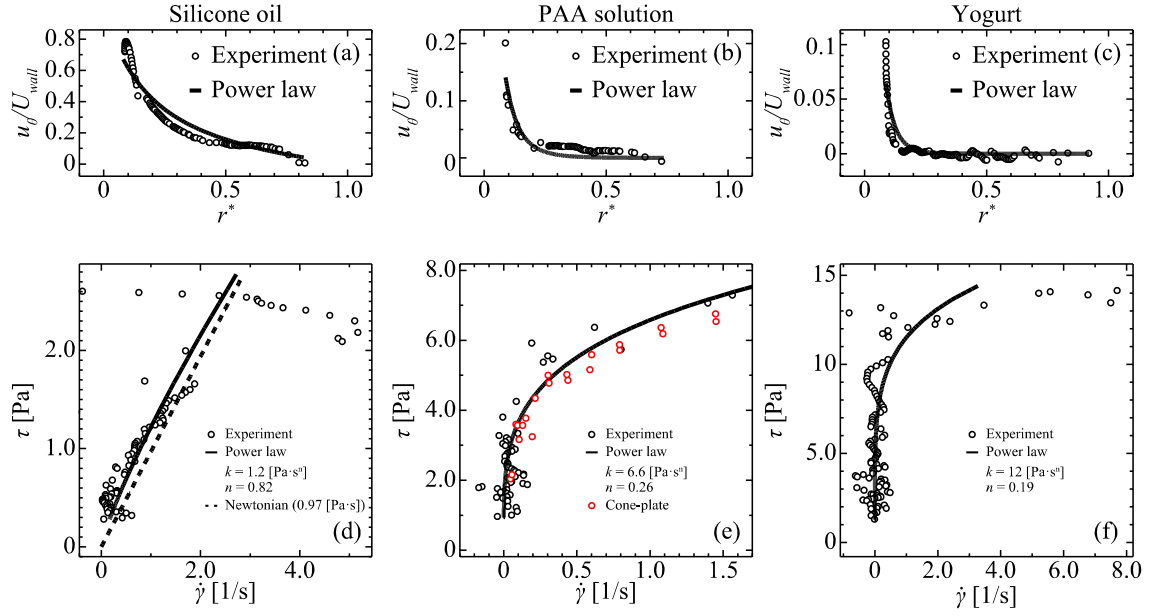


**Figure 3.10** Approximation curves from the power law function applied to (a)–(c) velocity distributions and (d)–(f) flow curves, for three test fluids: silicone oil (left panels), PAA solution (central panels), and yogurt (right panels)

### 3.4 Flow curve derivation without rheological model

We examined the applicability of general function-fitting techniques, power series polynomials, and Chebyshev expansion to estimate the measured flow curve. Such methods are called here model-free rheometry. The power series polynomial is described as

$$u_\theta(r) = \sum_{l=0}^m a_l r^l. \quad (3.40)$$

The coefficients,  $a_l$ , in the power series are determined by the least-square approximation for the measured velocity profile. It is expected that a third-order polynomial of the power series is high enough to describe shear rate distribution as a function of shear stress in the present flow configuration. It can express multiple-value functions like Fig. 3.11 [19]. To approximate  $u_\theta(\tau)$  with a power series, a fourth order is taken into account, because velocity is a spatially integrated quantity of shear rate. The function approximation is performed not only for  $u_\theta(r)$ , but also for  $u_\theta(\tau)$ , based on this expectation. We introduced power series polynomials of third, fourth, and fifth orders for both  $u_\theta(r)$  and  $u_\theta(\tau)$  approximations.

Approximation using power series polynomials is the most common practice in function approximation and is used to obtain fundamental characteristics. The power law is also represented by finite series of power polynomials, which therefore belong to

the same mathematical approach. Approximation curves for  $u_\theta(r)$  using power series polynomials are shown in Fig. 3.12 (a)–(c) as solid lines, and corresponding flow curves are shown in Fig. 3.12 (d)–(f). In the case of silicone oil, the velocity profile is approximated well by the polynomials with any order. The flow curves calculated from the approximated velocity profiles in Fig. 3.12 (d), however, do not follow the ideal Newtonian curve indicated by the dashed line, especially in the higher shear stress region,  $\tau > 1.6$  Pa. The influence of polynomial order is significant for the PAA solution. As shown in Fig. 3.12 (b), the lower order polynomials, third and fourth, do not match well with the velocity data, particularly in the high shear stress region. This is reflected in the corresponding flow curves, Fig. 3.12 (e). Furthermore, even at the fifth-order approximation, there remains a large discrepancy with the reference data from lower shear stress, where the higher order polynomial represent small fluctuations that originate from measurement errors. Therefore, neither the higher nor lower order polynomials lead to graphically acceptable representations of the velocity profiles over the whole region. The data of the yogurt, in Fig. 3.12 (c) and (f), display a similar trend. The results here show that the power series polynomials are not a valid method of representing the velocity profile near the inner cylinder, where the profile is much steeper than the other regions. This disadvantage becomes even more pronounced for shear-thinning fluids.

To address this issue we had to increase the order of polynomials to achieve better approximations that more fully resolve these steep profiles close to the inner cylinder. Unfortunately, this simultaneously induces higher-order wavy fluctuations in the approximated profiles. To avoid this dilemma, function approximation was performed for  $u_\theta(\tau)$  instead of  $u_\theta(r)$  with applying the variable transformation from  $r$  to  $\tau$ , using Eq. (3.6). If the flow curve is described by a third-order polynomial,  $u_\theta(\tau)$  would be approximated by a power series polynomial of the fourth order. Because of Eq. (3.6), the term of  $r^{-8}$  appears in  $u_\theta(r)$ , which explains why power series functions fail to follow  $u_\theta(r)$ , particularly near the inner cylinder.  $u_\theta(\tau)$  can therefore be approximated by a lower order polynomial than  $u_\theta(r)$  to capture the high shear rate region near the inner cylinder. In this power series approximation,  $u_\theta(\tau)$  is described as

$$u_\theta(\tau) = \sum_{l=0}^m b_l \tau^l . \quad (3.41)$$

The coefficients,  $b_l$ , are also determined by the least-square approximation. To approximate the flow curve by a function with a small number of terms, the Chebyshev expansion was examined. The Chebyshev expansion is known to give the best approximation of  $(m-1)$ th order polynomials for  $m$ th order power series polynomials,

and is given as

$$U_\theta = \frac{1}{2}c_0T_0(\sigma) + \sum_{l=1}^m c_l T_l(\sigma), T_n(\sigma) = \cos n\beta, \sigma = \cos\beta, \quad (3.42)$$

where  $U_\theta$  and  $\sigma$  are normalized velocity and shear stress, defined as

$$U_\theta = 2 \frac{u_\theta - u_{\min}}{u_{\max} - u_{\min}} - 1$$

$$\sigma = 2 \frac{\tau - \tau_{\min}}{\tau_{\max} - \tau_{\min}} - 1$$

The suffixes *max* and *min* indicate the maximum and minimum values in the range of approximation. The coefficients,  $c_l$ , are determined by the Chebyshev transform

$$c_l = \frac{2}{\pi} \int_0^\pi U_{\text{exp}}(\beta) \cos l\beta d\beta \quad (3.43)$$

where  $U_{\text{exp}}$  represents the experimental data of the velocity normalized by the same method mentioned previously. For the Chebyshev expansion, second, third, and fourth orders are examined. Functions of each order are expected to give the best approximation of power series polynomials of third, fourth, and fifth orders, respectively.

Figures 3.13, 3.14 and 3.15 show the experimental data and the approximation curves of  $u_\theta(\tau)$ ,  $u_\theta(r)$ , and  $\tau(\dot{\gamma})$ . In (a) of Figs. 3.13, 3.14 and 3.15, velocity,  $u_\theta$ , increases as shear stress,  $\tau$ , increases because both  $u_\theta$  and  $\tau$  are large near the rotating inner cylinder. By comparing  $u_\theta(\tau)$  and  $u_\theta(r)$ , the large velocity gradient in  $u_\theta(r)$  is decreased in  $u_\theta(\tau)$ . In the case of silicone oil,  $u_\theta$  is almost proportional to  $\tau$ , as in Fig. 3.13 (a), whereas the velocity gradient is large near the inner cylinder, in Fig. 3.13 (b). Thus, the power series polynomials give better approximations for  $u_\theta(\tau)$  than for  $u_\theta(r)$ , particularly in the PAA solution and the yogurt. In Fig. 3.14 (c), third- and fourth-order power series polynomials show a high shear rate, although they strongly underestimate the shear rate in Fig. 3.12 (e). Furthermore, in the case of the yogurt, shown in Fig. 3.15 (c), a high shear rate is expressed only by the fifth-order power series. It represents a flow curve that has a yield stress, yet no yield stress model was introduced. There is a linear relationship above the yield stress (about  $\tau_y = 10$  Pa), and zero shear rate under the yield stress. It is enough to predict flows of the test material. From the viewpoint of model-free rheometry, detecting the exact value of  $\tau_y$  is not a focused issue because the yield stress is one of models to explain flow phenomena. In cases the exact value is required, rheological model such as Bingham model should be introduced to the fitting. Even then, the present model-free rheometry can provide primary information which help to select a proper model from various yield stress models.

Approximation curves from Chebyshev expansion (by Eq. (3.42)) are shown in Figs. 3.16, 3.17 and 3.18. Although the number of the term is lower than in the power series polynomial, the fourth-order Chebyshev polynomial approximates well the flow curves of the silicone oil and the PAA solution. Focusing on the PAA solution, we evaluated the influence of polynomial order,  $m$ , on the quality of representation of the flow curve (assuming that the reference data obtained by the cone-plate rheometer gave correct rheological characteristics). Figure 3.19 shows the variation of square error,  $E$ , with respect to  $m$ . The dashed line in the figure shows the value of  $E$  for the approximation with power law model that has thus far been believed to give the best representation of the flow curve, as confirmed in previous chapter. In the case of the power series, indicated by black circles,  $E$  decreases as  $m$  increases for  $m < 5$ , because higher order polynomials give better approximations for the experimental value of  $u\theta(\tau)$ .  $E$  becomes minimal at  $m = 5$ , and increases as  $m$  increases for  $m > 5$ . In this region, measurement errors included in the data are also represented by higher order polynomials. In the case of the approximation with the Chebyshev expansion, a similar trend as with the power series appears.  $E$  is minimal at  $m = 4$ , and this result is compatible with the  $m$ th order Chebyshev polynomials, which consistently give the best approximation of  $(m+1)$ th order power series. Both polynomials produce approximation curves that are of comparable accuracy to the power law approximation.

In summary, our model-free ultrasonic rheometry provides an approximate continuous flow curve in a single rotation. This is enough for analytical and numerical predictions as long as the target fluid is continuum in the aspect of rheology. The shear-rate-dependent viscosity, which was not explicitly presented in this paper, is simply given by the ratio of the shear stress to the shear rate in the measured flow curve. If a specific fluid is under focus, combined use with a commercial rheometer and rheological models can obviously obtain a flow curve more precisely. In cases where the flow prediction of a new material is required without preliminary knowledge, our model-free rheometry can be applied. The required time for the measurement is short compared with commercial thin-gap rheometers, because the UVP is applied to a fluid domain with a wide distribution of shear rates. Our model-free ultrasonic rheometer is potentially useful in quickly obtaining flow curves of new materials.

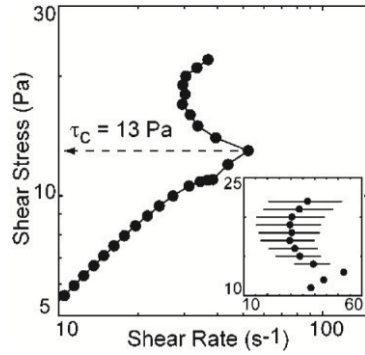


**Figure 3.11** Flow curve of a surfactant which has multiple values of shear stress [31]

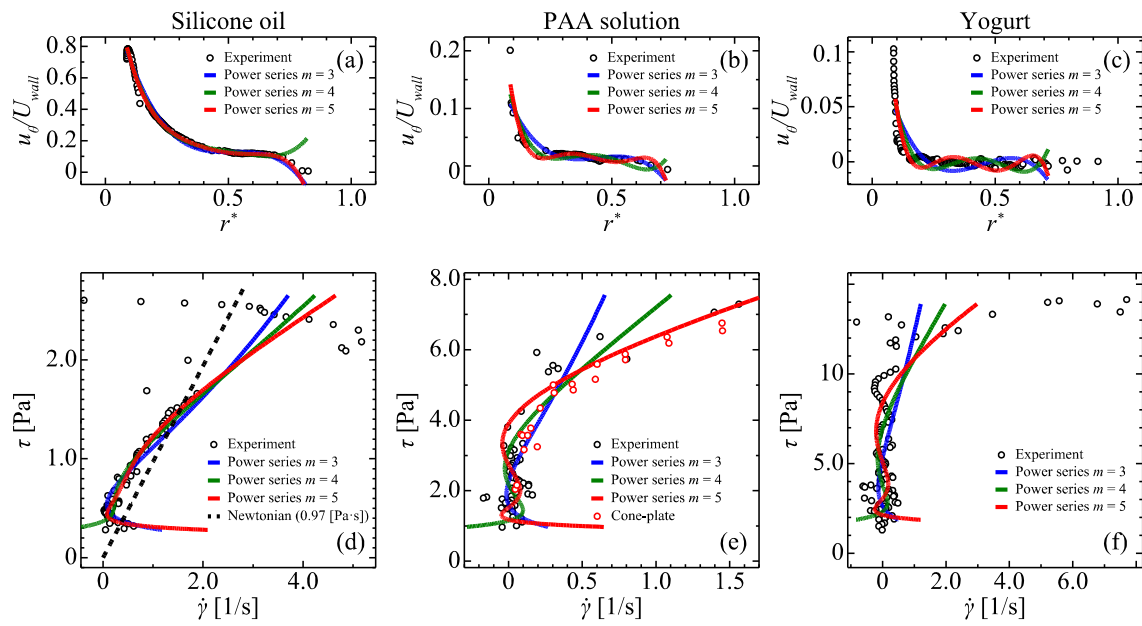


**Figure 3.12** Approximation for  $u(r)$  using power series polynomials, displayed on (a)–(c) velocity distributions and (d)–(f) flow curves, for three test fluids: silicone oil (left panels), PAA solution (central panels), and yogurt (right panels)

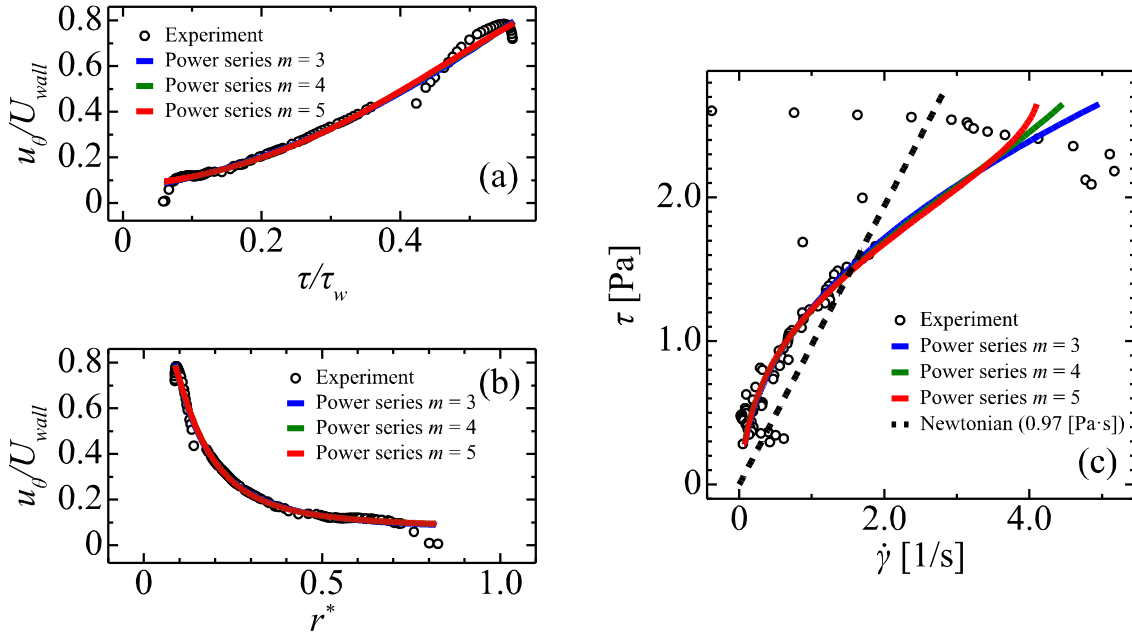


**Figure 3.13** Approximation for  $u(\tau)$  using power series polynomials, displayed on (a) relationship between velocity and shear stress, (b) velocity distributions and (c) flow curves, for silicone oil

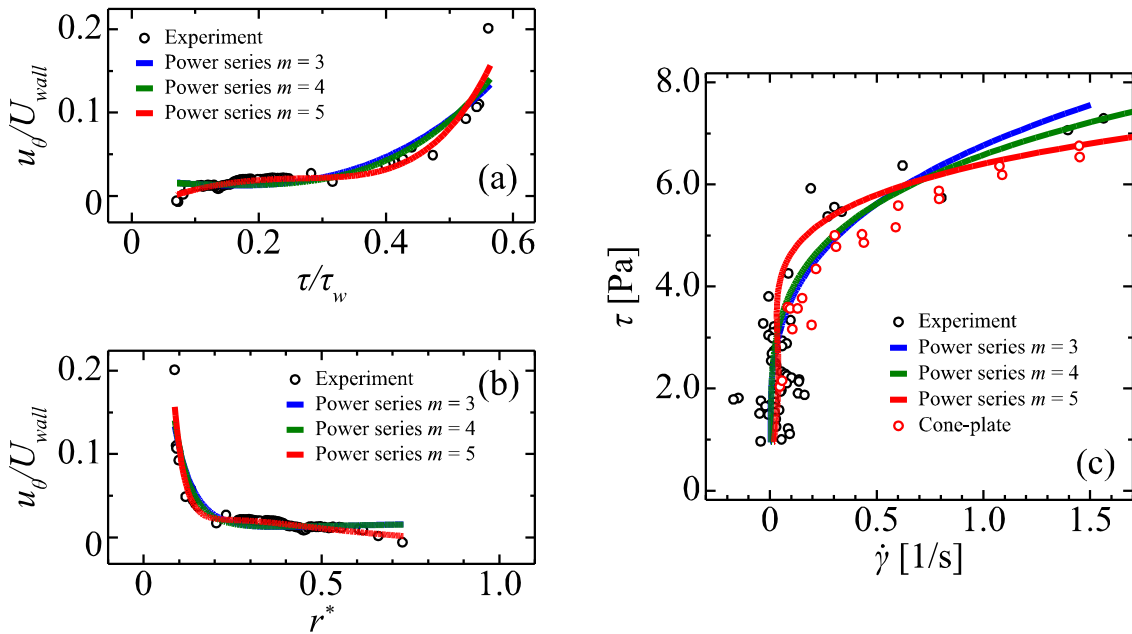


**Figure 3.14** Approximation for  $u(\tau)$  using power series polynomials, displayed on (a) relationship between velocity and shear stress, (b) velocity distributions and (c) flow curves, for PAA solution

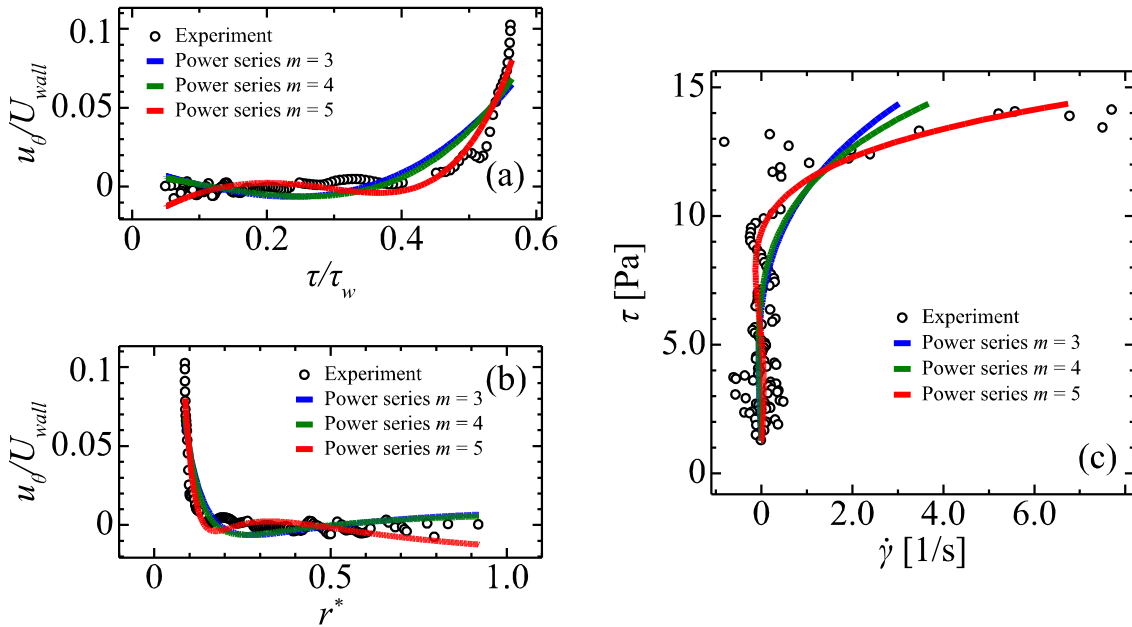


**Figure 3.15** Approximation for  $u(r)$  using power series polynomials, displayed on (a) relationship between velocity and shear stress, (b) velocity distributions and (c) flow curves, for yogurt

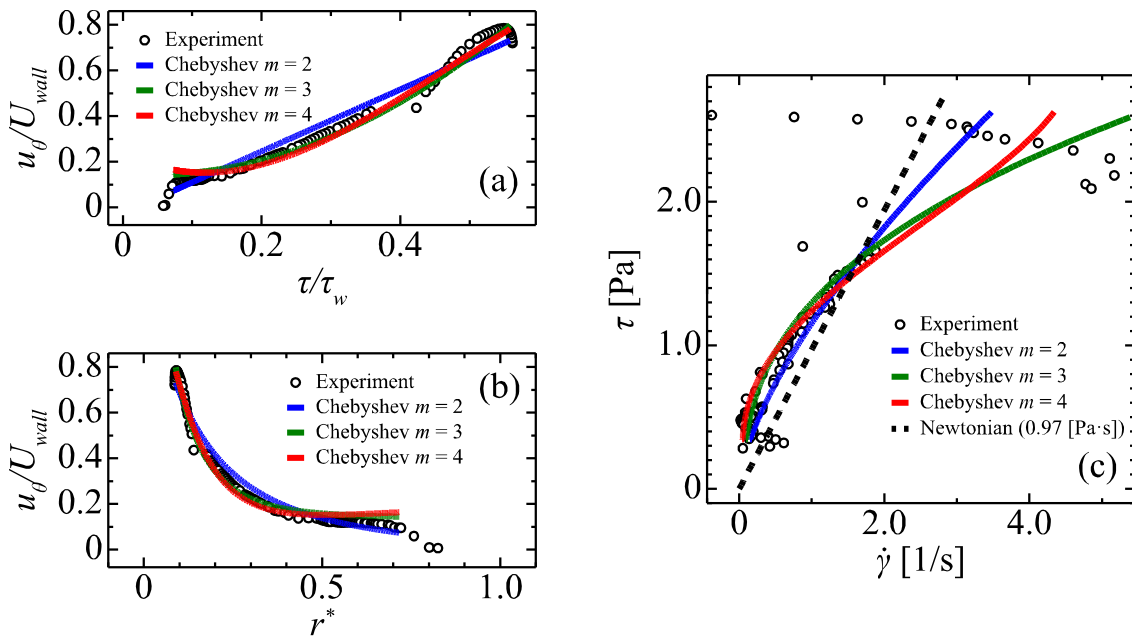


**Figure 3.16** Approximation for  $u(r)$  using Chebyshev expansions, displayed on (a) relationship between velocity and shear stress, (b) velocity distributions, and (c) flow curves, for silicone oil

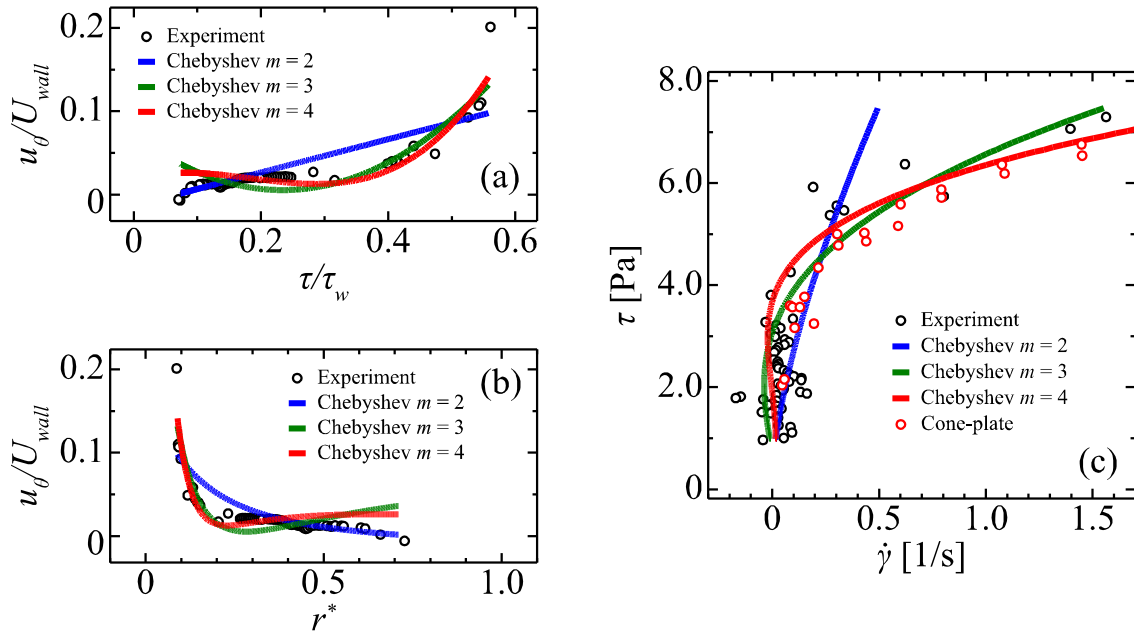


**Figure 3.17** Approximation for  $u_a(\tau)$  using Chebyshev expansions, displayed on (a) relationship between velocity and shear stress, (b) velocity distributions, and (c) flow curves, for PAA solution

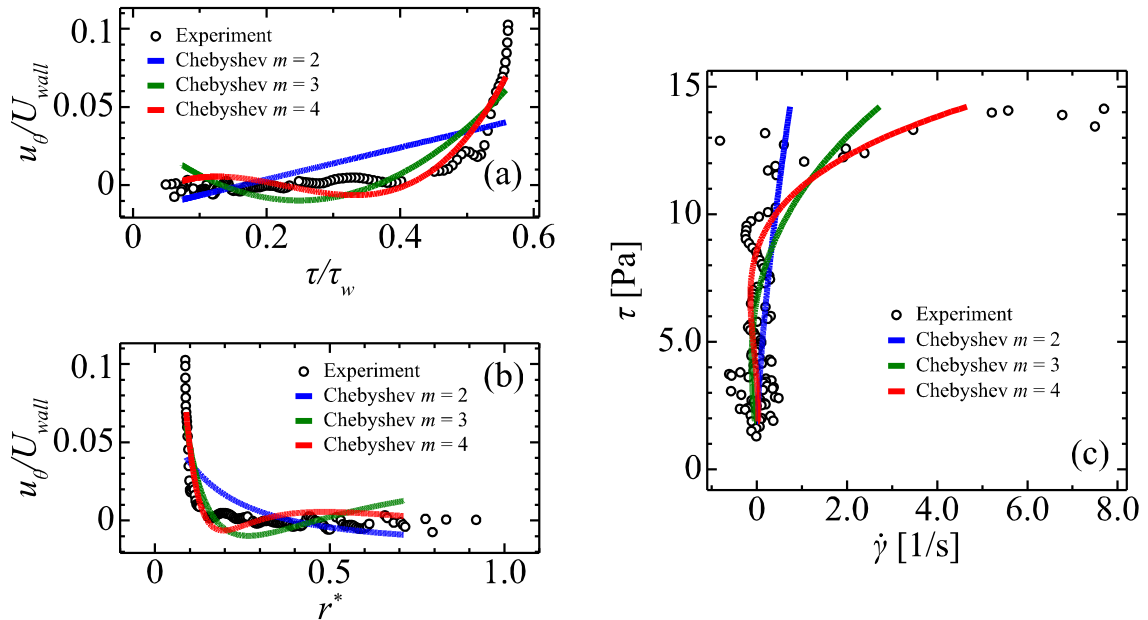


**Figure 3.18** Approximation for  $u_a(\tau)$  using Chebyshev expansions, displayed on (a) relationship between velocity and shear stress, (b) velocity distributions, and (c) flow curves, for yogurt

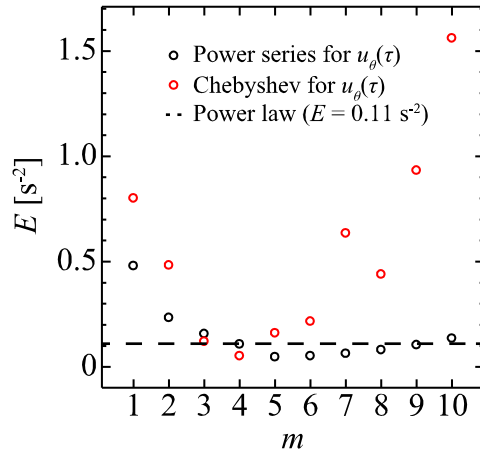


**Figure 3.19** Square errors,  $E$ , of flow curves of PAA solution, obtained using power series polynomials, Chebyshev expansion, and power law.  $E$  varies with polynomial order,  $m$ , compared with the flow curve obtained with a cone-plate rheometer

### 3.5 Conclusion

We proposed a model-free ultrasonic rheometry designed to evaluate shear-rate-dependent viscosity quantitatively. This is realized by introducing ultrasonic velocity profiling (UVP) to a double cylinder configuration with a wide gap. The flow curves were calculated from function approximation curves of the velocity data, measured by UVP. This extracted the primary rheological characteristics of the materials without amplifying measurement errors. Flow curves of silicone oil, polyacrylamide solution, and yogurt were measured to evaluate the applicability of this technique. These liquids are examples of Newtonian fluids, non-Newtonian fluids, and opaque fluids with unknown properties, respectively. For the function approximations, fundamental power series polynomials and Chebyshev polynomials were examined. The order of polynomial was kept relatively lower to prevent artifacts in the flow curves produced by measurement errors in the velocity. We suggest that function approximation of the velocity as the variable of shear stress gives better representation than on the radial velocity profiles. This is because conversion from the radial position to the shear stress can relax the steep variation of the velocity profile near the inner cylinder, which obstructs the function approximations using lower order polynomials. Function approximations using fourth-order Chebyshev polynomials provided good representations of the flow curves of shear-thinning PAA solution.

We would like to emphasize that the present model-free rheometry provides a quantitative outline of the rheological characteristics of a material. However, model-based rheometry provides more accurate representations of the rheological

characteristics if a suitable rheological model is applied to the fluids under examination. Though as mentioned previously, the application of an unsuitable model will result in severe miscalculation of the rheological characteristics and produce huge errors. The flow curve measurement of our technique is designed to exclude such a model-dependent process, which allows users to be emancipated from preliminary knowledge of rheological property if they face unknown materials. The measurement of flow curves of yogurt was an example of an opaque unknown material whose properties easily fluctuate. Finally, we would like to summarize three potential advantages of our rheometry: (A) it is applicable to fluid materials, including multiphase fluids such as large ingredients mixed in fluids, because of the wider gap between cylinders, (B) it has a much shorter operational time so that materials with time-fluctuating properties can be correctly measured, and (C) it presents flow curves in continuous style, achieving numerical simulations of arbitrary flows by directly referring to the flow curve in the equation of fluid motion.

#### References

- [1] C. W. Macosko, *Rheology: Principles, Measurements, and Applications*, Wiley-VCH, New York, 1994
- [2] P. Schall, M. Hecke, Shear bands in matter with granularity, *Annu. Rev. Fluid Mech.* 42 (2010) 67-88
- [3] Y. Murai, T. Shiratori, I. Kumagai, P. Rühs, P. Fischer, Effective viscosity measurement of interfacial bubble and particle layers at high volume fraction, *Flow Meas. Instrum.* 41 (2015) 121-128
- [4] R. Darby, Couette viscometer data reduction for materials with a yield stress, *J. Rheol.* 29 (1985) 369-378
- [5] V. C. Kelessidis, R. Maglione, Modeling rheological behavior of bentonite suspensions as Casson and Robertson–Stiff fluids using Newtonian and true shear rates in Couette viscometry, *Powder Technol.* 168 (2006) 134-147
- [6] P. Estellé, C. Lanos, A. Perrot, Processing the Couette viscometry data using a Bingham approximation in shear rate calculation, *J. Non-Newtonian Fluid Mech.* 154 (2008) 31-38
- [7] G. Heirman, L. Vandewalle, D. Van Gemert, Ó Wallevik, Integration approach of the Couette inverse problem of powder type self-compacting concrete in a wide-gap concentric cylinder rheometer, *J. Non-Newtonian Fluid Mech.* 150 (2008) 93-103
- [8] I. M. Krieger, Shear rate in the Couette viscosimeter, *Trans. Soc. Rheol.* 12 (1968) 5-11

- [9] T. M. T. Yang, I. M. Krieger, Comparison of methods for calculating shear rates in coaxial viscometers, *J. Rheol.* 22 (1978) 413-421
- [10] Q. D. Nguyen, D. V. Boger, Characterization of yield stress fluid with concentric cylinder viscometers, *Rheol. Acta* 26 (1987) 508-515
- [11] F. R. De Hoog, R. S. Anderssen, Approximate solutions for the Couette viscometry equation, *Bull. Austral. Math. Soc.* 72 (2005) 461-470
- [12] Y. L. Yeow, W. C. Ko, P. P. P. Tang, Solving the inverse problem of Couette viscometry by Tikhonov regularization, *J. Rheol.* 44 (2000) 1335-1351
- [13] C. Ancy, Solving the Couette inverse problem using a wavelet-vaguelette decomposition, *J. Rheol.* 49 (2005) 441-460
- [14] B. Ouriev, E. J. Windhab Rheological study of concentrated suspensions in pressure-driven shear flow using a novel in-line ultrasound Doppler method, *Exp. Fluids* 32 (2002) 204-211
- [15] B. Ouriev, E. J. Windhab, Novel ultrasound based time averaged flow mapping method for die entry visualization in flow of highly concentrated shear-thinning and shear-thickening suspensions, *Meas. Sci. Technol.* 14 (2003) 140-147
- [16] B. H. Birkhofer, S. A. K. Jeelani, E. J. Windhab, B. Ouriev, K. J. Lisner, P. Braun, Y. Zeng, Monitoring of fat crystallization process using UVP-PD technique, *Flow Meas. Instrum.* 19 (2008) 163-169
- [17] J. Wiklund, M. Standing, A. J. Pettersson, A. Rasmuson A comparative study of UVP and LDA techniques for pulp suspensions in pipe flow, *AIChE J.* 52 (2006) 484-495
- [18] J. Wiklund, I. Shahram, M. Standing, Methodology for in-line rheology by ultrasound Doppler velocity profiling and pressure difference techniques, *Chem. Eng. Sci.* 62 (2007) 4277-4293
- [19] J. Wiklund, M. Standing, Application of in-line ultrasound Doppler-based UVP-PD rheometry method to concentrated model and industrial suspensions, *Flow Meas. Instrum.* 19 (2008) 171-179
- [20] V. C. Kelessidis, R. Meglione, Modeling rheological behavior of bentonite suspensions as Casson and Robertson-Stiff fluids using Newtonian and true shear rates in Couette viscometry, *Powder Technol.* 168 (2006) 134-147
- [21] B. Derakhshandeh, D. Vlassopoulos, S. G. Hatzikiriakos, Thixotropy, yielding and ultrasonic Doppler velocimetry in pulp fibre suspensions, *Rheol. Acta.* 51 (2012) 201-214
- [22] T. Gallot, C. Perge, V. Grenard, M. Fardin, N. Taberlet, S. Mannville, Ultrafast ultrasonic imaging coupled to rheometry: principle and illustration, *Rev. Sci. Instrum.*

84 (2013) 045107

- [23] F. Rodríguez-González, J. Pérez-González, L. Vargas, B. M. Marín-Santibáñez, Rheo-PIV analysis of the slip flow of a metallocene linear low-density polyethylene melt, *Rheol. Acta.* 49 (2010) 145-154
- [24] C. J. Dimitriou, L. Casanellas, T. J. Ober, G. H. McKinley, Rheo-PIV of a shear-banding wormlike micellar solution under large amplitude oscillatory shear, *Rheol. Acta.* 51 (2012) 395-411
- [25] J. Pérez-González, J. J. López-Durán, B. M. Marín-Santibáñez, F. Rodríguez-González, Rheo-PIV of a yield-stress fluid in a capillary with slip at the wall, *Rheol. Acta.* 51 (2012) 937-946
- [26] T. Shiratori, Y. Tasaka, Y. Murai, Y. Takeda, Development of ultrasonic visualizer for capturing the characteristics of viscoelastic fluids, *J. Vis.* 16 (2013) 275-286
- [27] P. Cheng, K. Liu, Linear surface waves in roll coating flows of thin viscoelastic polymer liquid films using power-series approximation approach techniques, *Int. Sympos. Comput. Consum. Control* (2012) 801-804
- [28] H. T. Jongen, P. Jonker, F. Twilt, *Nonlinear optimization in finite dimensions: Morse theory, Chebyshev approximation, transversality, flows, parametric aspects*, Springer, Boston, 2000
- [29] A. Einstein, Eine neue Bestimmung der Moleküldimensionen. *Ann Phys* 19 (1906) 289–306
- [30] A. Esser, S. Grossmann, Analytic expression for Taylor-Couette stability boundary, *Phys. Fluids* 8 (1996) 1814
- [31] V. Herle, P. Fischer, E. J. Windhab, Stress driven shear bands and the effect of confinement on their structures: a rheological, flow visualization, and Rheo-SALS study, *Langmuir* 21 (2005) 9051-9057

#### 4.1 Introduction

Prediction of non-Newtonian fluid flows becomes increasingly important in material processing. In the field of food process engineering, for example, flow during food processing has to be predicted and controlled because the flow determines taste and texture of the food. The prediction of non-Newtonian flow is difficult because Newton's law of viscosity cannot be introduced to flow simulation: In cases of Newtonian flow, equations to describe the flow are solvable as simultaneous equations of momentum conservation, mass conservation and Newton's law of viscosity, as Fig. 4.1 (a) shows. For non-Newtonian flows, however, the equations are not solvable because Newton's law of viscosity cannot describe the fluid motion. Then an alternative equation to Newton's law, called constitutive equation, is introduced to simulations as Fig. 4.1 (b) shows. As the constitutive equation represent the relation between deformation and stress, simultaneous equations are closed and a flow field is given as a solution.

Because the academic discipline about flow and deformation of materials, called rheology, has been developed based on materials science, many of constitutive equations were established for each group of materials. In the case of polymeric materials, for example, dynamics of polymers is described by models in different length scales [1-3]. In the most resolved length scale, each atoms in the polymer molecule is described as the model, and motion of them is taken into account. In longer length scale, the detail of the chain structure is ignored through coarse-graining, and the chains are described as uncrossable strings. In the largest length scale to represent fluid flows, a relation between macroscopic deformation and stress is described by a constitutive equation. Models to describe deformation and stress are established in each length scales, and the models are coupled by determining model constants from dynamics in different length scales.

Because they are based on dynamics in smaller length scales, constitutive equations derived by this way cannot be applied for materials with different materials. For example, constitutive equations for polymeric fluids are not applicable to describe food flows. Because constitutive equations are particularized for each materials, it is difficult to choose a proper model to predict flows. In the case that flow simulation of new material is required, the choice of a model is particularly difficult. To establish a method which is applicable for various kinds of fluids, we employed an idea to introduce experimental information to numerical simulation. Figure 4.1 (c) presents a schematic of the simulation with experimental information. In flow simulations of

inelastic fluids with shear-rate-dependent viscosity, the relation between shear rate and shear stress, called flow curve, has been introduced. To express viscoelasticity, not only shear rate but also strain should be employed as a factor to determine shear stress. Thus we expressed fluid property in the form of “flow surface” which describes the relation among shear rate, strain and shear stress.

To introduce experimental flow surface to flow simulation, much amount of data about the relation among the three quantities should be obtained in a short time. This requirement was satisfied by employing fluid velocimetries, such as particle imaging velocimetry (PIV) and ultrasonic velocity profiling (UVP). Spatio-temporal distributions of the quantities were converted to the flow surface. As a configuration to realize velocity distribution, and derive shear stress distribution, concentric cylinders with cylinders with a large gap were introduced. Characterization of non-Newtonian fluids based on velocimetry has been developed in previous researches. For example, PIV [4-8], UVP [9-13], LDA (laser Doppler anemometer) [12] and NMR (nuclear magnetic resonance) [14,15] are utilized to characterize non-Newtonian fluids. We extend the function of velocimetry-based characterization from two viewpoints. Firstly, the present method aim to characterize not only shear-rate-dependent viscosity but also viscoelasticity whereas previous researches focus on shear-rate-dependent viscosity. Because measurement of unsteady flow is required to characterize viscoelasticity, oscillating flow after the spin up of inner cylinder was measured. Secondly, we are developing fluid characterization which can predict flows without any rheological models. Previous researches about velocimetry-based characterization have introduced rheological model such as power law and Herschel-Bulkley model to predict flows with high accuracy. Because we accord central importance to wide applicability of characterization, experimental data itself is implemented in flow prediction as Fig. 4.1 (c) shows. We have already performed visualization of unsteady flows in Chapter 2, and succeeded in quantifying shear-rate-dependent viscosity in Chapter 3 to realize widely-applicable characterization. As the flow surface is defined as property of the fluid, dynamics in smaller length scale is not taken into account. This concept is similar to “eddy viscosity” in turbulent modeling which regard eddy dynamics as a change of fluid property.

The rest of this paper is consist of five sections. In Section 4.2, experimental apparatus is presented. In Section 4.3, influence of viscoelasticity and shear-rate-dependent viscosity is qualitatively read out from the measured velocity profiles. In Section 4.4, the procedure to obtain the flow surface from the measured velocity distribution is explained. The derived flow surfaces are shown here, and we present how

viscoelasticity and shear-rate-dependent viscosity are expressed in the flow surface. In Section 4.5, a numerical simulation with the flow surface is performed as an example of application. In Section 4.6, we state significance of the characterization with flow surface as conclusion.

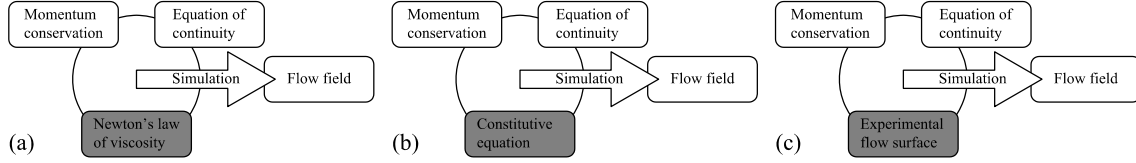


**Figure 4.1** Schematic illustration of flow prediction for (a) Newtonian fluids, (b) non-Newtonian fluids in conventional way, and (c) non-Newtonian fluids in present way

## 4.2 Experimental setup

As the experimental apparatus, concentric cylinders, which are also used in Chapter 3, are introduced as shown in Fig. 4.2. Radii of the inner cylinder,  $r_{in}$ , and outer cylinder,  $r_{out}$ , are 15.0 mm and 71.5 mm, respectively. The flow between the cylinders is assumed to be one-directional. For more detail on the geometry of the apparatus, refer Section 3.2. Because unsteady flow should be analyzed to quantify viscoelasticity, the torque sensor connected to the inner cylinder (Bohlin Visco88; Malvern Instruments Ltd., Malvern, U.K.) records time variation of torque  $T(t)$ . Thus shear stress on the inner cylinder wall is derived as time variation  $\tau_{wall}(t)$  by

$$\tau_{wall}(t) = -\frac{T(t)}{2\pi r_{in}^2 H}, \quad (4.1)$$

where  $H = 50$  mm is the height of the inner cylinder. The inner cylinder starts rotation at  $t = 0$  with the rotational velocity of  $U_{wall} = 31.1$  mm/s.

As velocity measurement technique, ultrasonic velocity profiling (UVP) and particle tracking velocimetry (PTV) were introduced. The introduced UVP device is UVP-DUO (Metflow S.A., Lausanne, Switzerland), and an ultrasonic transducer was installed at the same position as the setup in Chapter 3 as shown in Fig. 4.2 (a): Distance between the measurement line and the center line  $d$  equals 20 mm. Velocity component obtained by UVP  $u_x$  is converted to  $u_\theta$  by

$$u_\theta = \frac{u_x}{\cos \alpha}, \quad (4.2)$$

where  $\alpha$  is the angular coordinate of the measurement point against the center of the cylinder, as shown in Fig. 4.2 (a). To obtain particle images, a high speed video camera (FASTCAM-MAX; Photron Ltd., Tokyo, Japan) was adopted. The images were

recorded from the top of the apparatus as shown in Fig. 4.2 (b). A measurement cross section was illuminated with a laser light sheet (G50; Kato Koken Co. Ltd., Isehara, Japan). The high speed video camera records a series of images like Fig. 4.3 (a). Because focal area of images taken by the high speed video camera was not parallel to the illuminated cross section, particle position was calibrated with a calibration board shown in Fig. 4.3 (b). To obtain velocity distribution, 4-frame particle tracking was introduced. Figure 4.3 (c) is one of examples of the obtained velocity vectors. These velocity vectors are relocated to  $r$ - $\theta$  coordinate as shown in Fig. 4.3 (d). Data acquisition of the torque sensor, the UVP and the high speed video camera was started simultaneously.

The test fluids are 1000 cSt silicone oil (KF96-1000cs; Shin-Etsu Chemical Co., Ltd., Tokyo, Japan) and 1.0 wt% PAA solution (AP805C; Dia-Nitrix Co., Ltd., Tokyo, Japan). Differently from Chapter 3, velocity profile of yogurt was not analyzed because only PIV provide high time resolution enough to derive unsteady shear stress distribution. In Fig. 4.4, rheological properties of the PAA solution measured with a commercial cone-plate rheometer (Bohlin CVO; Malvern Instruments Ltd., Malvern, U.K.) is shown. The flow curve shown in Fig. 4.4 (a) indicates that the PAA solution is shear thinning fluid as discussed in Chapter 3. Phase angle, storage modulus and loss modulus, shown in Fig. 4.4, are obtained by dynamic viscoelasticity measurement with the commercial cone-plate rheometer. In the measurement, oscillatory deformation is applied to the test fluid. Then time variations of shear strain and shear rate are described by Eqs. (4.3) and (4.4), respectively,

$$\gamma(t) = \gamma_0 \cos 2\pi ft, \quad (4.3)$$

$$\dot{\gamma}(t) = -2\pi f \gamma_0 \sin 2\pi ft, \quad (4.4)$$

where  $\gamma_0$  and  $f$  are amplitude and frequency of the applied strain, respectively. Then, shear stress generated by the viscoelastic fluid is expected to have same frequency  $f$  as strain and shear rate. If the test material was Hookean solid, shear stress has same phase as strain:  $\tau(t) = \tau_0 \cos 2\pi ft$ . If the test material is Newtonian fluid, on the other hand, shear stress has same phase as shear rate:  $\tau(t) = \tau_0 \cos(2\pi ft + \pi/2)$ . Therefore, shear stress of viscoelastic fluid is described as

$$\tau(t) = \tau_0 \cos(2\pi ft + \delta), \quad (0 < \delta < \pi/2). \quad (4.5)$$

The viscoelasticity of the test fluid is quantified by the phase angle  $\delta$ . From Eqs. (4.3), (4.4) and (4.5), the relationship between shear rate, shear strain and shear stress is described as

$$\tau(t) = G' \gamma(t) + \frac{G''}{2\pi f} \dot{\gamma}(t), \quad (4.6)$$

$$G' = \frac{\tau_0}{\gamma_0} \cos \delta, \quad (4.7)$$

$$G'' = \frac{\tau_0}{\gamma_0} \sin \delta, \quad (4.8)$$

where  $G'$  and  $G''$  mean storage and loss moduli, respectively. The first term in the right-hand side of Eq. (4.6) is contribution of elasticity to shear stress while the second term is viscous contribution. In the measurement, phase angle  $\delta$  is obtained by comparing  $\gamma(t)$  and  $\tau(t)$  acquired with the rheometer, and  $G'$  and  $G''$  are derived by Eqs. (4.7) and (4.8). Figure 4.4 (b) shows that the PAA solution has viscoelasticity because  $G'$  and  $G''$  have comparable magnitude. According to  $\delta(f)$  shown in Fig. 4.4 (b), the PAA solution behave more elastic as the applied frequency  $f$  increases while  $f < 3$  Hz. When higher frequency than 3 Hz is applied,  $\delta(f)$  shows that the PAA solution behave viscous rather than elastic as  $f$  increases. It is to be noted that  $\tau(t)$  might not obey Eq. (4.5) under such a high frequency, and thus the requirement for the dynamic viscoelasticity measurement is not fulfilled. Figure 4.4 shows that the PAA solution has both shear-rate-dependent viscosity and viscoelasticity. In the flow with the experimental apparatus in Fig. 4.2, therefore, the flow immediately after the start of inner cylinder rotation is governed by viscoelasticity. By continuing the rotation for a longer time than relaxation time of the fluid, the flow converges to a steady state that is governed by shear-rate-dependent viscosity. A method to derive shear-rate-dependent viscosity with spatial distribution of  $u_\theta$  under the steady state was already presented in Chapter 3. In this Chapter, viscoelasticity of the test fluid was characterized with time-dependent velocity profile information right after the start of the rotation.

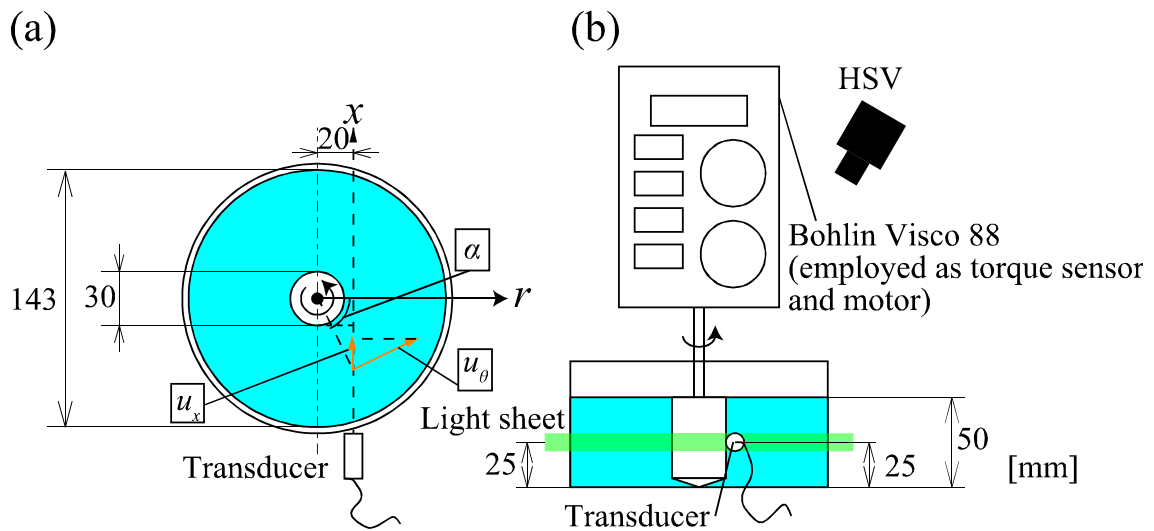


**Figure 4.2** (a) Top view and (b) side view of the experimental apparatus

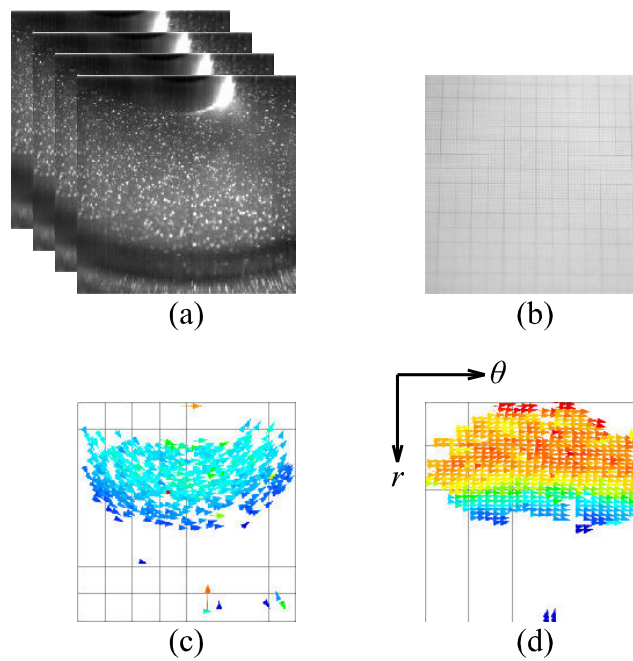


**Figure 4.3** Procedure of image processing: (a) original images (b) calibration board (c) velocity vectors obtained by PTV (d) velocity vectors after relocation

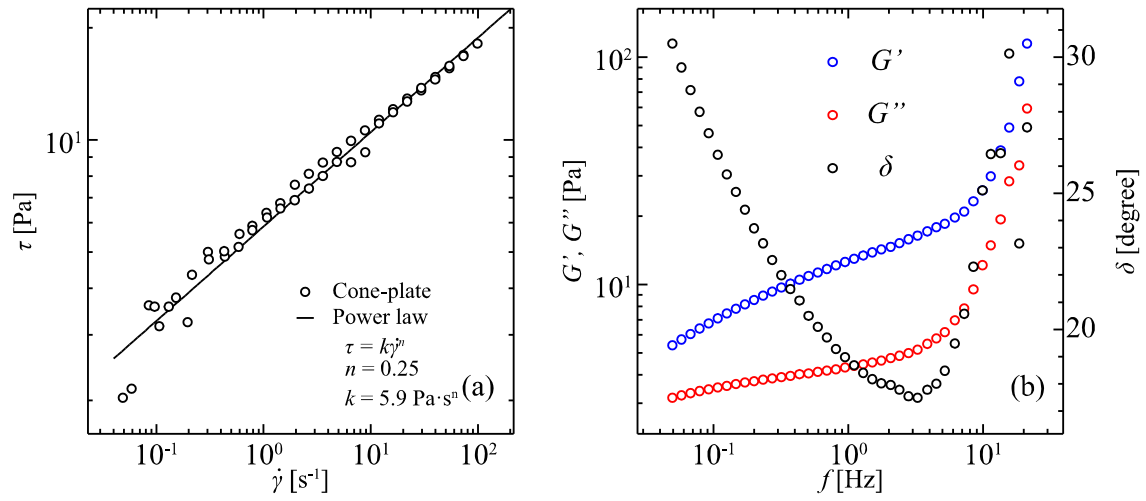


**Figure 4.4** (a) Flow curve and (b) phase angle, storage modulus and loss modulus depending on frequency, for 1.0 wt% polyacrylamide solution obtained with a commercial cone-plate rheometer

### 4.3 Spatio-temporal velocity distributions

Time variations of torque and velocity distributions are shown in Fig. 4.5. The left axes of Fig. 4.5 (a) and (b) show the measured torque, and the right axes show shear stress obtained with Eq. (4.1) from the measured torque. Figure 4.5 (c) and (d) indicate spatio-temporal distributions of the circumferential velocity component  $u_\theta$  obtained with Eq. (4.2). Although PTV obtains two dimensional distribution of velocity vectors with two components,  $u_\theta$  is averaged for  $\theta$  direction in all range of  $\theta$  in Fig. 4.3 (d). The averaged distribution of  $u_\theta$  is shown as Fig. 4.5 (e) and (f).

The difference of rheological property between the silicone oil and the PAA solution appears both in the velocity distribution and the torque variation. Figure 4.5 (c) and (e) show that velocity of the silicone oil is increased from the inner wall side after the inner cylinder start rotation, and approaches to the steady state, rigid body motion, until about  $t = 0.5$  s. This is so-called ‘spin-up’. Because spatio-temporal distribution of velocity is described as diffusion equation in spin-up flows, and kinematic viscosity corresponds to its diffusion coefficient, flows reach the steady state in shorter time in case that viscosity of the fluid is higher. Thus the measured velocity distributions contain information about viscosity of test fluids. Velocity distributions of the PAA solution in Fig. 4.5 (d) and (f) follow similar spin-up process with the silicone oil. However, deceleration occurs after once the velocity increases as observed between  $t = 1.0$  and  $2.0$ . This velocity distribution implies that the test fluid has viscoelasticity. The PAA solution is driven in a wide range right after the inner cylinder start rotation because it behaves as an elastic material in a short time after deformed. As time advances the PAA solution decelerates. After the deceleration, the flow is driven only near the inner cylinder in the steady state. In the steady state of concentric cylinder systems, shear stress distribution is theoretically described as

$$\tau_{r\theta}(r) = \tau_{wall} \left( \frac{r_{in}}{r} \right)^2, \quad (4.9)$$

which is independent from the fluid property. Near the inner cylinder where fluids experience high shear stress, viscosity of shear thinning fluids is lower than that near the outer cylinder. In this reason, the PAA solution has velocity only near the inner cylinder in Fig. 4.5 (f) in the steady state compared with the silicone oil in Fig. 4.5 (e). In shear stress variation of the silicone oil, shown as Fig. 4.5 (a), shear stress monotonically increases. If rotational velocity of the inner cylinder jumped from 0 to  $U_{wall}$  at  $t = 0$  as a step function, the shear stress should also jump at  $t = 0$ , and decrease after that. The gradual, monotonic increase of the shear stress implies that the rotational velocity of

inner cylinder does not obey step function, but gradually increases because of characteristics of the equipment. This is a suitable to have relatively longer time range on the data for analysis and is not a problem, because any assumptions about the rotational velocity are not required in the analysis to obtain shear stress distribution and flow surface. The shear stress of PAA, shown in Fig. 4.5 (b), has a maximum at  $t = 2.0$ . Shear stress increases proportionally to fluid deformation until the maximum shear stress. Then, shear stress decreases because of stress relaxation that the fluid releases elastic energy.

In rheological characterization, relation among shear rate, strain and shear stress is investigated. In these three quantities, shear rate and strain are derived by simple differential and integral calculations. But local shear stress cannot be obtained only from the velocity distribution. In the next section, we propose how to derive the shear stress distribution by introducing momentum conservation. Then the three quantities to characterize the test fluid are derived from the experimental data. We will interpret physical meanings included in the obtained flow surface.

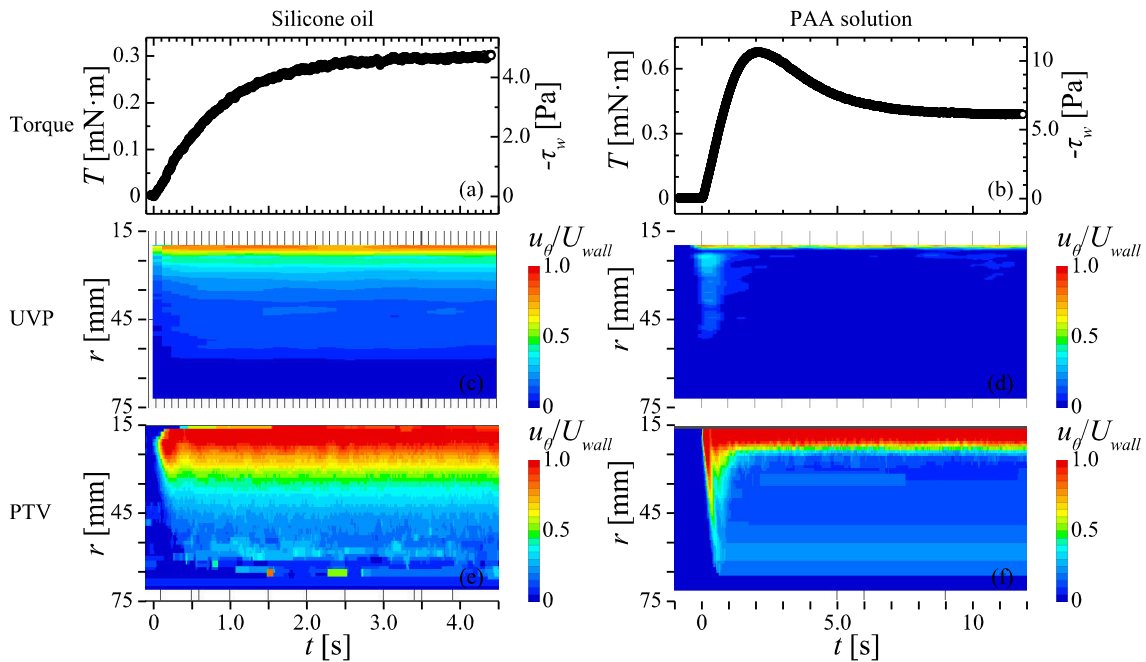


**Figure 4.5** (a)-(b) Time variation of torque, and spatio-temporal velocity distribution measured by (c)-(d) UVP, and (e)-(f) PTV for silicone oil (left panels) and PAA solution (right panels)

#### 4.4 Quantification of viscoelasticity

##### 4.4.1 Procedure to derive shear stress distribution

Figure 4.6 shows the procedure to derive spatio-temporal distributions of shear rate, strain and shear stress from velocity distribution and shear stress variation obtained experimentally. The three quantities correspond to three axes of the flow surface. As shown in Fig. 4.5, shear stress on the wall of the inner cylinder,  $\tau_{wall}$ , and spatio-temporal distribution of circumferential velocity component,  $u_{\theta}(r,t)$ , were obtained in the experiment. Shear rate distribution  $\dot{\gamma}_{r\theta}(r,t)$  and strain distribution  $\gamma_{r\theta}(r,t)$  are derived simply from  $u_{\theta}(r,t)$  by calculating gradient and integral, namely,

$$\dot{\gamma}_{i,j} = \frac{u_{i+1,j} - u_{i-1,j}}{r_{i+1} - r_{i-1}} - \frac{u_{i,j}}{r_i}, \quad (4.10)$$

$$\gamma_{i,j} = \sum_{k=0}^j \dot{\gamma}_{i,k} \Delta t, \quad (4.11)$$

where  $\dot{\gamma}_{i,j}$  and  $\gamma_{i,j}$  are discrete shear rate and strain, respectively. Subscripts  $i$  and  $j$  mean space and time, respectively.  $\Delta t$  means time resolution of the velocity measurement. To obtain spatio-temporal distribution of shear stress,  $\tau_{r\theta}(r,t)$ ,  $\tau_{wall}$  and  $u_{\theta}(r,t)$  are substituted to momentum conservation law, which is described as

$$\rho \frac{\partial u_{\theta}}{\partial t} = \frac{2\tau_{r\theta}}{r} + \frac{\partial \tau_{r\theta}}{\partial r}. \quad (4.12)$$

Because the left hand side of Eq. (4.12) is given by  $u_{\theta}(r,t)$ ,  $\tau_{r\theta}(r,t)$  is derived as a numerical solution of differential equation. Boundary condition of the differential equation is given by  $\tau_{wall}$ . Then shear rate, strain and shear stress are obtained as a form of spatio-temporal distribution. Flow surface,  $\tau(\dot{\gamma}, \gamma)$ , is derived as a relation among these three quantities. To solve the momentum conservation numerically, velocity distribution near the inner cylinder is required. In the analysis below, therefore, velocity distribution obtained by PTV was used. The analysis above is applicable to velocity distribution measured by UVP, if velocity near the inner cylinder is accurately measured by improving the experimental apparatus.

##### 4.4.2 The obtained shear stress and quantified viscoelasticity

Shear rate distributions obtained from the measured velocity distribution with Eq. (4.10) is shown in Fig. 4.7 (a) and (b). In Fig. 4.7 (a), the shear rate increases in almost all spatial positions, and decrease very little. In Fig. 4.7 (b), on the other hand, the shear rate has local minimum at around  $t = 1.0$  s. Shear rate varies oscillatory around this moment. It is expected that stress response to the oscillatory variation of shear stress

will be obtained in flow surface. Figure 4.7 (c) and (d) show the shear stress distributions obtained by solving Eq. (4.12) with the experimentally obtained spatio-temporal velocity distributions. According to Fig. 4.6 and Eq. (4.9), shear stress distribution is determined from boundary condition,  $\tau_{\text{wall}}$ , and local acceleration of fluid. Integral effect of viscoelasticity appears in the time variation of  $\tau_{\text{wall}}$  as Fig. 4.5 (b) and it decreases after the maximum point. Thus shear stress decreases in a wide range at around  $t = 4.0$  s. Characteristics of viscoelasticity in the velocity distribution is the deceleration at around  $t = 1.0$  s as Fig. 4.5 (f) shows. Considering momentum conservation described as Eq. (4.12), fluids are decelerated when the shear stress takes larger value in outer region. Typical instantaneous shear stress profiles are shown in Fig. 4.8; these are extracted from the area bounded by dashed line in Fig. 4.7 (d). At  $t = 0.4$  s, shear stress has local maximum at  $r = 40$  mm, thus the PAA solution is decelerated at this moment. It means that velocity information of Fig. 4.5 (f) is correctly reflected in the derived shear stress field of Fig. 4.7 (d). Shear stress distribution converges to the analytical solution under the steady state depicted by solid line in Fig. 4.8 as time advances.

Figure 4.9 shows relationships among shear rate, strain and shear stress, named flow surface in this paper. Figure 4.9 (a) is a flow surface of the silicone oil. Shear stress depends only on shear rate, which means that the silicone oil can be regarded as a Newtonian fluid as know so. The relation between shear rate and shear stress follows a flow curve of Newtonian fluid with viscosity of 0.97 Pa·s. Figure 4.9 (b) is a flow surface of the PAA solution. It seems that the data point is much coarser for the shear rate direction in Fig. 4.9 (b) compared with Fig. 4.9 (a). This is because data points are concentrated in low shear rate region in Fig. 4.9 (b). In the flow of PAA solution, high shear rate appears only near the inner cylinder, and shear rate is small in wide region, as Fig. 4.7 (b) shows. Because the shear rate distribution is expressed with uniform spatial resolution, data points are dense in low shear rate. Viscoelasticity of the fluid is expressed as a ridge of the flow surface. In Fig. 4.9 (c), the flow surface is depicted from a different viewpoint, and the ridge is circled by dashed line. The ridge separates the flow surface into two regions, elastic region and viscous region. In the region of small strain, shear stress increases as strain increases. This region shows elasticity of the PAA solution, because elasticity means that stress of materials depends on strain. In the region of large strain, on the other hand, shear stress increases as shear rate increases. Thus this region is regarded as viscous region. In flow field, the viscous region corresponds to steady state where the flow is governed by shear-rate-dependent viscosity. The flow surface in the viscous region equals to ordinal flow curves. Figure

4.9 focuses on small strain region of the flow surface. It shows the relation between shear rate, strain and shear stress while the PAA solution oscillates right after the inner cylinder starts rotation. Dots representing individual data points trace circular patterns in Fig. 4.9 (d), because the fluid experiences oscillatory variation of the three quantities. In measurements of linear viscoelasticity with commercial rheometers, periodic variation of strain is applied to the test material. Fig. 4.9 (d) shows that test fluids experience similar deformation to the linear viscoelasticity test. Therefore, it will be possible to derive storage modulus  $G'$  and loss modulus  $G''$  by analyzing the oscillatory variation of quantities.

The flow surface in Fig. 4.9 (b) contains information about viscoelasticity of the test fluid. With knowledge of rheology, it is possible to read out viscoelastic characteristics of the test fluid from the shape of the flow surface such as the ridge between elastic and viscous regime. Additional analysis of the flow surface will enable to derive rheological properties such as  $G'$ ,  $G''$  and relaxation time. To predict flow by numerical simulations, one of the way is to determine constants in rheological models with the experimental information as already succeeded for shear-rate-dependent viscosity. We propose, however, to directly refer the flow surface in flow simulations. Then it is not necessary to construct or find proper, suitable rheological models. In the next chapter, flow simulation by introducing the flow surface is briefly presented as an example of practical use of the flow surface.

#### 4.4.3 Error propagation and measurement limitation

Because the procedure to obtain flow surface contains the calculations of spatial gradient, time integral and spatial integral, measurement errors on velocity  $u_\theta$ , position  $r$  and shear stress  $\tau_{wall}$  propagate through the calculations. The effect of the measurement errors on the derived quantities is assessed in this section. Because the effect on shear rate is already discussed in Chapter 3, here the effect on strain and shear stress is assessed.

The error propagation is assessed in the same way as the way introduced in Chapters 2 and 3: When a quantity  $y$  is derived from experimentally measured quantities  $x_l$  as

$$y = f(x_1, x_2, x_3, \dots, x_l, \dots, x_M), \quad (4.13)$$

measurement error on  $y$ ,  $\delta y$ , is described as following

$$\delta y = \pm \sqrt{\sum_{l=1}^M \left( \frac{\partial f}{\partial x_l} \delta x_l \right)^2}, \quad (4.14)$$

where  $\delta x_l$  are errors on the measured quantities  $x_l$ . In the procedure presented in Section 4.4.1, strain and shear stress are described as

$$\gamma_{i,j} = \sum_{p=0}^j \left( \frac{u_{i+1,p} - u_{i-1,p}}{2\Delta r} - \frac{u_{i,p}}{r_i} \right) \Delta t, \quad (4.15)$$

$$\tau_{i,j} = \frac{r_i}{r_i + 2\Delta r} \left( \tau_{i-1,j} + \rho \frac{u_{i,j} - u_{i,j-1}}{\Delta t} \Delta r \right), \quad (4.16)$$

where  $\Delta r$  is spatial resolution on  $r$  axis,  $\Delta t$  is time resolution, and the suffixes  $i$  and  $j$  indicate the position and time in discretized form. Because velocities,  $u_{i+1,p}$ ,  $u_{i,p}$  and  $u_{i-1,p}$ , and radial position,  $r_i$ , are expected to include measurement errors in Eq. (4.15), measurement error on strain,  $\delta\gamma$ , is described as

$$\delta\gamma_{i,j} = \pm \sqrt{\sum_{p=0}^j \left[ \left( \frac{\partial\gamma_{i,p}}{\partial u_{i+1,p}} \delta u \right)^2 + \left( \frac{\partial\gamma_{i,p}}{\partial u_{i-1,p}} \delta u \right)^2 + \left( \frac{\partial\gamma_{i,p}}{\partial u_{i,p}} \delta u \right)^2 \right] + \left( \frac{\partial\gamma_{i,j}}{\partial r_i} \delta r \right)^2}, \quad (4.17)$$

where  $\delta u$  and  $\delta r$  mean measurement errors on  $u_\theta$  and  $r$ , respectively. By calculating partial differentials and the summation,  $\Sigma$ , Eq. (4.17) is converted to

$$\delta\gamma_{i,j} = \pm \sqrt{(j+1) \left[ \frac{1}{2(\Delta r)^2} + \frac{1}{r_i^2} \right] (\Delta t \delta u)^2 + \left( \frac{\Delta t}{r_i^2} \sum_{p=0}^j u_{i,p} \right)^2 (\delta r)^2}. \quad (4.18)$$

Shear stress at an arbitrary data point is determined by velocity distribution between the inner cylinder and the data point as shear stress is described as recurrence relation in Eq. (4.16). To assess the error propagation, therefore, error on shear stress is described as a function of velocity information between the inner cylinder and the data point,

$$\delta\tau_{i,j} = \pm \sqrt{\sum_{p=1}^i \left( \frac{\partial\tau_{i,j}}{\partial u_{p,j}} \delta u \right)^2 + \sum_{p=1}^i \left( \frac{\partial\tau_{i,j}}{\partial u_{p,j-1}} \delta u \right)^2 + \sum_{p=1}^i \left( \frac{\partial\tau_{i,j}}{\partial r_p} \delta r \right)^2 + \left( \frac{\partial\tau_{i,j}}{\partial \tau_{0,j}} \delta\tau_{wall} \right)^2}, \quad (4.19)$$

where  $\delta\tau_{wall}$  means measurement error on shear stress on the inner cylinder wall. Equation (4.19) is converted to

$$\delta\tau_{i,j} = \pm \sqrt{2 \left( \rho \frac{\Delta r}{\Delta t} \delta u \right)^2 \sum_{p=0}^i \left( \prod_{q=p}^i \frac{r_q}{r_q + \Delta r} \right)^2 + \left[ \rho \frac{(\Delta r)^2}{\Delta t} \delta r \right]^2 \sum_{p=0}^i \left[ \frac{u_{p,j} - u_{p,j-1}}{(r_p + \Delta r)^2} \left( \prod_{q=p+1}^i \frac{r_q}{r_q + \Delta r} \right) \right]^2 + \left[ \delta\tau_{wall} \left( \prod_{q=1}^i \frac{r_q}{r_q + \Delta r} \right) \right]^2} \quad (4.20)$$

by calculating partial differentials and summation. According to Eq. (4.18), the error on strain  $\delta\gamma$  increases as time advances as the term  $j+1$  and the summation for  $j$  implies. This error accumulation is caused by the integration of shear rate for time direction as

Eq. (4.11) shows in discretized form. On the other hand, the error on shear stress,  $\delta\tau$ , increases as  $r$  increases because of the summation  $\Sigma$  and the product of sequence  $\Pi$  for radial direction.

In Fig. 4.10, the errors,  $\delta\gamma$  and  $\delta\tau$ , are displayed together with strain and shear stress derived from the velocity profile. Strain and shear stress of the PAA solution are displayed with  $\delta\gamma$  and  $\delta\tau$  because error propagation in the case of viscoelastic fluid is object of interest from a viewpoint of rheometry. The errors after the propagation,  $\delta\gamma$  and  $\delta\tau$ , are derived by Eqs. (4.18) and (4.20), respectively. Errors before the propagation,  $\delta u$ ,  $\delta r$  and  $\delta\tau_{wall}$ , are assumed to be 9.3 mm/s, 0.075 mm and 0.10 Pa, respectively. The assumed value of  $\delta u$  is velocity resolution of PTV which corresponds to 1 pixel/frame. As the value of  $\delta r$ , spatial resolution of the images recorded by the high speed video camera is employed. The value of  $\delta\tau_{wall}$  is the corresponding shear stress to the resolution of the torque sensor. Figure 4.10 (a) shows strain  $\gamma$  obtained from the velocity profile, with the estimated error  $\delta\gamma$ . Because  $\delta\gamma$  increases as time advances, time  $t$  is chosen as the horizontal axis of Fig. 4.10 (a). The time variation of strain is extracted from  $r = 21$  mm where the fluid is largely deformed and the velocity measurement is not affected by light reflection on the inner cylinder. It is shown that  $\delta\gamma$  is relatively small compared with  $\gamma$ . Both  $\gamma$  and  $\delta\gamma$  increase as time advances, and accordingly the ratio  $\delta\gamma/\gamma$  decreases. Figure 4.10 (b) shows shear stress distribution and the estimated error  $\delta\tau$  at  $t = 12$  s which is regarded as steady state. The amplitude of  $\delta\tau$  is larger in outer region because of the accumulation of measurement errors through the spatial integration described as Eq. (4.16). As shear stress decreases as  $r$  increases, ratio of  $\delta\tau$  to  $\tau$  is significantly large near the outer cylinder.

As described in Section 4.2, the flow between the cylinders is assumed to be one-directional in the analysis to obtain shear stress distribution. One of the requirement to make the flow one-dimensional is that Reynolds number is small enough. This limitation is already considered in Section 3.2.2. In cases that viscoelasticity is taken into account, the possibility that radial or axial flow is caused by viscoelasticity have to be examined. To assess the effect of viscoelasticity, Deborah number  $De$  have been employed. In flows between concentric cylinders, Deborah number is defined as

$$De = \frac{\lambda U_{wall}}{r_{out} - r_{in}}, \quad (4.21)$$

where  $\lambda$  means relaxation time of the fluid. For Maxwell fluids, the relaxation time corresponds to the inverse of frequency where  $G'$  equals  $G''$ . Thus relaxation time of the PAA solution is estimated as tens or hundreds second. Then Deborah number of the flow shown in Fig. 4.5 (d) and (f), the flow of the PAA solution between the cylinders,

would be between 5.0 and 50. According to a previous research [16], critical Deborah number  $De_c$  where secondary flow occurs is estimated to be less than 19. It is preferred that  $De$  is reduced by slowing down the rotation of the inner cylinder. In the present experiment, the motor connected to the inner cylinder could not slow down the rotation any more. It is possible to make Deborah number less than  $De_c$  by improving the experimental apparatus. According to velocity vector distribution obtained by PTV, the magnitude of  $u_r$  is about 10% of  $u_\theta$ .

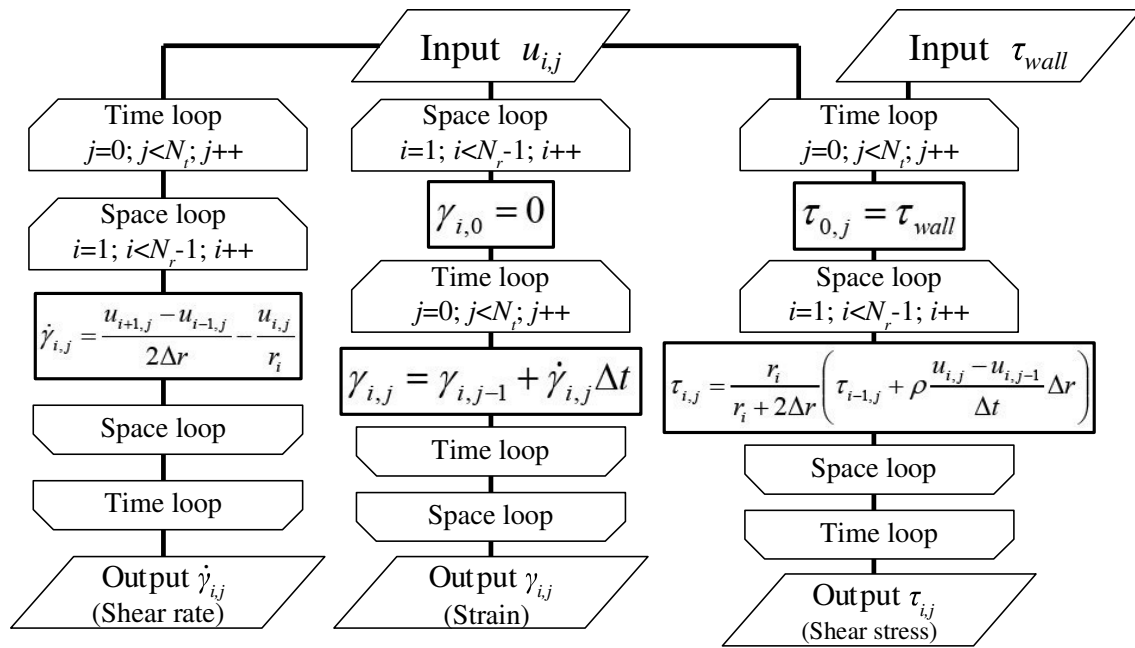


**Figure 4.6** Procedure to obtain the relation among shear rate, strain and stress from experimentally obtained velocity distribution and shear stress on the wall

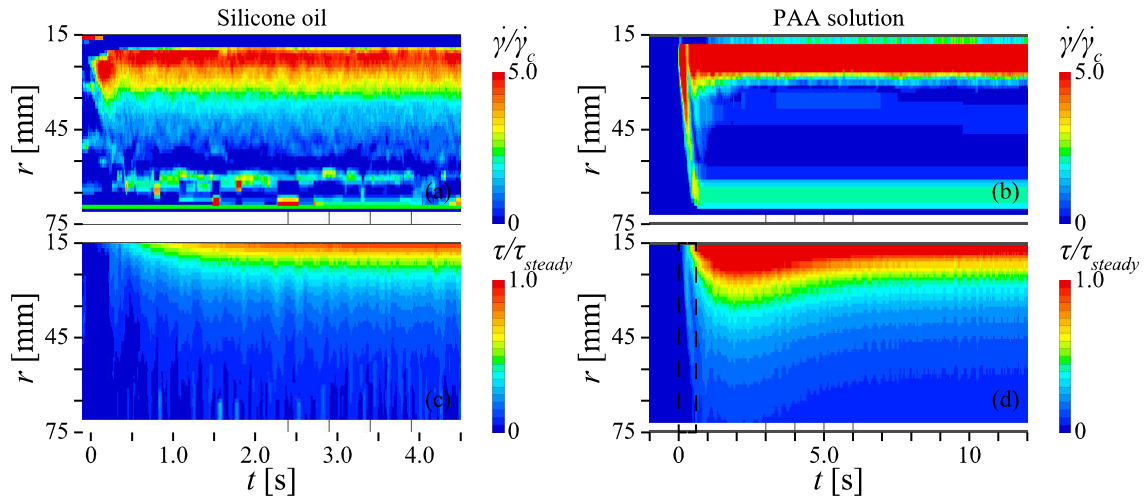


**Figure 4.7** Suptio-temporal distributions of (a)-(b) shear rate and (c)-(d) shear stress obtained from experimental data for silicone oil (left panels) and PAA solution (right panels)

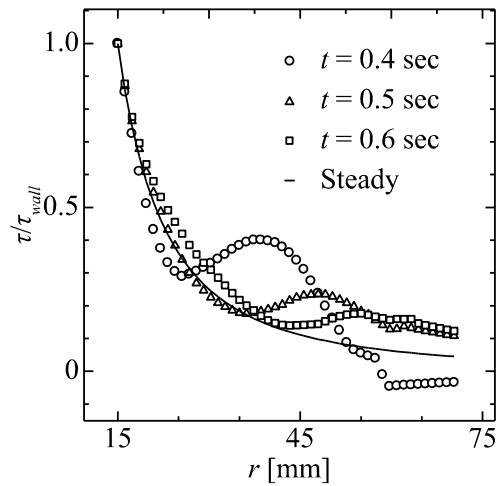


**Figure 4.8** Instantaneous shear stress profiles normalized by wall shear stress at each time extracted from Fig. 4.7(d) indicated by dashed rectangle

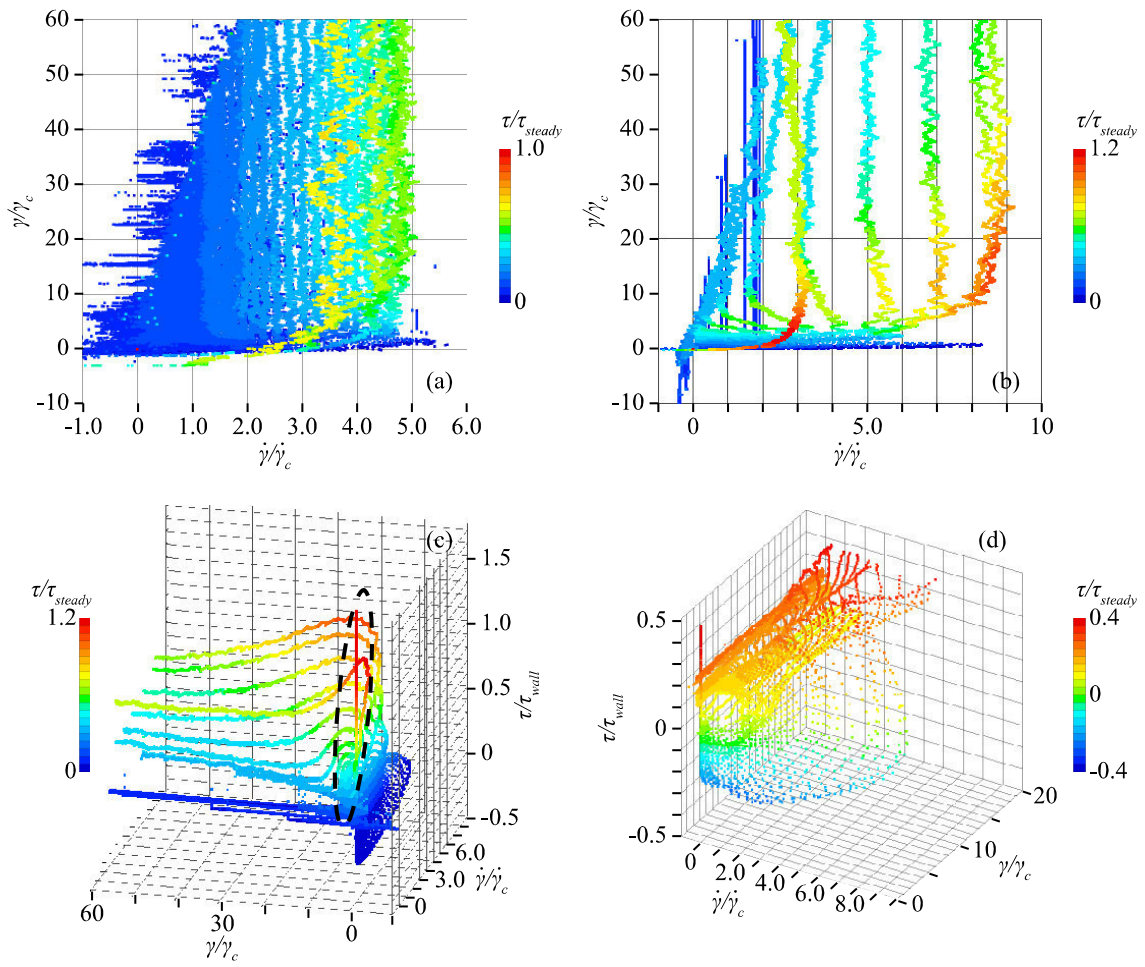


**Figure 4.9** Relation among shear rate, strain and shear stress for (a) silicone oil and (b)-(d) PAA solution from different viewpoints

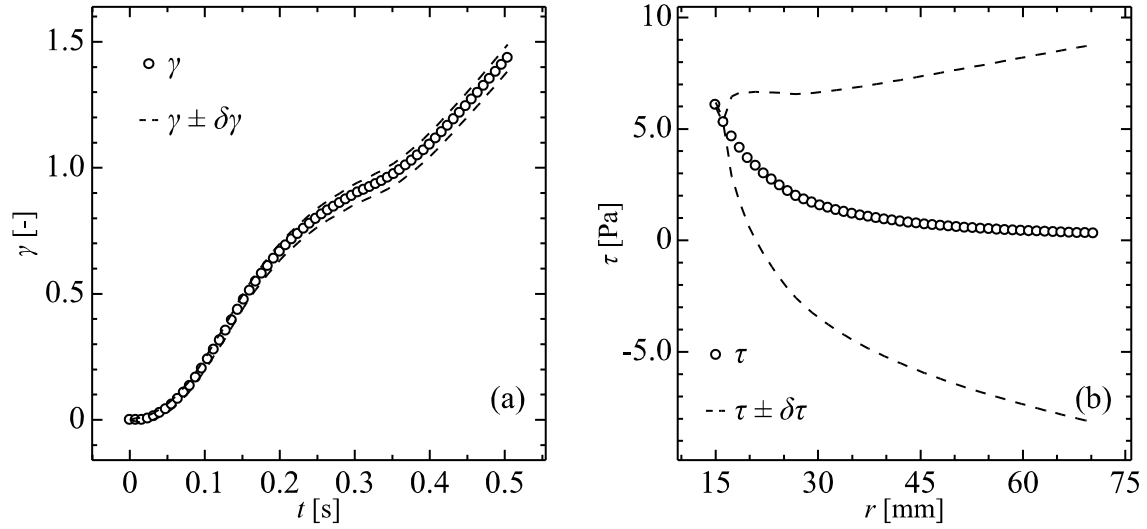


**Figure 4.10** Relation among shear rate, strain and shear stress for (a) silicone oil and (b)-(d) PAA solution from different viewpoints

#### 4.5 Application to numerical simulations

##### 4.5.1 Procedure of the numerical simulation

As a configuration of flow simulation with the flow surface, concentric cylinder with the same size as Fig. 4.2 was employed. Under the assumption that radial and axial velocity component,  $u_r$  and  $u_z$ , are zero, momentum conservation law described as Eq. (4.12) was solved. Velocity of the inner cylinder wall  $U_{wall}$  was set as 3.11 mm/s, which is one tenth of the velocity in the experiment. The flow surface obtained by the experiment does not have any information in the higher shear rate and strain region than experimentally realized value. Thus the wall velocity was set smaller than experimental condition to keep shear rate and strain in the range of the flow surface. This configuration was employed as the easiest example to simulate flow field. The simulation was performed for both of the test fluids, the silicone oil and the PAA solution. Time and spatial resolutions for each flow simulation are summarized in Table 4.1. In the flow simulation of Newtonian fluids, the resolutions should be set to make diffusion number,  $di$ , less than 0.5. That is described as

$$di = \frac{\eta \Delta t}{\rho (\Delta r)^2}, \quad (4.22)$$

where  $\Delta t$  and  $\Delta r$  mean time and spatial resolution, respectively. Since viscosity  $\eta$  depends on shear rate and strain in the simulation with the flow surface, it is difficult to estimate  $di$  before doing the simulation. Thus there is a possibility that the time resolutions in Table 4.1 are not high enough to satisfy the condition,  $di < 0.5$ . Grid points to calculate the velocity and these to calculate the shear rate were arranged as

spatially staggered grid. Strain and shear stress are calculated on the same grid as shear rate.

The procedure to simulate a flow with the flow surface is summarized in Fig. 4.11. As the first operation of the simulation,  $U_{wall}$  is substituted as boundary condition. Then the fluid near the inner cylinder experiences shear deformation. Shear rate of the fluid  $\dot{\gamma}_{i,j}$  is derived by

$$\dot{\gamma}_{i,j} = \frac{u_{i+0.5,j} - u_{i-0.5,j}}{r_{i+0.5} - r_{i-0.5}} - \frac{u_{i+0.5,j} - u_{i-0.5,j}}{2r_i}, \quad (4.23)$$

where 0.5 in subscript means that neighbor point of the staggered grid is referred. Strain  $\gamma_{i,j}$  is obtained by integrating shear rate as Eq. (4.11) describes. Here, two quantities required to determine shear stress are obtained. To include the flow surface to the simulation, an algorithm to output shear stress for the input of shear rate and strain is required. The algorithm used in this case is explained in Section 4.5.2. In this paper, degree of sophistication of the algorithm is out of focus. The algorithm gives spatial distribution of shear stress  $\tau_{i,j}$ , thus velocity in the next time step is calculated from shear stress gradient by

$$u_{i,j+1} = u_{i,j} + \frac{\Delta t}{\rho} \left( \frac{\tau_{i+0.5,j} + \tau_{i-0.5,j}}{r_i} - \frac{\tau_{i+0.5,j} - \tau_{i-0.5,j}}{r_{i+0.5} - r_{i-0.5}} \right). \quad (4.24)$$

By iterating the procedure, flow field is simulated while introducing the flow surface instead of constitutive equation used in common simulations.

**Table 4.1** Spatial and time resolutions for each fluid simulations

	Silicone oil	PAA solution
Spatial resolution $\Delta r$	1.0 mm	1.0 mm
Time resolution $\Delta t$	80 $\mu$ s	8.0 $\mu$ s

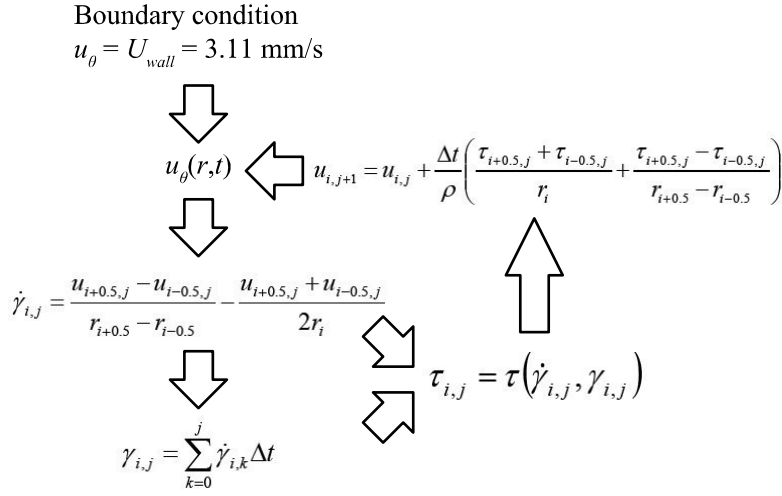


**Figure 4.11** Procedure of the numerical simulation with the flow surface

#### 4.5.2 Interpolation of the discretized relation to determine shear stress

In the procedure of numerical simulations in Fig. 4.11, shear stress have to be extracted from the flow surface to arbitrary inputs of shear rate and strain. Thus an algorithm to interpolate the discretized flow surface, Fig. 4.9 (a) and (b), is required.

Firstly, data points near the input value of shear rate and strain are extracted from the discretized flow surface. All of the data points in the flow surface are sorted by a distance from the input value

$$D_i = \sqrt{(\gamma_i - \gamma_{input})^2 + c^2(\dot{\gamma}_i - \dot{\gamma}_{input})^2}, \quad (4.25)$$

where subscripts  $i$  and  $input$  mean value of  $i$ th data point and input value, respectively. The weight coefficient,  $c$  in Eq. (4.25), was set as 40 s and 4.3 s for the silicone oil and the PAA solution, respectively. According to the sort,  $N$  data points with small  $D_i$  are extracted.  $N$  was set as 10 for both fluids.

Secondly, output shear stress is determined by assuming linearity around the input shear rate and strain. Namely, output shear stress  $\tau_{output}$  is described as

$$\tau_{output} = A\gamma_{input} + B\dot{\gamma}_{input}. \quad (4.26)$$

Coefficients  $A$  and  $B$  are determined to minimize accumulated square error of shear stress between Eq. (4.26) and the extracted  $N$  data points. To confirm whether the interpolation property works or not, flow surfaces reconstructed by the interpolation algorithm are presented as Fig. 4.12 (a) and (b). In Fig. 4.12 (a), the flow surface of the silicone oil, shear stress depends on shear rate, and is almost independent on strain. In Fig. 4.12 (b), on the other hand, the ridge remains at around  $\dot{\gamma}\gamma_c = 10$ . Shear stress

depends on strain in  $\dot{\gamma}\gamma_c < 10$ , and also depends on shear rate in  $\dot{\gamma}\gamma_c > 10$ . Thus it is expected that the interpolation can provide viscoelastic property to the numerical simulation from the original flow surface of Fig. 4.9 (b).

Although Eq. (4.26) is introduced to interpolate discrete data points linearly, it has the same form as the equation which describes dynamic viscoelasticity test with conventional rheometer,

$$\tau = G' \gamma + \frac{G''}{2\pi f} \dot{\gamma}. \quad (4.27)$$

Here, it is considered whether the flow surface in Fig. 4.9 is consistent with the rheological properties in Fig. 4.4 (b) obtained in the dynamic viscoelasticity test. Because the flow surface of the PAA solution represents viscoelasticity while the strain is small, There is a possibility that the coefficients  $A$  and  $B$  corresponds  $G''/(2\pi f)$  and  $G'$ , respectively, in the region where strain is small. Figure 4.13 shows the coefficients  $A$  and  $B$  depending on shear rate and shear stress. The values of coefficients in Fig. 4.13 are obtained on the procedure to derive Fig. 4.12. In Newtonian case, the coefficient  $A$  partly succeeds in representing fluid property. In the region indicated by (I) and (II) in Fig. 4.13 (a), value of  $A$  is around 0.97 Pa·s, which is viscosity of the silicone oil. In other regions, however,  $A$  is significantly larger or smaller than the reference viscosity. Because of measurement errors on velocity and shear stress, it is difficult to obtain the precise viscosity from a local relation among  $\dot{\gamma}$ ,  $\gamma$  and  $\tau$ . In Fig. 4.13 (d), which shows elastic coefficient of PAA solution, the coefficient  $B$  has large value in the region indicated as (III). This tendency is consistent with the fact that the PAA solution behaves as viscoelastic fluid when strain is small. In this region, the value of  $B$  is between 1.0 Pa and 5.0 Pa. This value equals to  $G'$  under low frequency ( $f = 0.05$  Hz), according to Fig. 4.4 (b).

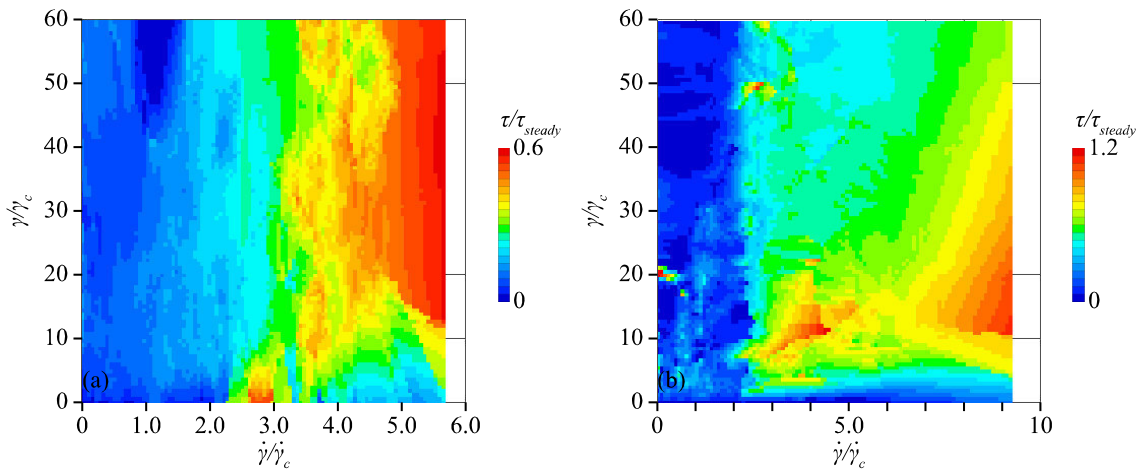


**Figure 4.12** Shear stress as a function of shear rate and strain of (a) silicone oil and (b) PAA solution

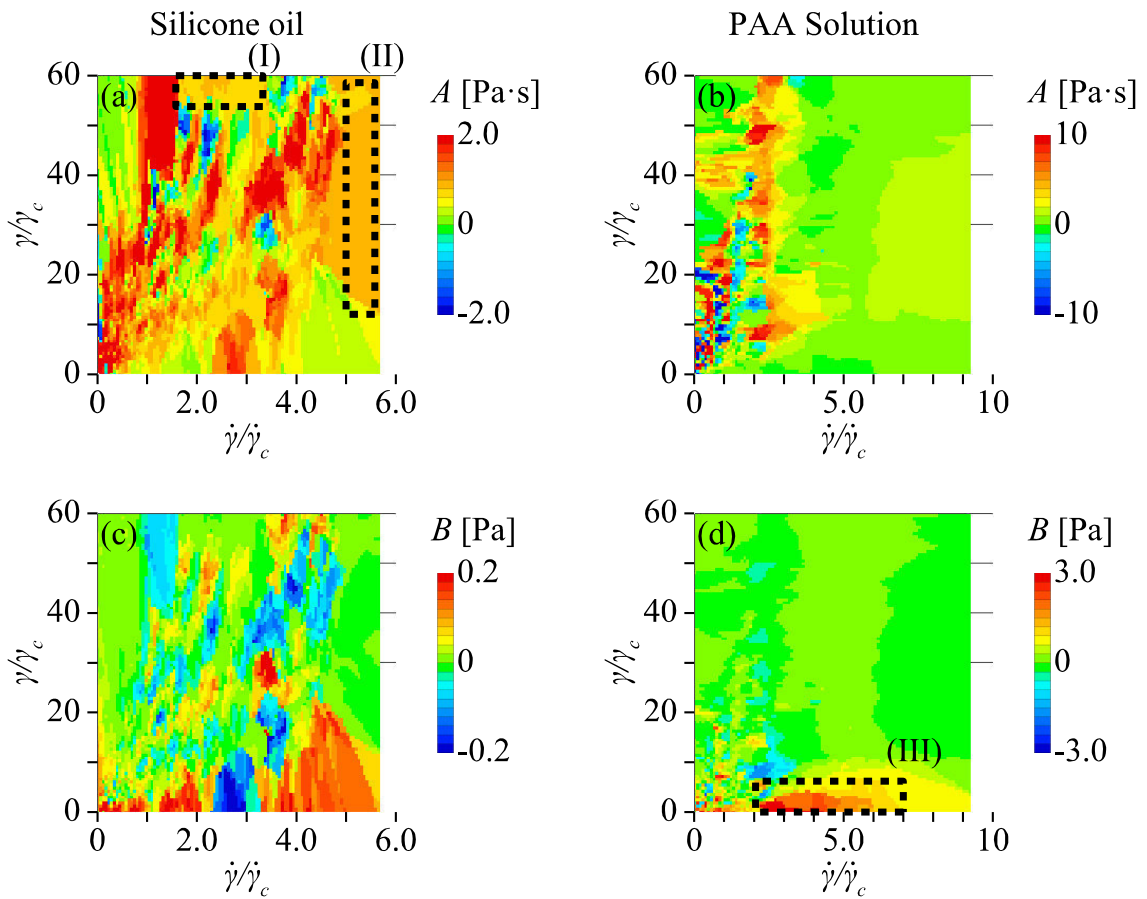


**Figure 4.13** (a), (b) Viscous and (c), (d) elastic coefficients defined by Eq. (4.26) to interpolate the discretized relation among shear rate, strain and shear stress for silicone oil (left panel) and PAA solution (right panel)

### 4.5.3 Spatio-temporal velocity distribution obtained by the simulation

Figure 4.14 shows velocity, shear rate and shear stress distribution as a solution of the simulation. In Fig. 4.14 (a), velocity distribution of the silicone oil, velocity diffuses from the inner cylinder after the inner cylinder starts rotation at  $t = 0$ . The velocity slightly decreases at around  $t = 3.0$  s. In the velocity distribution of the PAA solution shown in Fig. 4.14 (b), on the other hand, the fluid is driven in a wide range after the rotation starts. At  $t = 1.5$  s, the fluid even near the outer cylinder has considerable value of the velocity. Deceleration begins at the same time, and fluid only near the inner cylinder flows in the steady state. The same tendency was observed in the experimental velocity distribution of the PAA solution shown in Fig. 4.5 (f). Figure 4.14 (a) and (b) mean that the flow surfaces of each fluid provide certain Newtonian and viscoelastic property to the simulation, thus the difference of the properties appears on the velocity distributions. Of course there are a lot of differences between the experimental and simulated velocity distributions. For example, velocity fluctuation was observed in the experiment, but it does not appear in the result of the simulation. While the velocity fluctuations, shear stress is described as multiple-value function of shear rate and shear stress: Two or more values of shear stress is given for one set of shear rate and strain. The velocity fluctuation did not appear because the multiple-value function was not taken into account in the simulation. One of ways to improve the simulation is to introduce hysteresis to determine one value from the multiple-value of shear stress. Although the simulation still has a margin for improvement, Fig. 4.14 is enough to show applicability of the flow surface to predict flows of non-Newtonian fluids without introducing any rheological models.

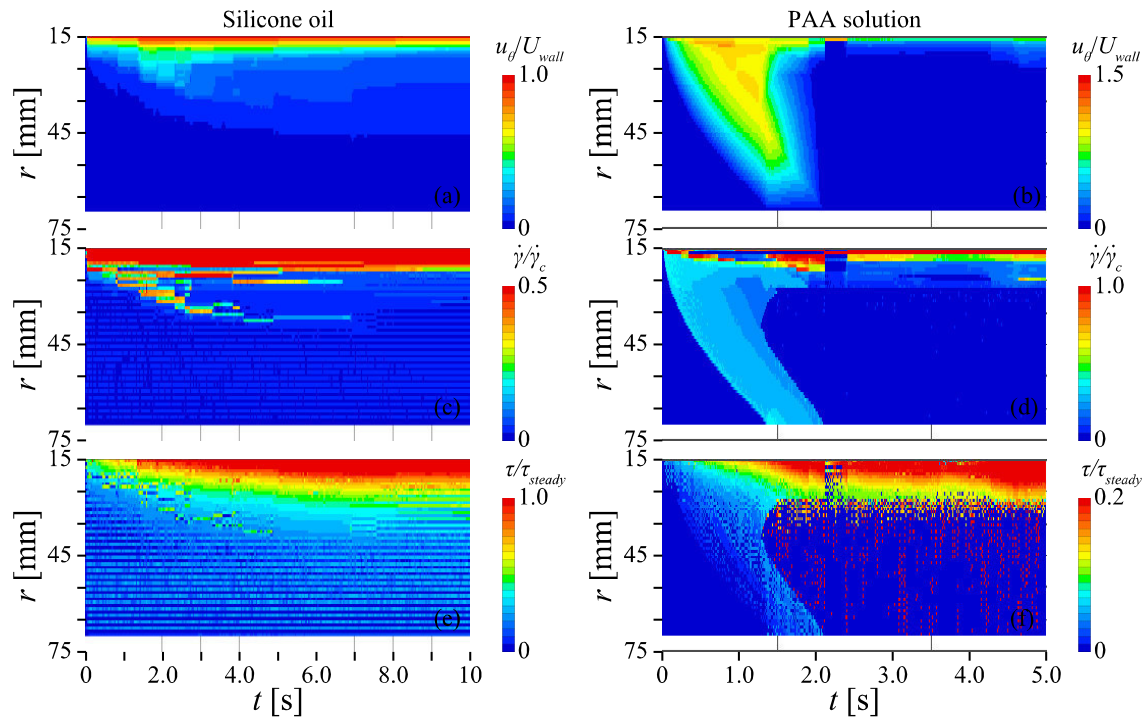


**Figure 4.14** Distributions of (a)-(b) velocity, (c)-(d) shear rate and (e)-(f) shear stress obtained by a simulation with experimental property shown in Fig. 4.8 for silicone oil (left panels) and PAA solution (right panels)

#### 4.6 Conclusion

Characterization method for viscoelastic fluids based on fluid velocimetry was proposed. In the presented method, viscoelasticity of fluids are characterized as the relationship among shear rate, strain and shear stress. Shear rate and strain are derived as spatio-temporal distribution from velocity distribution, and shear stress distribution is obtained as a solution of momentum conservation law. To realize this characterization, concentric cylinders with a large gap was introduced as a flow configuration because momentum conservation law can be solved by substituting obtained velocity distribution and torque to rotate the inner cylinder. The relation among the three quantities was named “flow surface” after “flow curve” which means the relation between shear rate and shear stress. As a test of the characterization, properties of silicone oil and polyacrylamide (PAA) solution were examined. These two fluids represents Newtonian fluid and viscoelastic fluid, respectively. As velocimetry, particle tracking velocimetry (PTV) and ultrasonic velocity profiling (UVP) were employed.

According to velocity distributions obtained with PTV and UVP, velocity diffuses from the inner cylinder after the inner cylinder start rotating in the silicone oil flow, and converges to a steady state. In the flow of the PAA solution, on the other hand,

oscillation of the fluid was observed. Because there is a significant difference between the two cases, the velocity and torque obtained in the experiment contains enough information to characterize the two test fluids. The experimental conditions, such as size of cylinders and rotational speed of the inner cylinder, are well adjusted to induce the viscoelastic flow. In the derivation of shear stress field and flow surface below, velocity measured with PTV was employed because velocity information near the inner cylinder is required to solve momentum conservation. Viscoelasticity of the PAA solution appeared in the shear stress distribution as well. Local maximum was observed in simultaneous shear stress profile at the moment when the viscoelastic fluid is decelerated. The local maximum means that the momentum conservation law was properly solved, and the deceleration of velocity effected on the stress as gradient of shear stress.

The obtained shear rate, strain and shear stress were displayed as a form of the relation among the three quantities, namely flow surface. In the flow surface, elastic and viscous natures of the fluid were expressed: elastic nature was expressed as shear stress increasing as strain increases, and viscous nature was expressed as shear stress increasing as shear rate increases. The periodic variation of three quantities while the fluid oscillation corresponds to circular trajectory of data points in the flow surface. Because the similar variation of quantities is applied for fluids in linear viscoelasticity test, the flow surface contains parameters such as storage modulus  $G'$  and loss modulus  $G''$ . A numerical simulation was performed by introducing the flow surface as a trial of practical utilization. The simulation succeeded in the qualitative reconstruction of flow behavior with increase and decrease of velocity. The result of simulation confirms that the flow surface contains information about viscoelasticity of the test fluid.

As viscoelastic materials are utilized in various industrial fields, rheological models and determination method of their model constants, rheometry, have been developed in each field. Thus rheology is bifurcating to several particular fields such as biorheology, food rheology and polymer rheology. As the characterization presented in this paper is applicable for all materials which is regarded as continuum, the technique can be utilized in wide industrial fields. Our technique would be a powerful tool to characterize materials whose rheological model is not established yet. Although PTV was employed as velocimetry in this paper, the procedure to characterize fluids with a flow surface does not limit velocimetry. By introducing ultrasonic techniques such as UVP, therefore, even opaque fluids can be characterized with flow surface.

## References

- [1] C. Tzoumanekas, D.N. Theodorou, From atomistic simulations to slip-link models of entangled polymer melts: Hierarchical strategies for the prediction of rheological properties, *Current Opinion in Solid State and Materials Science* 10 (2006) 61-72
- [2] J.T. Padding, W.J. Briels, Systematic coarse-graining of the dynamics of entangled polymer melts: the road from chemistry to rheology, *J. Phys. Condens. Matter* 23 (2011) 233101
- [3] Y. Li, B.C. Abberton, M. Kröger, W.K. Liu, Challenges in Multiscale Modeling of Polymer Dynamics, *Polymers* 5 (2013) 751-832
- [4] F. Rodríguez-González, J. Pérez-González, L. Vargas, B.M. Marín-Santibáñez, Rheo-PIV analysis of the slip flow of a metallocene linear low-density polyethylene melt, *Rheol Acta* 49 (2010) 145-154
- [5] F. Blanc, F. Peters, E. Lemaire, Particle Image Velocimetry in Concentrated Suspensions: Application to Local Rheometry, *Appl. Rheol.* 21 (2011) 23735
- [6] C.J. Dimitriou, L. Casanellas, T.J. Ober, G.H. McKinley, Rheo-PIV of a shear-banding wormlike micellar solution under large amplitude oscillatory shear, *Rheol Acta* 51 (2012) 395-411
- [7] J. Pérez-González, J.J. López-Durán, B.M. Marín-Santibáñez, F. Rodríguez-González, Rheo-PIV of a yield-stress fluid in a capillary with slip at the wall, *Rheol Acta* 51 (2012) 937-946
- [8] J.J. López-Durán, J. Pérez-González, B.M. Marín-Santibáñez, F. Rodríguez-González, A New method to determine the yield stress of a fluid from velocity profiles in a capillary, *Revista Mexicana de Ingeniería Química* 12 (2013) 121-128
- [9] Th. Wunderlich, P.O. Brunn, Ultrasound pulse Doppler method as a viscometer for process monitoring, *Flow Measurement Instrumentation* 10 (1999) 201-205
- [10] N. Dogan, M.J. McCarthy, R.L. Powell, In-Line Measurement of Rheological Parameters and Modeling of Apparent Wall Slip in Diced Tomato Suspensions Using Ultrasonics, *J. Food Science*, 67 (2002) 2235-2240
- [11] B. Ouriev, E. Windhab, Novel ultrasound based time averaged flow mapping method for die entry visualization in flow of highly concentrated shear-thinning and shear-thickening suspensions, *Meas. Sci. Technol.* 14 (2003) 140-147
- [12] J.A. Wiklund, M. Standing, A.J. Pettersson, A. Rasmuson, A Comparative Study of UVP and LDA Techniques for Pulp Suspensions in Pipe Flow, *AIChE J.* 52 (2006) 484-495

- [13] B. Derakhshandeh, D. Vlassopoulos, S.G. Hatzikiriakos, Thixotropy, yielding and ultrasonic Doppler velocimetry in pulp fibre suspensions, *Rheol Acta* 51 (2012) 201-214
- [14] S.J. Gibbs, K.L. James, L.D. Hall, D.E. Haycock, W.J. Frith, S. Ablett, Rheometry and detection of apparent wall slip for Poiseuille flow of polymer solutions and particulate dispersions by nuclear magnetic resonance velocimetry, *J. Rheol.* 40 (1996) 425-440
- [15] S.J. Gibbs, D.E. Haycock, W.J. Frith, S. Ablett, L.D. Hall, Strategies for Rapid NMR Rheometry by Magnetic Resonance Imaging Velocimetry, *J. Magnetic Resonance* 125 (1997) 43-51
- [16] S. J. Muller, R. G. Larson, E. S. G. Shaqfeh, A purely elastic transition in Taylor-Couette flow, *Rheol Acta* 28 (1989) 499-503

## 5.1 Introduction

Effective viscosity of particle suspensions, which is defined by regarding suspension as one continuum, have been investigated for a long time. The first study about the effective viscosity was performed by Einstein [1] from theoretical aspect. Later Batchelor *et al.* extended the theory to the cases of non-spherical particles [2], with Brownian motion [3] and second order term [4]. These researches succeeded in describing effective viscosity of dilute suspensions as functions of volume fraction of particles. In cases the suspension is dense, it is experimentally clarified that the effective viscosity of suspension exceeds a thousand times of the viscosity of suspending medium [5], and theoretically the effective viscosity approaches infinity as volume fraction approaches the limit of closest packing [6]. According to recent researches, however, effective viscosity of dense suspensions depends on not only volume fraction but also other parameters [7]. For example, previous researches [8,9] indicated that microstructures formed by particles affect shear stress, and consequently, effective viscosity. Thus it is difficult to describe shear stress with a simple function independently from the microstructure.

It is known that particles in turbulent modify vortex structure [10], and effective viscosity is employed as one of interpretation of this phenomenon. Even if the suspension is dilute in bulk, volume fraction of particles can be high locally because of accumulation of particles in turbulence [11,12]. As centrifugal force in vortices accumulate particles, it is expected that the void fraction rises in centers of vortices in case the density of the particle is smaller than that of continuous phase. Thus effective viscosity of dense suspension modifies vortex structure. This hypothesis was originally developed for bubbly flows [13], thus similar phenomenon might occur in suspensions of light particles.

This research aim to measure effective viscosity of suspension with high particle concentration. We presented new rheometry based on interfacial rheometry [14] to measure the effective viscosity. By measuring viscosity of suspension layer on water surface, packing was prevented even in case the suspension is highly concentrated. At the same time, it was enabled to observe particle motion.

## 5.2 Experimental setup

Figure 5.1 and 5.2 show the overview of the experimental apparatus and the detail of the measurement section, respectively. The experimental apparatus consists of shear rheometer (Physica MCR300, Anton Paar GmbH, Graz) and digital video camera (DWF-V500, Sony Corporation, Tokyo) as Fig. 5.1 shows. In the measurement section, a cone and cup are concentrically arranged as Fig. 5.2 (a) shows. The rheometer is connected to the cone to rotate it and record torque and rotational speed. Before the cone is settled, particles (FLO-BEADS CL-2507, Sumitomo Seika Chemicals Co., Ltd., Osaka) are dispersed homogeneously on the free surface. The FLO-BEADS is a spherical particle made of polyethylene. Radii of the cone  $r_{in}$  and the cup  $r_{out}$  are 34 mm and 44 mm, respectively. The vertical position of the cone is determined with normal force sensor in the rheometer so as to attach the top face of the cone with the surface [15]. The particles gather in the gap between the inner cone and the outer wall of the cup while adjusting the position of the cone. Then thin layer of suspension is formed in the gap. By rotating the cone, shear deformation is given to the suspension layer. The experiment is performed in five conditions with different particle concentrations. Figure 5.3 shows the dispersion state of the particles in four different concentration conditions. In another condition, the measurement was performed without particles. The images in Fig. 5.3 were took from the top as Fig. 5.1 shows. The inner cone can be seen in the lower right of the images. The amount of particles is quantified as the areal concentration,  $\alpha$ , which is the ratio of the area occupied by particles to that of the gap between the cone and the wall. The area of the particles is calculated as product of area occupied by one particle and a number of particles detected in the images. The areal concentrations are derived as  $\alpha = 0.76, 0.43, 0.22$  and  $0.20$  for Fig. 5.3 (a), (b), (c) and (d), respectively. In Fig. 5.3 (a) and (b), which show the conditions of high concentration, particles distribute all over the gap. As the arrows in Fig. 5.3 show, a local concentration of particles becomes low at certain position. The particles are driven in the inside of this low concentration region, and not driven in the outer side. In Fig. 5.3 (c) and (d), on the other hand, particles gather near the outer wall, and are not driven by the rotation of the cone.

When the rheometer is utilized as interfacial rheometer in measurements of absorption layers, the measured torque and rotational speed are analysed based on dynamics of transportation on interfaces [16-19]. The property of the target interface is quantified as dependence of interfacial shear stress and interfacial viscosity on shear rate. Because they are quantities to describe two dimensional deformation phenomena of interfaces, interfacial shear stress and interfacial viscosity have dimensions of Pa·m

and Pa·s·m, respectively. Numerical technique to derive them from the measured torque is established [14], and available as a commercialized computer program.

In this research, the measured torque is analysed in a different way from the original interfacial rheometry to characterize the suspension as a layer with finite thickness. The property of the suspension is quantified as shear stress and viscosity which have dimensions of Pa and Pa·s, respectively. As the first step of the analysis, torque contribution from the suspension layer  $T_s$  is obtained from the measured torque  $T$  by removing that from the water under the layer and the cone  $T_w$ , namely

$$T_s = T - T_w. \quad (5.1)$$

As the values of  $T_w$ , the torque values measured in the condition without particles are employed. The torque  $T_s$  is applied to the cone because of shear stress generated by the suspension layer  $\tau$ . As the thickness of the layer corresponds to the particle diameter  $d_p$ , the relationship between  $\tau$  and  $T_s$  is derived as

$$\tau = \frac{T_s}{2\pi r_{in}^2 d_p}. \quad (5.2)$$

Here it is assumed that the suspension forms a layer without the overlap of particles as depicted in Fig. 5.2 (a). This assumption is reasonable because the overlap of particles was not observed in the recorded images except near the outer wall. Even if the overlap occurs and the thickness of the layer becomes twice or third times of the particle diameter, the effect to the torque and shear stress is relatively small because the torque varies over some orders depending on applied shear rate, as shown later. Shear rate applied by the cone is derived from the rotational speed of the cone  $\omega$  as

$$\dot{\gamma} = r_{in} \omega \left( \frac{1}{r_{out} - r_{in}} - \frac{1}{r_{out} + r_{in}} \right). \quad (5.3)$$

In the derivation of Eq. (5.3), the flow between the cone and the cup is regarded as Couette flow. Thus  $\dot{\gamma}$  corresponds to shear rate applied to whole of the fluid in the gap. As shear stress and shear rate are derived by Eq. (5.2) and (5.3), respectively, the relationship between them, namely flow curve, can be drawn. Viscosity of the suspension is obtained by

$$\eta = \frac{\tau}{\dot{\gamma}}. \quad (5.4)$$

Thus dependence of viscosity on shear rate can also be drawn from the measured torque and rotational speed.

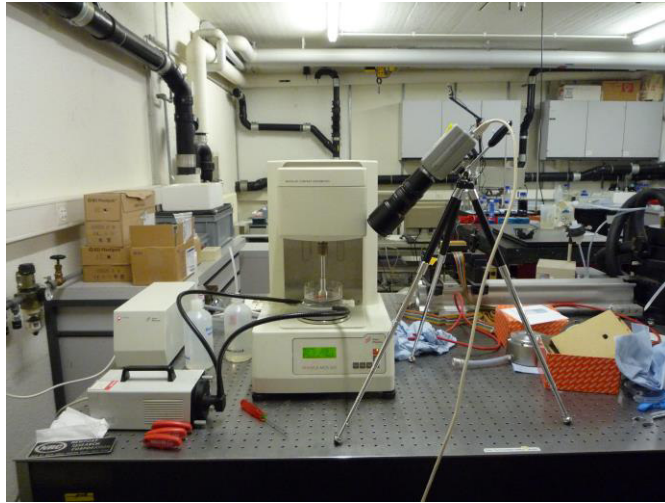


**Figure 5.1** Overview of the experimental apparatus

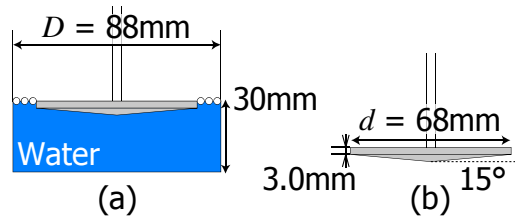


**Figure 5.2** (a) Side view of the measurement section (b) geometry of the inner cone

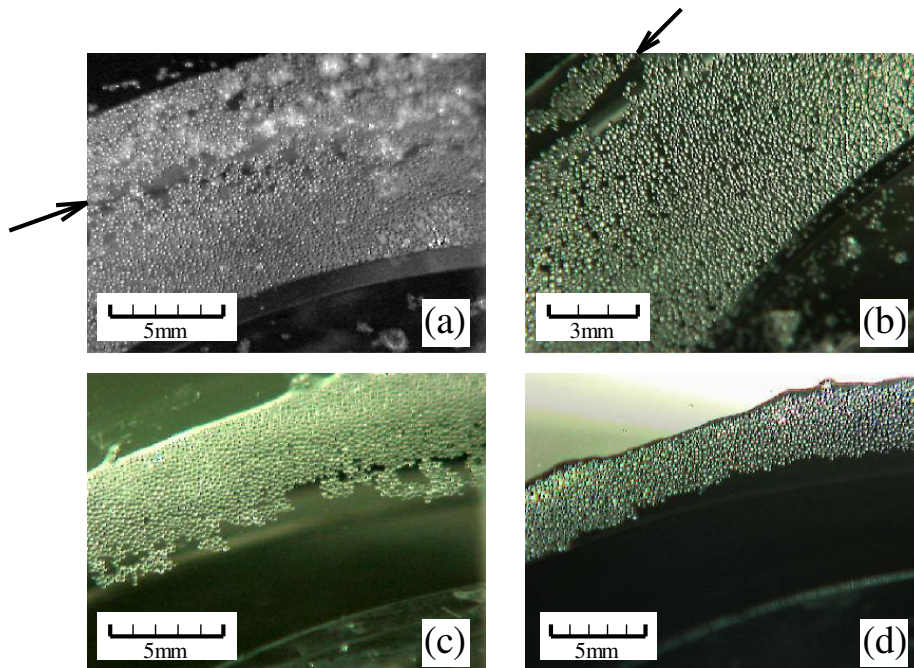


**Figure 5.3** Particle distributions recorded by the camera for (a)  $\alpha = 0.76$ , (b)  $\alpha = 0.43$ , (c)  $\alpha = 0.22$  and (d)  $\alpha = 0.20$

### 5.3 Effective viscosity of suspensions characterized with flow curve

The measured original torque  $T$  depending on shear rate is shown in Fig. 5.4 (a). The torque includes contributions from both the suspension layer and water under the cone. Right after the cone start rotation, or the applied shear rate is changed, torque value varies on time. As time advances, the torque value converges to a value under the steady state. Figure 5.4 (a) indicates torque under the steady state. It takes several minutes until torque converges although it depends on shear rate and concentration of particles. The measurement was begun with low shear rate, and then shear rate was increased (sweep up). After that, the measurement was continued while decreasing shear rate (sweep down). In Fig. 5.4 (a), torque values obtained in both sweep up and sweep down tests are plotted. The clear difference between these tests can be seen only in the condition with highest concentration,  $\alpha = 0.76$ .

In low concentration conditions,  $\alpha = 0.20$  and  $0$ , clear relation between shear rate and torque cannot be seen in  $\dot{\gamma} < 10^0 \text{ s}^{-1}$ . This is because applied torque to the cone is small compared to minimum torque that the rheometer can detect ( $10^{-8} \text{ N}\cdot\text{m}$ ). In other concentration conditions,  $\alpha = 0.76, 0.43$  and  $0.22$ , torque value converges as shear rate decreases. The convergence of torque implies the existence of yield stress. Torque increases as shear rate increases in  $\dot{\gamma} > 10^0 \text{ s}^{-1}$  regardless of concentration. This implies that the suspensions behave as viscous liquid under the high shear rate, but it is not clear in Fig. 5.4 (a) whether the increase of torque is caused by the suspension layer or water: Because the increase of the torque is observed even in the condition of  $\alpha = 0$ , the torque contribution from the water should be removed. The relation between shear rate,  $\dot{\gamma}$ , and torque in  $\alpha = 0$ ,  $T_w$ , is approximated by

$$T_w = a\dot{\gamma}^b, \quad (5.5)$$

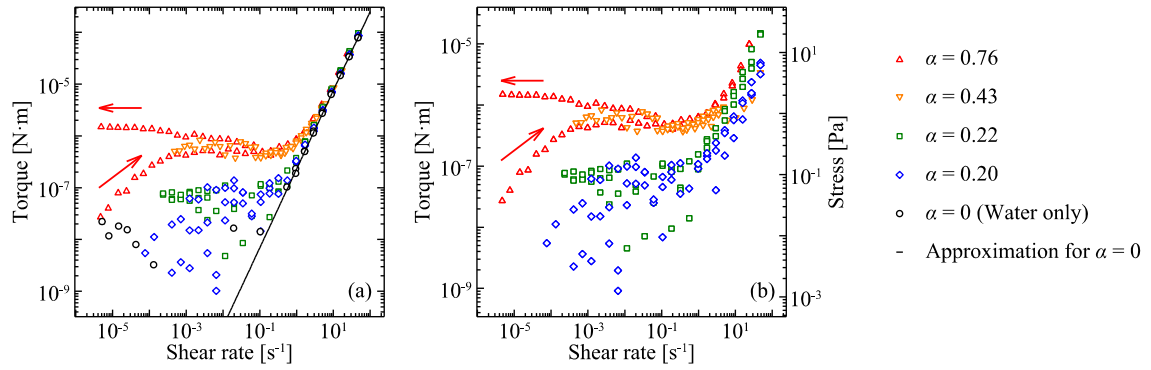
where  $a$  and  $b$  are constants determined to fit the relation obtained in the experiment. Because the contribution from the water to torque is significant in  $\dot{\gamma} > 10^0 \text{ s}^{-1}$ , experimental data only in this shear rate range were taken into account in the determination of  $a$  and  $b$ . According to Fig. 5.4 (a), Eq. (5.5) approximates the relation between  $\dot{\gamma}$  and  $T_w$  well.

Figure 5.4 (b) shows the torque after the contribution from water is subtracted, namely  $T_s$  in Eq. (5.1). The torque  $T_s$  is regarded as contribution only from the suspensions. The left and right axis indicate the torque  $T_s$  and corresponding shear stress  $\tau$ , respectively. The torque still increases as shear rate increases in  $\dot{\gamma} > 10^0 \text{ s}^{-1}$  even after  $T_w$  is subtracted for all concentrations. Thus Fig. 5.4 (b) means that the suspensions behaves as viscous material in the high shear rate region. As shear rate decreases, shear

stress converges to an yield stress in conditions of  $\alpha = 0.76, 0.43$  and  $0.22$ , which means the suspensions are rigid under the low shear rate. Particularly, the flow curve for  $\alpha = 0.76$  obtained in the down sweep measurement clearly shows yield stress  $\tau_y$  at around 2 Pa. The existence of the yield stress consistent with Fig. 5.3 which shows that particles are driven in inner region, and are static in outer region. In steady state, shear stress distribution between the cone and the cup  $\tau(r)$  is described as

$$\tau(r) = \tau_{in} \left( \frac{r_{in}}{r} \right)^2, \quad (5.6)$$

where  $\tau_{in}$  means shear stress acting on the cone. Because shear stress decreases as  $r$  increases, the fluid is not driven in outer region where shear stress is smaller than the yield stress.



**Figure 5.4** Torque contribution from (a) both suspension layer and water (b) suspension layer only depending on shear rate

The characteristics of the suspensions, yield stress and viscosity under high shear rate, are described with Casson model namely

$$\sqrt{\tau} = \sqrt{\eta_{\infty} \dot{\gamma}} + \sqrt{\tau_y}, \quad (5.7)$$

where  $\eta_{\infty}$  means convergence value of viscosity under infinitely high shear rate. Casson model was originally developed by considering structure formation in suspensions to characterize printing inks [20,21]. The flow curve of  $\alpha = 0.76$ , which shows the yield stress clearly, is approximated by Eq. (5.7). Constants in the model,  $\eta_{\infty}$  and  $\tau_y$ , are determined as 0.11 Pa.s and 1.1 Pa, respectively, by the least square approximation to the flow curve obtained in the down sweep test. Figure 5.5 (a) shows the flow curves obtained in the experiment and the approximation with Eq. (5.7). The approximation curve explains the increase of shear stress under high shear rate and

existence of yield stress. However, the flow curve obtained in the down sweep test has local minimum of shear stress at around  $\dot{\gamma} = 0.2 \text{ s}^{-1}$  which is not explained by Casson model. In the up sweep test, shear stress increases as shear rate increases in  $\dot{\gamma} < 10^{-4} \text{ s}^{-1}$ . Also this relation is not described by Eq. (5.7). As shear rate exceeds  $10^{-4} \text{ s}^{-1}$ , the flow curve draws a plateau until  $10^0 \text{ s}^{-1}$ , and shear stress increases again. In flow curves which have local minimum of shear stress, there is a shear rate range with negative gradient, namely  $\partial\tau/\partial\dot{\gamma} < 0$ . It is known that this shear rate range is jumped and is not realized in stress-controlled tests [22-26].

Figure 5.5 (b) shows viscosity curve, namely the relation between shear rate and viscosity. Viscosity curves of all suspensions show a tendency called shear thinning that viscosity decreases as shear rate increases. According to Fig. 5.4 (b), shear stress is constant in a wide shear rate range, particularly in cases of  $\alpha = 0.76$  and  $0.43$ . This means that viscosity drastically decreases in this shear rate range. It seems viscosity reaches a minimum at around  $\dot{\gamma} = 2 \text{ s}^{-1}$ , and increases slightly as shear rate increases. The increase of viscosity is interpreted as the effect of water under the suspension layer: Flows of the suspension layer and water interacts each other, and it is impossible to separate torque into contributions from suspension layer and water with Eq. (5.1). In interfacial rheology, Boussinesq number  $Bo$  is referred to confirm whether the interfacial flow is independent from the flows of continuous phase or not [14],

$$Bo = \frac{\eta_{int}}{(\eta_{(1)} + \eta_{(2)})r_{out}}, \quad (5.8)$$

where  $\eta_{int}$  means interfacial viscosity,  $\eta_{(1)}$  and  $\eta_{(2)}$  are viscosities of continuous phases in both side of the interface. When  $Bo \gg 1$ , the interfacial flow is independent from the flows of continuous phases. Although it is impossible to derive  $Bo$  directly from Fig. 5.5 (b) because analysis based on interfacial rheometry is required to obtain  $\eta_{int}$ . According to the interfacial viscosity curve obtained from the same torque data as Fig. 5.4 (a) [27],  $Bo$  reaches unity at around  $\dot{\gamma} = 10^1 \text{ s}^{-1}$  in all concentration conditions. Under low shear rate, viscosity increases infinitely when shear rate approaches to zero except the curve obtained in down sweep test for  $\alpha = 0.76$ . The infinite viscosity means that the suspension has yield stress.

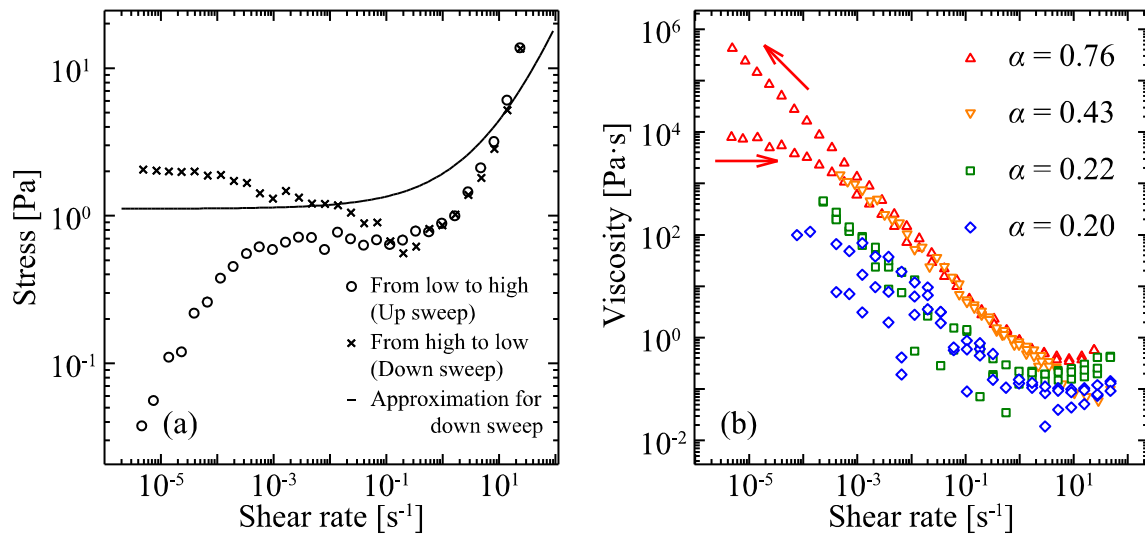


**Figure 5.5** (a) Flow curves for  $a = 0.76$  obtained in up sweep and down sweep tests with approximation by Casson model (b) Relations between shear rate and viscosity for suspensions with different particle concentrations

#### 5.4 Conclusion

A new measurement technique is developed based on interfacial rheometry to quantify shear-rate-dependent viscosity of highly concentrated suspensions. Spherical particles, whose diameter is about 100 nm, are dispersed on the surface of water to form a suspension layer. Torque to deform the layer is measured with a rheometer, and viscosity of the suspension is derived from the torque. To remove torque contribution from water, torque obtained in the measurement without particles are subtracted. By measuring viscosity of the suspension layer on the water surface, it is enabled to measure viscosity of highly concentrated suspension. Motion of particles is recorded with a camera at the same time.

As a result of the viscosity measurement, it is clarified that the suspension have yield stress particularly in high concentration conditions. Shear stress is almost constant at the yield stress while  $\dot{\gamma} < 10^{-1} \text{ s}^{-1}$  in the condition of the highest concentration,  $\alpha = 0.76$ . Under the higher shear rate, shear stress increases as shear rate increases. This tendency is explained with Casson model well. According to images recorded by the camera, particles are driven in the inner region, and do not move in outer region. This is consistent with the existence of yield stress. The constant shear stress is expressed as shear thinning in viscosity curve.

## References

- [1] A. Einstein, Eine neue Bestimmung der Moleküldimensionen, *Ann. Phys.* 19 (1906) 289-306
- [2] G. K. Batchelor, The stress system in a suspension of force-free particles, *J. Fluid Mech.* 41 (1970) 545-570
- [3] G. K. Batchelor, The effect of Brownian motion on the bulk stress in a suspension of spherical particles, *J. Fluid Mech.* 83 (1977) 97-117
- [4] G. K. Batchelor, J. T. Green, The determination of the bulk stress in a suspension of spherical particles to order  $c^2$ , *J. Fluid Mech.* 56 (1972) 401-427
- [5] C. Chang, R. L. Powell, Effect of particle size distribution on the rheology of concentrated bimodal suspensions, *J. Rheol.* 38 (1994) 85-98
- [6] I. M. Krieger, T. J. Dougherty, A mechanism for non-Newtonian flow in suspensions of rigid spheres, *Trans. Soc. Rheol.* 3 (1959) 137-152
- [7] J. J. Stickel, R. L. Powell, Fluid mechanics and rheology of dense suspensions, *Annu. Rev. Fluid Mech.* 37 (2005) 129-149
- [8] D. R. Foss, J. F. Brady, Structure, diffusion and rheology of Brownian suspensions by Stokesian dynamics simulation, *J. Fluid Mech.* 407 (2000) 167-200
- [9] C. Völtz, M. Nitschke, L. Heymann, I. Rehberg, Thixotropy in macroscopic suspensions of spheres, *Phys. Rev. E* 65 (2002) 051402
- [10] C. T. Crowe, T. R. Troutt, J. N. Chung, Numerical models for two-phase turbulent flows, *Annu. Rev. Fluid Mech.* 28 (1996) 11-43
- [11] J. K. Eaton, J. R. Fessler, Preferential concentration of particles by turbulence, *Int. J. Multiphase Flow* 20 (1994) 169-209
- [12] S. Sundaram, L. R. Collins, Collision statistics in isotropic particle-laden turbulent suspension. Part 1. Direct numerical simulations, *J. Fluid Mech.* 335 (1997) 75-109
- [13] Y. Murai, Drag reduction of large vessels by microbubble injection, *J. Jpn. Inst. Energy* 93 (2014) 1038-1043 (in Japanese)
- [14] P. Erni, P. Fischer, E. J. Windhab, Stress- and strain-controlled measurements of interfacial shear viscosity and viscoelasticity at liquid/liquid and gas/liquid interfaces, *Rev. Sci. Instrum.* 74 (2003) 4916-4924
- [15] P. Erni, P. Fischer, E. J. Windhab, Rheology of surfactant assemblies at the air/liquid and liquid/liquid interface, *Proc. 3rd Int. Symp. Food Rheol. Struct.* (2003) 411-415
- [16] M. J. Boussinesq, Sur l'existence d'une viscosité superficielle, dans la mince couche de transition séparant un liquide d'un autre fluide contigu, *Ann. Chim. Phys.* 29 (1913) 349-371

- [17] L. E. Scriven, Dynamics of a fluid interface, *Chem. Eng. Sci.* 12 (1960) 98-108
- [18] J. M. Lopez, A. Hirs, Direct determination of the dependence of the surface shear and dilatational viscosities on the thermodynamic state of the interface: Theoretical foundations, *J. Colloid and Interface Sci.* 206 (1998) 231-239
- [19] S. G. Oh, J. C. Slattery, Disk and biconical interfacial viscometers, *J. Colloid and Interface Sci.* 67 (1978) 516-525
- [20] C. C. Mill (ed), *Rheology of Disperse Systems*, Pergamon Press, London, 1959
- [21] G. W. Scott Blair, The success of Casson's equation, *Rheol. Acta* 5 (1966) 184-187
- [22] M. E. Cates, T. C. B. McLeish, G. Marrucci, The rheology of entangled polymers at very high shear stress, *Europhys. Lett.* 21 (1993) 451
- [23] A. Noort, W. J. Briels, Brownian dynamics simulations of concentration coupled shear banding, *J. Non-Newtonian Fluid Mech.* 152 (2008) 148-155
- [24] E. Miller, J. P. Rothstein, Transient evolution of shear-banding wormlike micellar solutions, *J. Non-Newtonian Fluid Mech.* 143 (2007) 22-37
- [25] J. K. G. Dhont, K. Kang, M. P. Lettinga, W. J. Briels, Shear-banding instabilities, *Korea-Australia Rheol. J.* 22 (2010) 291-308
- [26] S. M. Fielding, P. D. Olmsted, Flow phase diagrams for concentration-coupled shear banding, *Eur. Phys. J. E* 11 (2003) 65-83
- [27] Y. Murai, T. Shiratori, I. Kumagai, P. A. Rühls, P. Fischer, Effective viscosity measurement of interfacial bubble and particle layers at high volume fraction, *Flow Meas. Instrum.* 41 (2015) 121-128

### 6.1      Conclusions

With the aim to establish a novel method to achieve model-free characterization of non-Newtonian fluids instead of conventional constitutive equations based on rheology models, relationships among shear rate, strain and shear stress of several test fluids are investigated in shear flows. Unsteady rotating flows in cylindrical vessel were adopted for the characterization. Ultrasonic velocity profiling (UVP) and particle imaging velocimetry (PIV) were used to capture spatio-temporal velocity distributions of rotating shear flows, and shear stress distributions were derived by solving momentum conservation law on experimentally obtained flow information.

Derivation of shear rate and strain is one of the important factors to increase quality of the model-free characterization. Thus these in spin down flows were simultaneously visualized with the measured velocity profile in Chapter 2. The visualized shear rate and strain show where viscosity and elasticity contribute to stress generation, respectively. The observed phenomena such as reverse flow after the spin down involving recovery of deformation are appropriate for rheological property of test fluids. The visualization enables to intuitively recognize whether the measured flow contains viscoelastic information or not.

In Chapter 3, relations between shear rate and shear stress, termed flow curve, were obtained from velocity profiles. Concentric double cylinder system with a wide gap was employed as the flow configuration. Measurement of torque to rotate the inner cylinder makes it possible to obtain shear stress profile under the steady state. Because the flow curve is derived from stress and shear rate profiles, time required to obtain the flow curve is shorter than that in cases with conventional rheometer. Therefore the present technique is applicable to fluids whose viscosity varies as time advances. In this case, velocity profiling enables to obtain properties of the fluid with inverse procedure of physical phenomenon: In physics, the properties determine shear stress and velocity profiles. In this rheometry, on the other hand, the properties are determined from the shear stress and velocity profiles.

By analyzing unsteady flows, not only shear-rate-dependent viscosity but also viscoelasticity was characterized in Chapter 4. Time variations of the axial torque and velocity distributions were simultaneously measured for rotating flows in the double cylinder system after the spin up of the inner cylinder. Strain was added as the quantities that are taken into account to characterize viscoelasticity. Thus viscoelasticity was quantified as a relation among shear rate, strain and shear stress. The relation is named

“flow surface”, implying that it is expansion of flow curve representing relation between shear rate and shear stress. To obtain shear stress distributions which are necessary to derive the flow curve, momentum conservation law was solved by substituting experimentally obtained velocity profiles and wall shear stress. This procedure is exactly inverse of physical phenomenon: Physically velocity and shear stress distributions are given as a solution of momentum conservation. As a demonstration of practical applications of the flow surface, velocity distributions between concentric cylinders were reconstructed by solving momentum conservation adopting the flow surface simultaneously. In the reconstructed velocity distributions, deceleration of velocity, which is unique phenomenon in viscoelastic flow, was observed. This result implies that the flow surface can be utilized as an alternative of constitutive equation to simulate flows of non-Newtonian fluids.

In Chapter 5, effective viscosity of highly concentrated suspension was evaluated. By expanding a function of interfacial rheometer, effective viscosity was measured even in case the concentration is near the packing limit. Particle motion during the viscosity measurement was observed. Shear banding, which is the coexistence state of different shear rate layers, was observed, and its mechanism can be explained by shear-rate-dependency of the effective viscosity. The obtained viscosity curve supports the hypothesis that particles are accumulated in the center of vortices, and modify turbulent structure.

The utilization of flow surface in flow simulations is interpreted as the beginning of “data driven fluid engineering”. The adjective phrase, “data driven”, means that big data alter complex theories. Thus I mean that the flow surface is suitable, useful representation of the big data, and alters rheological models. Until now rheological models have been constructed based on microstructure of the material, thus a rheological model can describe property of specified group of materials. Data driven fluid engineering is meaningful as characterization which is applicable regardless of microstructure of the material. Velocity profiling techniques such as UVP and PIV enabled to derive quantitative flow surface by solving momentum conservation law to the inverse direction of physical phenomenon.

## 6.2 Future perspectives

The model-free characterization established in this study will work as data driven model generator for non-Newtonian fluids. The generator replies shear stress against input information about fluid deformation such as shear rate and strain. Thus it can be introduced to numerical simulations to predict viscoelastic fluid flows. In cases that researchers have to understand rheological properties of the fluid, the relation among shear stress and the quantities about fluid deformation should be displayed as the flow surface.

For making accuracy of the simulation high enough to practical use, however, some improvements are required in the procedure from the measurement to the utilization in the simulation. Accuracy of the data driven simulation depends on the amount of experimental data. Thus automation of data acquisition contributes improvement on accuracy of simulation. If experimental flow information in various condition, such as different rotational speeds or rotation modes, accuracy and applicable range of the simulation will be improved. It is desirable that information in some fundamental flow configurations such as extensional flow is also acquired automatically.

Although the flow surface was derived from velocity distributions measured by PIV, introduction of UVP yields advantages from two different viewpoints. First, UVP is preferred to PIV to automate measurements. Because PIV requires calibrations and post processes, and parameters in the post processes are determined as a result of trial-and-error, it is difficult to obtain velocity distributions automatically while changing measurement conditions. On the other hand, UVP does not require any calibrations and post processes with trial-and-error, and thus it is more suitable to introduce the automated measurement system. The second reason why UVP is preferred is applicability for opaque fluids. To quantify property of opaque non-Newtonian fluids such as yogurts by using this model-free characterization, the embedded velocimetry has to be applicable for opaque fluids.

Once experimental data are acquired in various conditions, an algorithm to determine shear stress takes on significance. As described in Chapter 4, linear interpolation among experimental data was introduced as an algorithm. This interpolation is insufficient to express shear stress as multiple value function of shear rate and strain. In the reconstruction of velocity distribution with the linear interpolation, oscillatory motion of the fluid was not appeared because shear stress is described as the multiple value function. Namely shear stress is determined not only shear rate and strain, but depending on deformation history. By improving the algorithm to take into account

hysteresis as a factor to determine shear stress, the oscillatory motion will be reproduced. Considering application for numerical simulations of flows in complex configurations such as processing plant or digestive organs, it is required to the algorithm to choose proper information from experimental data in various configurations, and determine stress based on it.

### 6.3 Summary of measurement limitations

#### Size of the experimental apparatus

Radius of the inner cylinder	$r_{in} = 15 \text{ mm}$
Radius of the outer cylinder	$r_{out} = 71.5 \text{ mm}$

#### Reference properties of test fluids

	Silicone oil	Polyacrylamide (PAA) solution
Power law index $n$ [-]	1.0	0.25
Power law coefficient $k$ [Pa·s <sup><math>n</math></sup> ]	0.97	5.9
Relaxation time $\lambda$ [s]	0	10~100
Density $\rho$ [kg/m <sup>3</sup> ]	970	1000

#### Limitation of Reynolds number

$$\text{Re} = \frac{\rho U_{wall} (r_{out} - r_{in})}{k \dot{\gamma}_c^{n-1}} < \text{Re}_c, \quad (3.27)$$

$$\dot{\gamma}_c = \frac{U_{wall}}{r_{out} - r_{in}}, \quad (3.28)$$

$$\text{Re}_c \cong 100$$

#### Limitation of Deborah number

$$De = \frac{\lambda U_{wall}}{r_{out} - r_{in}} < De_c, \quad (4.21)$$

$$De_c \cong 19$$

Maximum rotational speed of the inner cylinder  $U_{max}$  [mm/s]

	Silicone oil	PAA solution
$Re < Re_c$	176	111
$De < De_c$	-	21.4 (for $\lambda = 50$ s)
$U_{max}$	176	21.4

Spatial distribution of velocity and shear rate under the steady state

$$u_\theta = \frac{r_{in}^{2/n}}{1 - (r_{in}/r_{out})^{2/n}} \left( r^{1-2/n} - r_{out}^{-2/n} r \right) \frac{U_{wall}}{r_{in}}, \quad (3.8)$$

$$\dot{\gamma} = -\frac{2}{n} \frac{1}{1 - (r_{in}/r_{out})^{2/n}} \left( \frac{r_{in}}{r} \right)^{\frac{2}{n}} \frac{U_{wall}}{r_{in}}, \quad (3.9)$$

Maximum and minimum shear rate under  $U_{wall} = U_{max}$

$$\dot{\gamma}_{max} = -\frac{2}{n} \frac{1}{1 - (r_{in}/r_{out})^{2/n}} \frac{U_{max}}{r_{in}}, \quad (3.10)$$

$$\dot{\gamma}_{min} = -\frac{2}{n} \frac{1}{1 - (r_{in}/r_{out})^{2/n}} \left( \frac{r_{in}}{r_{out}} \right)^{\frac{2}{n}} \frac{U_{max}}{r_{in}}, \quad (3.11)$$

	Silicone oil	PAA solution
$\dot{\gamma}_{max}$ [s <sup>-1</sup> ]	-247	-11.0
$\dot{\gamma}_{min}$ [s <sup>-1</sup> ]	-10.9	-4.3×10 <sup>-5</sup>